X-ray observations of the accreting pulsars Her X-1 and EXO 2030+375

Dissertation
zur Erlangung des Grades eines Doktors
der Naturwissenschaften
der Fakultät für Mathematik und Physik
der Eberhard-Karls-Universität zu Tübingen

vorgelegt von
Dmitry Klochkov
aus Nizhnekamsk, Russland

2007

Tag der mündlichen Prüfung:	17. Dezember 2007
Dekan:	Prof. Dr. N. Schopohl
1. Berichterstatter:	Prof. Dr. R. Staubert, Tübingen
2. Berichterstatter:	Prof. Dr. K. Werner, Tübingen

Abstract

The dissertation presents the analysis and interpretation of the multi-instrument X-ray observations of two accreting binary pulsars Her X-1 and EXO 2030+375 performed with the X-ray observatories *INTEGRAL, RXTE,* and *Swift.*

The intermediate mass X-ray binary system Her X-1/HZ Her was repeatedly observed with *RXTE* since its launch in 1996. The *All Sky Monitor (ASM)* aboard the satellite provided almost uninterrupted monitoring of the 2–12 keV flux of the pulsar. In July–August 2005 Her X-1 was observed by the *INTEGRAL* observatory which covered a substantial part of a main-on state of the system. Using these observations along with the historical data we studied the secular changing of the orbital period of the system; searched for the long-term correlations between the 35 d precessional period of the accretion disk, the 1.24 s pulsation period, and the X-ray luminosity of the source; explored the pulse-averaged and pulse-resolved X-ray spectra of the source; modeled the observed behavior of anomalous dips and post-eclipse recoveries. The following main results were obtained. A new orbital ephemeris of the system was constructed. The value of the secular decrease of its orbital period was improved. The long-term correlations between the 35 d precessional period of the accretion disk and 1.24 s pulsation period as well as between the X-ray luminosity of the source and the 1.24 s period were confirmed. A positive correlation of the cyclotron line energy with the X-ray luminosity of the source was revealed. The observed behavior of anomalous dips and post-eclipse recoveries was reproduced using a numerical model. Spectral changes during X-ray dips were modeled with a partial covering spectral model, assuming that the observed radiation contains both absorbed and non-absorbed contributions. The energy, width, and the depth of the cyclotron line as well as the spectral continuum parameters were found to vary significantly with pulse phase. To explain

most of the observed properties of the system a model was used which includes a precessing twisted accretion disk, a freely precessing neutron star, and an accretion stream which moves out of the system's orbital plane.

EXO 2030+375 belongs to the class of Be/X-ray binaries. In June–September 2006 the source entered into the second giant (type II) outburst since its discovery. During the outburst the pulsar was observed with *INTEGRAL* and *Swift*. For the first time, the broad band (3–200 keV) X-ray spectrum of the source during a giant outburst was studied. X-ray pulse profiles were explored. The dependence of the spin-up rate on the X-ray luminosity of the source was studied using different accretion torque models. The following main results were obtained. We did not confirm the presence of the cyclotron line in the spectrum of the source (reported previously on the basis of *RXTE* data). The X-ray pulse profiles were found to be highly luminosity-dependent. The dependence of the spin-up rate on the X-ray luminosity measured during the 2006 giant outburst was found to be different from that observed during the 1985 giant outburst. This was interpreted as an indication of a possible change of the configuration of the neutron star's magnetosphere and/or accretion disk between the two giant outbursts.

Contents

Abstract **iii**

1 Introduction **1**

2 X-ray binaries **3**
2.1 General picture . . . 3
2.2 Origin and evolution . . . 4
2.2.1 Evolution of a single star . . . 5
2.2.2 Roche approximation and mass transfer in a binary . . . 6
2.2.3 Evolution of HMXB . . . 8
2.2.4 Evolution of LMXB . . . 8
2.3 Accretion mechanism . . . 9
2.3.1 Roche lobe overflow and disk accretion . . . 9
2.3.2 Accretion from the stellar wind . . . 10
2.4 Accreting pulsars . . . 11
2.4.1 Accretion onto a magnetized neutron star . . . 11
2.4.2 Accretion torques and spin period behavior . . . 12
2.4.3 X-ray spectrum . . . 12

3 Her X-1/HZ Her: intermediate mass X-ray binary **14**
3.1 System overview . . . 14
3.2 Observational properties . . . 15
3.2.1 35 d period . . . 15
3.2.2 X-ray dips . . . 16
3.2.3 X-ray pulse profiles . . . 17
3.2.4 Cyclotron line . . . 18
3.3 Model and open questions . . . 21

4 *RXTE* observations of Her X-1 **25**
4.1 *Rossi XTE*: mission overview . . . 25
4.1.1 Proportional counter array . . . 25
4.1.2 *HEXTE* detectors . . . 27
4.1.3 All sky monitor . . . 27
4.2 Refining system orbital ephemeris . . . 28
4.2.1 Phase-connection method . . . 29

4.2.2 *RXTE* data . . . 29
4.2.3 Orbital ephemeris . . . 31
4.3 Measuring parameters of individual 35 d cycles . . . 33
4.3.1 Preliminary processing . . . 34
4.3.2 Turn-on times and $(O-C)$ diagram . . . 35
4.3.3 Maximum main-on flux . . . 36
4.3.4 Correlations between $(O-C)$, maximum main-on flux, and the pulse period 38
4.3.5 Correlation between the CRSF energy and the maximum main-on flux . . . 45
4.4 Averaged *ASM* light curves . . . 46
4.4.1 Evidence for a change in the disk tilt during the 35 d cycle . . . 46
4.4.2 The model for reproducing the behavior of dips . . . 49

5 *INTEGRAL* observations of Her X-1 53
5.1 *INTEGRAL* observatory: mission overview . . . 53
5.1.1 IBIS . . . 55
5.1.2 *SPI* . . . 56
5.1.3 *JEM-X* . . . 56
5.2 Observations and data reduction . . . 56
5.2.1 Summary of observations . . . 56
5.2.2 *IBIS/ISGRI* data processing . . . 57
5.2.3 *SPI* data processing . . . 59
5.2.4 *JEM-X* data processing . . . 59
5.3 Timing analysis . . . 60
5.3.1 Light curve . . . 60
5.3.2 Pulse profiles . . . 60
5.3.3 Pulse period behavior . . . 63
5.4 Spectral analysis . . . 64
5.4.1 Pulse averaged spectrum. . . . 64
5.4.2 X-ray dips . . . 68
5.4.3 Pulse-phase-resolved spectra . . . 70

6 EXO 2030+375: Be X-ray binary 75
6.1 System description . . . 75
6.2 X-ray and optical monitoring . . . 76
6.2.1 Pulse period and X-ray flux history . . . 76
6.2.2 Type I X-ray outbursts . . . 78
6.2.3 Optical/IR observations . . . 78
6.2.4 X-ray pulse profiles . . . 79
6.2.5 X-ray spectrum . . . 79
6.3 The model and open questions . . . 80

7 *INTEGRAL* and *Swift* observations of EXO 2030+375 84
7.1 *Swift* satellite: mission overview . . . 84
7.1.1 *BAT* . . . 85
7.1.2 *XRT* . . . 86

7.2 Observations and data reduction . . . 87
7.2.1 Summary of observations . . . 87
7.2.2 *IBIS/ISGRI* and *JEM-X* data processing . . . 87
7.2.3 *BAT* data processing . . . 88
7.2.4 *XRT* data processing . . . 89
7.3 Timing analysis . . . 89
7.3.1 Pulse period behavior . . . 89
7.3.2 Pulse profiles . . . 90
7.4 Spectral analysis . . . 90

8 Discussion **95**
8.1 Her X-1 . . . 95
8.1.1 Secular change of the orbital period . . . 95
8.1.2 The disk–stream coupling model . . . 97
8.1.3 Correlation of X-ray luminosity with spin-up rate . . . 98
8.1.4 Correlation of the cyclotron line energy and the X-ray luminosity . . . 98
8.1.5 Pulse profiles . . . 99
8.1.6 Short-time scale variations of the pulse period . . . 100
8.1.7 Absorption during X-ray dips . . . 100
8.1.8 Pulse-phase variability of the X-ray spectrum . . . 101
8.2 EXO 2030+375 . . . 102
8.2.1 X-ray luminosity – $\dot{\boldsymbol{P}}_{\mathbf{spin}}$ relation: probing the accretion theory . . . 102
8.2.2 Pulse profiles . . . 106
8.2.3 Broad band X-ray spectrum . . . 107

9 Summary and conclusions **108**

Bibliography **110**

A Turn-On times and maximum main-on fluxes **118**

B Spin period **121**

C Numerical model of disk wobbling in Her X-1 **124**

Acknowledgements **128**

Chapter 1

Introduction

Since the Earth's atmosphere is opaque to X-rays, X-ray astronomy emerged with the space age. First X-ray detectors were carried aloft on rockets and then parachuted back down to Earth. They detected X-ray emission from the solar corona (Chubb et al. 1957). This emission was relatively weak which led many astronomers and astrophysicists in the late 1950s and early 1960s to think that efforts to build larger detectors and telescopes to observe X-rays from other celestial sources would be fruitless. However, it turned out that most of X-ray sources are much more powerful than the Sun. The first such source, Sco X-1, was discovered in 1962 during a rocket flight, by a group led by Riccardo Giacconi (Giacconi et al. 1964; Giacconi & Gursky 1974), who won the Nobel Prize for Physics in 2002 for his pioneering studies in X-ray astronomy. Major progress in the field began in the 1970s with the use of satellites equipped with X-ray detectors. The first one, *Uhuru*, was launched in 1970 (Kellogg 1975; Giacconi et al. 1972). It mapped the X-ray sky in the energy range 2–6 keV. The *Einstein* observatory was launched in November 1978. Its payload contained the first large focusing X-ray telescope. *Einstein* provided high-resolution images and accurate locations for thousands of X-ray sources (Harris et al. 1993). The European X-Ray Observatory Satellite *(EXOSAT)* operated from May 1983 to April 1986 allowed to perform continuous observations of X-ray sources lasting several days without the interference of Earth occultations. This allowed to discover transient nature of many sources. These and later missions (*Chandra, XMM-Newton, Rossi XTE, BeppoSAX, INTEGRAL* and others) observed X-ray radiation from ordinary stars, white dwarfs, neutron stars black holes, remnants of supernova explosions, active galactic nuclei and hot gas in intergalactic space. X-ray astronomy has changed our view of the universe and revealed it to be full of evolving, explosive, high energy phenomena.

Soon after first X-ray observations with satellites it was discovered that the X-ray emission from many point-like X-ray sources undergoes rapid and sometimes periodic variations. Combined observations with optical and X-ray telescopes have demonstrated that these X-ray sources are members of binary systems – *X-ray binaries* – in which matter streams from a normal star onto a nearby collapsed star with an intense gravitational field. Most of point X-ray sources discovered in our Galaxy belong to this class of objects. So, it is not surprising that the first discovered extrasolar X-ray source, Sco X-1, was identified as the X-ray binary system. Two objects explored in this work, Hercules X-1 and EXO 2030+375, are also X-ray binaries where the compact companion is a neutron star. We present the analysis of observations of these two sources performed with the modern X-ray missions – *INTEGRAL*, *RXTE*, and *Swift*. Excellent capabilities of the instruments

aboard these satellites allowed to probe the physical processes in these two binary systems which are both good representatives of their classes of binary stars.

This thesis is organized as follows. Chapter 2 gives an introduction to the close X-ray binary systems. In Chapter 3 we give a description of the Hercules X-1 X-ray binary. First, we provide an overview of observational properties of the source. Then we present a theoretical interpretation of these properties and outline the open questions related to the system. Chapter 4 is devoted to the analysis of the *RXTE* observations of the source. Using these observations we construct the new orbital ephemeris of Her X-1 and measure the secular decrease of its orbital period, explore the parameters of individual 35 d cycles of the source and study their correlation with each other, construct the averaged 35 d light curves of the source and reproduce the timing behavior of X-ray dips in these curves using a numerical model. In Chapter 5 we analyze the *INTEGRAL* observations of Her X-1. This analysis includes the study of time- and energy-dependent pulse profiles, pulse period variations, pulse-averaged and pulse-resolved X-ray spectra as well as spectral changing during X-ray dips. Chapter 6 provides a description of the EXO 2030+375 binary system. As in the case of Her X-1, it consists of an overview of the source's observational properties followed by a description of the current theoretical model of the system and open questions related to it. Chapter 7 is devoted to the analysis of the multi-instrument (*INTEGRAL* and *Swift*) observations of EXO 2030+375 during its giant outburst. In this chapter we study the energy- and luminosity-dependent pulse profiles, the decrease of the pulsation period during the outburst (spin-up), and the pulse-averaged broad-band X-ray spectrum of the source. In Chapter 8 we discuss the results of our analyses and provide a theoretical interpretation of them. A summary and conclusions are given in Chapter 9.

Chapter 2

X-ray binaries

2.1 General picture

A binary stellar system is simply one in which two stars orbit around a common center of mass, that is they are gravitationally bound to each other. Roughly half of the stars in the sky are part of a binary or multiple star system. A sub-class of binary systems are *X-ray binaries*, the systems in which a compact object (a white dwarf, neutron star or a black hole formed after collapse of an ordinary star) and a stellar companion orbit each other at a distance small enough to enable mass transfer from the companion star to the compact object. Matter from the stellar companion spiraling toward the compact object often forms a so-called *accretion disk* around the latter. Gravitational energy of accreted matter is released in the form of X-ray radiation that comes from the area around the compact object where the gas is heated to very high temperatures (10^6 to 10^8 K). In case of a neutron star or a white dwarf the emission originates from both the accretion disk and the surface of the compact star while in black hole binaries the only source of X-rays is the accretion disk. Figure 2.1 shows a sketch of an X-ray binary system as it would be seen by a nearby observer.

The donor star can provide matter through the stellar wind, the ejection of gas off the surface of the star. This normally takes place in binaries where the companion's mass is greater than several solar masses (so-called *High Mass X-ray Binaries* or HMXB). For systems with the lower mass stellar companion (*Low Mass X-ray Binaries* or LMXB) mass accretion can proceed through the *inner Lagrangian point* – the point where gravitational forces of the two stars and centrifugal force cancel.

If the neutron star or white dwarf in the X-ray binary is highly magnetized (with the magnetic dipole moment of the order of 10^{30} Gcm^3 or more) the accretion flow will be disrupted at some distance from the accretor by the magnetic field and funneled onto the magnetic poles where most of X-rays originate. In case of a neutron star, if the magnetic poles are displaced with respect to the rotational axis of the star the observed X-ray flux will be modulated with the star's spin period leading to the phenomenon of an *X-ray pulsar* (pulsating X-ray source).

Galactic X-ray Binaries (those located in our Galaxy) containing a neutron stars or a black hole are among the brightest sources in the X-ray sky. Some of them are persistent while others can be observed only during short episodes of high X-ray luminosity (outbursts) and remain in their quiescent state for most of the time. They are called *transient* sources. Observational studies of X-ray binaries provide a unique probe of the physical mechanisms operating under extreme conditions

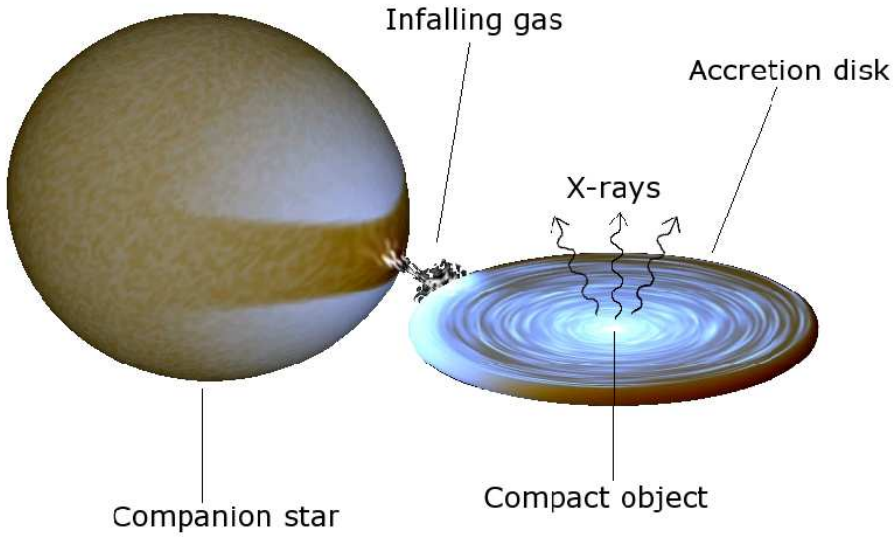

Figure 2.1 A schematic view of an X-ray binary. Gas is pulled off the normal star by the gravity of the compact object.

that are reached in the vicinity of neutron stars and black holes, at the site of X-ray emission.

In the next sections we describe in more details various aspects of X-ray binaries.

2.2 Origin and evolution

The compact objects in X-ray binaries are remnants of ordinary stars. Thus, our understanding of the origin and evolution of X-ray binaries is largely based on our understanding of the evolution of single stars. We will start, therefore, with a brief description of some aspects of single-star evolution (Section 2.2.1). With a few exceptions, X-ray binaries with black holes and neutron stars have companions with masses either $\gtrsim 10M_{\odot}$ or $\lesssim 1M_{\odot}$ (see e.g. Lewin et al. 1995). As mentioned above, these two classes of sources are commonly referred to as HMXB and LMXB, respectively. HMXB and LMXB differ in many aspects such as the type of mass transfer and overall environment in the vicinity of the compact object. We will describe their evolution separately in Sections 2.2.4 and 2.2.3. X-ray binaries containing a white dwarf are called *Cataclysmic variables* (CVs). These systems differ in many aspects from the X-ray binaries containing a neutron star or a black hole. In the following we will be mostly concentrated on properties of neutron star and black hole X-ray binaries. A comprehensive review of CVs can be found in e.g. Lewin et al. (1995).

2.2.1 Evolution of a single star

The evolution of a star is driven by the properties of a self-gravitating gas in hydrostatic equilibrium. According to the virial theorem, the loss of energy of such a gas causes it to contract and therewith to increase its temperature. The contraction of the primordial gas cloud mainly consisting of hydrogen and helium causes an increase in pressure and temperature in the center until hydrogen starts fusing into helium, finally reaching equilibrium on the Main Sequence.[1] Upon exhaustion of the hydrogen, the core contracts further until pressure and temperature have risen enough for the fusion of helium into carbon and oxygen. This is accompanied by the expansion of the outer layers. At this stage the star leaves the main sequence and turns into a *red giant* or a *supergiant*. Thus, cycles of nuclear burning alternate with stages of exhaustion of nuclear fuel in the stellar core. If the star is massive enough ($\gtrsim 11M_\odot$) it continues this cycle until its core is made of iron, at which point further fusion does not produces energy. The core of such a star collapses to form a neutron star or a black hole. The gravitational energy released during the collapse is enough to explode the outer layers of the star – *supernova* explosion. In fact, most part of the gravitational energy released in a core-collapse supernova (~99,9% or $\sim 10^{53\div 54}$ erg) is carried away by neutrino (which interacts with matter only via weak force) and only small fraction ($\sim 10^{50\div 51}$ erg) goes into kinetic energy of the exploded matter. In a less massive star, pressure of degenerate electrons in the core at the end of one of nuclear burning stages may be high enough to prevent contraction to the density required for the ignition of the next fusion process. Extensive mass loss will erode such a star, until the degenerate core remains only. This core cools onto a white dwarf.

Each end-product of the evolution of a single star corresponds to a range of initial stellar masses (see e.g. Lewin et al. 1995). White dwarfs are formed by stars with masses $\lesssim 11M_\odot$. Stars with masses in the range of $\sim 11 - 40M_\odot$ form neutron stars. Black holes are the products of evolution of stars with masses higher than $\sim 40M_\odot$. It should be noted that the values of these ranges are only known approximately due to considerable uncertainty in our knowledge of the evolution of massive stars.

Two characteristic time scales are important for stellar evolution. The first one is the so-called nuclear time scale: the time spent by the star on the main sequence when it burns hydrogen in its core. This time scale is set by the ratio of the total amount of nuclear energy available to the rate of energy loss (i.e. the luminosity). The energy available is the amount of mass available for fusion (typically of the order of 10% of the total mass) times the amount of energy ϵ released per unit of time and per unit of mass by the fusion process (for hydrogen burning $\epsilon \sim 0.007c^2$):

$$\tau_n \simeq \frac{0.1M\epsilon}{L} \simeq 10^{10}\frac{M}{M_\odot}\frac{L_\odot}{L} \quad \text{yr}, \tag{2.1}$$

where M and L are the mass and luminosity of the star, respectively.

The expansion of the star upon exhaustion of the nuclear fuel in the core occurs on the thermal time scale. It is given by the ratio of the thermal energy content of the star to the luminosity:

$$\tau_t \simeq \frac{GM^2}{RL} \simeq 3\times 10^7\left(\frac{M}{M_\odot}\right)^2\frac{R_\odot}{R}\frac{L_\odot}{L} \quad \text{yr}, \tag{2.2}$$

[1] Main sequence stars are the central band of stars on the Hertzsprung-Russell Diagram. These stars' energy comes from nuclear fusion, as they convert Hydrogen to Helium in their cores. Most stars are Main Sequence Stars. The sun is a typical Main Sequence star.

where R is the radius of the star and G is the gravitational constant.

Since both binary systems explored in this work (Her X-1 and EXO 2030+375) contain a neutron star we will spend a few more words on these objects. As it was already mentioned, neutron stars are the products of evolution of rather massive stars ($\gtrsim 11 M_\odot$). Once a star has run out of nuclear fuel there is no more source of energy. The equilibrium of cold self-gravitating matter can only be sustained by quantum effects. If the density of matter is less than $\sim 10^{11}$ g cm^{-3}, equilibrium can be ensured by the repulsive forces of degenerate electrons. This picture is realized in white dwarfs. However, as it was shown by Chandrasekhar (1931), if the mass of the star is sufficiently large the configuration becomes unstable. Thus, there is a maximum allowable mass of a white dwarf (Chandrasekhar limit). This mass is found to be slightly larger than the mass of the Sun. Landau (1932) proposed that equilibrium of stars with higher masses can be sustained by nuclear forces. The term "neutron stars" for such objects was suggested by Baade & Zwicky (1934) who attributed their origin to the supernova explosions.

The masses of presently known neutron stars range from $\sim$1 to $\sim 2 M_\odot$ (see e.g. Stairs 2004) while their sizes are of the order of 10 km. The surface of a neutron star is a hard crust of thickness 1–7 km whose density increases inwards from 10^6 to 10^{10} g cm^{-3}. Beyond the crust, the crystalline structure is destroyed and matter (comprised mainly of free neutrons) passes into a liquid superfluid state. The density in the liquid core can increase up to the density of nuclear matter ($\sim 2.8 \times 10^{14}$ g cm^{-3}). Finally, a hard core might exist in the center of a neutron star. When (and if) the density exceeds the nuclear density by a factor of 2 or 3, very exotic stuff might be able to form, like pion condensates, lambda hyperons, delta isobars, and quark-gluon plasmas. A comprehensive review of the recent progress in the neutron star theory can be found in Heiselberg & Pandharipande (2000); Pethick et al. (2000).

2.2.2 Roche approximation and mass transfer in a binary

Before discussing evolution of X-ray binaries we will briefly describe the geometry of a binary system. The potential surfaces in a binary are determined by the gravitational attraction of both stars and by the motion of the two stars around each other. In the *Roche* approximation, it is assumed, that the gravitational field can be approximated as that of two point masses M_1 and M_2 corresponding to the masses of the stars and located at their centers. In a frame co-rotating with the binary revolution, one may write the potential as

$$\Phi = -\frac{GM_1}{r_1} - \frac{GM_2}{r_2} - \frac{\omega^2 r_3^2}{2}, \tag{2.3}$$

where r_1 and r_2 are the distances to the center of the stars, ω is the orbital angular velocity, and r_3 is the distance to the axis of rotation of the binary (Fig. 2.2). Close to each star, the potential is dominated by the gravity of that star, and the equipotential surface has an almost spherical shape. Further out, the equipotential surfaces are deformed, and for a critical value of the potential the equipotential surfaces of the two stars touch, in the so-called *inner Lagrange point* where the potential reaches an extremum. Thus, the net force on particle at this point is zero. The space surrounded by the equipotential surface containing the Lagrange point is called the *Roche lobe*. At other critical values of the potential the equipotential surfaces open up at the outer Lagrange points (see Fig. 2.2).

If the stellar surface reaches the boundary of the Roche lobe, mass will start flowing out via the inner Lagrange point in the direction of the companion star. If the star expands so rapidly

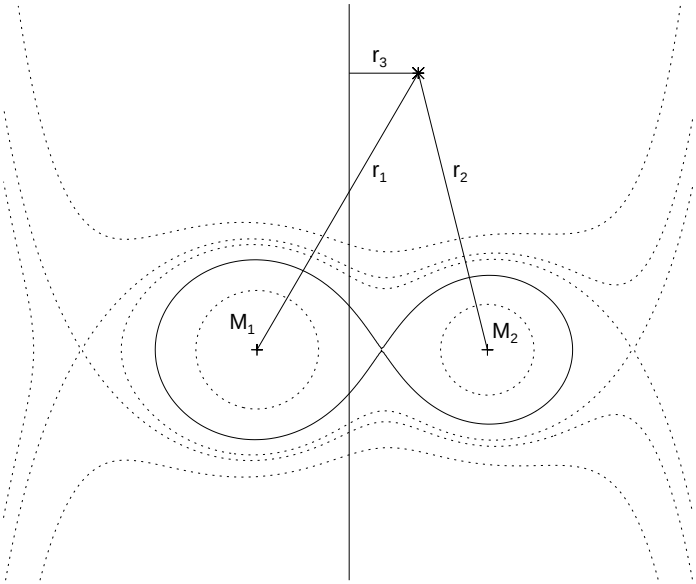

Figure 2.2 Roche lobe geometry for a mass ratio $M_1/M_2 = 3/2$. The plot shows cuts through equipotential surfaces of the co-rotating frame, parallel to the rotational axis, which is shown by the vertical solid line.

that its surface reaches an outer Lagrange point, mass may be lost from the binary through this point.

The more massive star which evolves faster (according to Eq. 2.1) expands first to fill its Roche lobe. Let us assume that the mass and angular momentum J of the binary system are conserved, i.e. we assume *conservative* evolution of the system. For a circular orbit these conditions are

$$M_1 + M_2 = const \tag{2.4}$$

$$J = \omega r_1^2 M_1 + \omega r_1^2 M_2 = const. \tag{2.5}$$

Using the third Kepler's law and the equations 2.4 and 2.5 we arrive at

$$\dot{M}_1 \frac{M_1 - M_2}{M_1 M_2} = \frac{\dot{a}}{2a}, \tag{2.6}$$

where $a = r_1 + r_2$ is the binary separation. From this formula one can see that the binary separation a and hence the orbital period decrease. Once the mass transfer has reversed the mass ratio, the orbital period may increase again. In reality, it is known that the conservative scenario in many cases cannot hold. Massive stars ($\gtrsim 10 M_\odot$) lose significant amounts of matter in the form of a stellar wind. Thus, some mass will be lost from the system, taking away angular momentum. However, as long as the amount of mass lost is not too large, the binary evolution will qualitatively still be fairly similar to the conservative scenario.

Both the conservative and non-conservative scenarios described above lead to a binary with the core of an initially fairly massive star in orbit around a relatively massive companion. Provided the core is sufficiently massive, it will evolve into a supernova that can leave behind a neutron star or a black hole.

2.2.3 Evolution of HMXB

In high-mass X-ray binaries the companion is a massive star (of a spectral type O or B) whose optical/UV luminosity may be comparable to, or greater than, that of the X-ray source. The permanently bright X-ray binaries, which were among those first discovered, are mostly close binaries, in which the donor star has evolved away from the main sequence (e.g. Cyg X-1, Vela X-1, Cen X-3). The supergiant emits a strong stellar wind, part of which is caught by the neutron star. In other systems, the massive star has expanded enough to fill its Roche lobe and transfers mass to the neutron star through the inner Lagrange point. An example of a system in which the donor is still smaller than the Roche lobe is Vela X-1. An example of a system in which the donor fills the Roche lobe is Cyg X-1. Because the the donor in these bright systems have already left the main sequence, the life time of the X-ray phase is set roughly by the thermal time scale given by Eq. 2.2.

If the compact object is a neutron star, the mass ratio is extreme, and a so-called "spiral-in" phase can be expected: the neutron star spirals into the envelope of its companion. The outcome of this process may be a merger, in particular in the short-period binaries. In wider systems the donor may have lifted its envelope to a larger radius, allowing the neutron star to expel it (due to gravitational interaction). In that case, the core of the massive star will emerge in a binary with the neutron star. It has been shown that Cyg X-3 may well be an example of such a binary (van Kerkwijk et al. 1992). The core proceeds with its evolution and may end as a white dwarf. An example of such a system is the binary that contains PSR0655+64. Alternatively, the evolved core may explode as a supernova and produce another neutron star. If the binary survives, it will consist of two neutron stars. PSR1913+16 and PSR2303+46 are examples of such binaries. In LMC X-3, the black hole is more massive than the donor star. The binary is very likely to survive the second supernova explosion, after which it will consist of a black hole and a neutron star. For a detailed discussion see e.g. Lewin & van der Klis (2006)

2.2.4 Evolution of LMXB

The nature of the low-mass X-ray binaries is rather less secure than that of high-mass X-ray binaries. The donor of the LMXB only rarely shows a clear signature in the observation. Below we provide an evolutionary scenario of LMXBs first suggested by (van den Heuvel 1983). As the progenitor of a neutron star or black hole must have been a fairly massive star, the progenitor binary must have had an extreme mass ratio. The massive star evolves first, and because of the extreme mass ratio will engulf its companion soon after the onset of mass transfer (see Eq. 2.6). So, the system will evolve through a common-envelope stage. The core of the massive star continues its evolution, and may turn into a supernova. In order for the binary to survive (not to be disrupted), this core should not be too massive. To some extent the disrupting effect of the mass loss during the supernova explosion can be "compensated" by a kick velocity of the neutron star (due to an asymmetry of the supernova explosion) that by chance happened to be in the right direction. If the orbital period is short enough to bring a $1M_{\odot}$ companion into contact with its Roche lobe within

a Hubble time the binary turns into a LMXB with a main-sequence donor. This usually requires an orbital period of 10–12 h or shorter. If the orbit is somewhat wider, loss of angular momentum during the supernova explosion may not suffice to bring the prospective donor into contact, and mass transfer will start only when the donor evolves away from the main sequence, and expands into a giant. Another possibility arises if the companion star is more massive, as in Her X-1 ($\sim 2 M_\odot$). When such a star starts filling its Roche lobe a second spiral-in phase may start, leaving the neutron star in an orbit around the core of an evolved star.

The mass transfer in a LMXB stops when the mass of the envelope drops below $\sim 0.001 M_\odot$, at which point the envelope collapses. The binary then consists of the degenerate core of the giant, which cools into a white dwarf, and a compact star. If the compact star is a neutron star, the accretion could have spun up the neutron star, and after the end of the mass transfer it may show up as a radio pulsar. A number of radio pulsars with low mass white dwarf companions have indeed been found. Also a number of millisecond accreting pulsars (currently eight) are found in LMXBs which confirms the evolutionary link between LMXBs and millisecond radio pulsars (White & Zhang 1997).

2.3 Accretion mechanism

As mentioned in Section 2.1, X-ray radiation in X-ray binaries is powered by gravitational energy released from the matter falling into the compact object. Accreting neutron stars and black holes can convert up to 10% of that energy into radiation. For a modest mass transfer rate of $\dot{M} \simeq 10^{17}\,\mathrm{g\,s^{-1}}$, one expects a luminosity of $10^{37}\,\mathrm{erg\,s^{-1}}$. If emitted thermally from an area of a few times the size of the object, this radiation must predominantly fall in the X-ray band ($\sim$1 keV). Higher characteristic temperatures occur when the neutron star has a strong magnetic field that funnels all accreting matter onto a small area near its two poles, or when for some reason the emission is (partially) non-thermal. Below we provide a brief description of different aspects of accretion process.

2.3.1 Roche lobe overflow and disk accretion

If matter is accreting from a substantial distance and possess significant specific angular momentum J one would expect the accreting gas to form a rotationally-flattened structure orbiting the compact object, an *accretion disk*. This typically requires that the *circularization radius* (see e.g. Frank et al. 1992; Pringle 1981)

$$R_{\rm circ} = \frac{J^2}{GM} \tag{2.7}$$

(where the matter would orbit if it lost energy but not angular momentum) should be larger than the effective size of the accretor. In X-ray binaries the accretor is a white dwarf, neutron star or black hole, and the condition (2.7) always holds if accretion is via Roche lobe overflow.

A particular element of gas in the accretion disk will then lose angular momentum through a process which is loosely referred to as viscosity, thereby allowing it to flow slowly inwards towards the compact object and eventually accrete. While the nature of this angular momentum transport was mysterious for some time, we now believe it to be due to magneto-hydrodynamical (MHD) turbulence driven by a well-studied instability, the magnetorotational instability (MRI) (see e.g. Balbus & Hawley 1991).

In many cases the accretion can be described using so-called *thin disk* approximation which assumes that cooling is always able to keep the local Kepler speed $v_k = (GM/R)^{1/2}$ supersonic (R is the distance to the accretor). In this case the disk lies essentially in the orbital plane, with only a small vertical extent H:

$$H \simeq \frac{c_s}{v_k} R \ll R, \tag{2.8}$$

where c_s is the local sound speed. The azimuthal speed of the disk is close to the Kepler value v_k. Both the radial and vertical velocities are much smaller. It is important that the three properties of being geometrically thin, Keplerian, and efficiently cooled are equivalent for any disk flow: if one of them breaks down, so do the other two. The thin disk approximation provides a rough description of the accretion flow in the systems where the companion fill its Roche lobe, and mass transfer is via the inner Lagrangian point. There are, however, a number of difficulties in explaining accretion disks using this approximation. If the X-rays came from a point source (the immediate vicinity of the neutron star or black hole) surrounded by a thin Keplerian disk, one would expect only total eclipses with very sharp ingress and egress or no eclipses at all (if the orbit inclination is far from 90°). However, "partial" eclipses are sometimes observed in LMXBs. This suggests that the X-ray source is effectively extended, presumably through the presence of some kind of scattering corona around it (White & Holt 1982). Irradiation of the disk by the central source which tends to extend the vertical scale of the disk has also to be taken into account (Begelman & McKee 1983). An accretion disk which spreads out enough within the Roche lobe of the compact object will be subject to tidal torques from the secondary star. This effect limits the size of the disk. Tidal torques can take angular momentum from matter at the outer disk edge, and return it to the binary orbit. A steady state is reached when the tidal torques remove the angular momentum at the rate it is transported outwards in the disk by viscosity.

2.3.2 Accretion from the stellar wind

In many X-ray binaries the mass-losing star does not fill its Roche lobe and the compact component must accrete from a wind from this star. This is an inheritently less efficient process than Roche lobe overflow: mass leaves the star in all directions, not just towards the accretor, and has enough kinetic energy to escape the system except where it passes close to the compact object. In general only a small fraction of the wind is accreted, in contrast to the Roche lobe case, where almost all the mass is captured by the accreting component. Analytic and numerical treatments of the bow shock of a compact star moving with orbital velocity v in a stellar wind of velocity v_w show that that the wind material will be captured if it passes within a cylindrical radius

$$r_{acc} = \frac{2GM_1}{v_{rel}^2} \tag{2.9}$$

of a star, where $v_{rel}^2 = v_w^2 + v^2$ (see e.g. Bondi & Hoyle 1944; Blondin et al. 1990). If the wind is emitted over a solid angle Ω and has total mass loss rate $\dot{M}_w$ this implies an accretion rate

$$\dot{M} \sim \frac{\pi r_{acc}^2}{\Omega a} \dot{M}_w, \tag{2.10}$$

where a is the binary separation. In HMXBs containing OB supergiants, the winds are isotropic ($\Omega \sim 4\pi$) and have high velocities ($v_w \sim (1 \div 2) \times 10^3$ km s^{-1}). Thus, $r_{acc} \sim 10^{10}$ cm is much smaller

than the binary separation $a \sim 10^{12}$ cm, and only $\lesssim 10^{-4}$ of the matter lost by the companion is accreted.

The captured wind material has rather low specific angular momentum compared with mass overflowing the Roche lobe. So, it is difficult to decide whether the disk formation condition (2.7) is satisfied. An additional complication is that the accreting neutron star in many cases has a strong magnetic field, increasing the effective size of the accretor. Measuring the neutron star's spin period (X-ray pulsation period) usually allows to distinguish between cases where a disk does or does not form: if the disk is present the neutron star is often being spun up by the accreted matter. A hybrid situation is sometimes observed in binaries with very eccentric orbits, where accretion near periastron may result in the formation of the disk.

2.4 Accreting pulsars

2.4.1 Accretion onto a magnetized neutron star

As it was already mentioned, neutron stars can posses substantial magnetic moments ($\gtrsim 10^{30}$ G cm^3). If the magnetic pressure in the vicinity of the neutron star is comparable with the gas pressure, the accretion flow can be channeled onto restricted regions of the accreting star close to its magnetic poles. In this case the observed X-ray flux will be modulated with the spin period of the accretor, provided that the magnetic dipole axis of the neutron star does not coincide with its rotational axis (Lamb et al. 1973).

A measure of the relative strength of the magnetic field and the accretion flow is given by the Alfvén radius, defined as the radius R_A at which magnetic stresses would balances the ram pressure of a spherically symmetrical accretion flow (see e.g. Pringle & Rees 1972):

$$R_\mathrm{A} = \left(\frac{\mu^2}{2\dot{M}\sqrt{2GM}} \right)^{2/7}, \tag{2.11}$$

where M is the mass of the neutron star, μ is its dipole magnetic moment, $\dot{M}$ is the accretion rate. It should be noted that Eq 2.11 is a rough measure. The actual dynamics of the accretion flow depends on many factors such as the degree to which the matter is threaded by the field, plasma instabilities, and the field geometry. In order to show significant magnetic behavior at all (e.g. X-ray pulsations), R_A should be greater than the radius of the neutron star. This condition requires a typical surface field $\gtrsim 10^8$ G. If $R_\mathrm{A} < R_\mathrm{circ}$ (see Eq. 2.7) the accretion disk can form in the normal way. This condition usually holds in X-ray binaries with a neutron star (particularly where the companion overflows the Roche lobe). Generally one would expect the disk to be disrupted by the magnetic field at some radius of order of R_A. If this radius is too large the matter will be flung out by centrifugal forces and carry off specific angular momentum (Illarionov & Sunyaev 1975). This occurs if R_A exceeds the "corotational radius"

$$R_\mathrm{co} = \left(\frac{GMP_\mathrm{spin}^2}{4\pi^2} \right)^{1/3}, \tag{2.12}$$

where the field lines move with the local Kepler speed (P_spin is the spin period of the neutron star).

Beyond this bare description, there is no consensus on how or where the matter attaches to the field lines and flows to the neutron star surface, or on the interaction of the field with the disk

outside the disruption radius. In most approaches (see e.g. Ghosh & Lamb 1979; Wang 1987; Anzer & Börner 1983) the matter is assumed to leave the disk in a narrow transition zone at the inner edge (near R_A), thereafter flowing along magnetic field lines to the neutron star.

2.4.2 Accretion torques and spin period behavior

The spin of the accreting neutron star, and sometimes its rate of change are often readily observable through the X-ray pulsations, offering insight into the angular momentum flow in the system. Spin-up of the neutron star can take place if the accreted matter has an angular momentum due to orbital motion. In the case of disk accretion, the spinning-up torque $K_{\rm spin-up}$ can be presented as the flux of angular momentum transfered from the disk at the magnetospheric boundary, close to R_A (Pringle & Rees 1972):

$$K_{\rm spin-up} \simeq \dot{M}\sqrt{GMR_A}. \tag{2.13}$$

The narrower the transition zone in which the accreting matter is decelerated, the better is this estimate.

Matter falling onto the surface of the neutron star emits its gravitational energy in the form of radiation so that the luminosity of the accreting star, L_X, is proportional to the mass accretion rate $\dot{M}$. Using this relation as well as the equation $dI\omega/dt = K_{\rm spin-up}$ (I is the moment of inertia of the star, ω is its angular frequency) it can be shown that in this rough approximation

$$-\dot{P}_{\rm spin} \propto L_X^{6/7}. \tag{2.14}$$

A more realistic description would require a detailed model of disk-field interaction. Such a description should also take into account torques that tend to slow down the rotation of the neutron star. Such spin-down torques result mainly from the interaction of the field lines with parts of the accretion disk outside R_{co} (where the field lines move faster than the matter). Again, a detailed model is needed to specify these torques. A detailed discussion can be found in Ghosh & Lamb (1979); Wang (1987); Lipunov (1992).

2.4.3 X-ray spectrum

The energy spectrum of an X-ray pulsar is of a thermal nature. As mentioned above, most of the X-ray radiation in accreting pulsars is produced in small regions around the magnetic poles of the neutron star, where accreted matter hits the star's surface. This matter fills a subset of the magnetic dipole field lines close to the poles, in a configuration which is more or less azimuthally symmetric about the pole. This region is restricted on the outside by a roughly column-shaped surface which is usually referred to as the "accretion column" (Meszaros 1992). When the luminosity is in excess of $\sim 10^{37}$ erg s^{-1}, a radiative shock close to the surface will form where most of the radiation is produced (Basko & Sunyaev 1976). At lower luminosities the inflowing material is thermalized either by Coulomb interactions at the surface (Meszaros et al. 1980; Nelson et al. 1993) or by a collisionless shock (Langer & Rappaport 1982). The feasibility of a collisionless shock in a 10^{12} G magnetic field (typical for X-ray pulsars) is unknown, so most calculation have been concentrated on Coulomb interactions. Beaming along the magnetic field lines due to the anisotropy of the photon-scattering cross-section in a strongly magnetized plasma (see e.g. Basko & Sunyaev 1976) is responsible for the observed deep modulation of the X-ray flux with the spin period of the neutron star.

The observed X-ray spectra of accreting pulsars are characterized by a flat power law with a photon index, Γ, of 1.0–2.0 up to a high-energy cutoff at 10–25 keV, above which the spectrum decays more steeply. Such a shape of the spectrum indicates that comptonization plays an important role (see e.g. Rybicki & Lightman 1979). The spectrum above the high-energy cutoff, $E_{\rm cutoff}$, is often approximated by the function $\exp[(E_{\rm cutoff}-E)/E_{\rm fold}]$, where $E_{\rm fold}$ is the e-folding energy (see e.g. White et al. 1983). Typical values for $E_{\rm cutoff}$ and $E_{\rm fold}$ both lie in the range 10–25 keV. A soft excess is sometimes seen below 1 keV, which may represent thermal emission from hot material in the magnetosphere (e.g. Her X-1, McCray et al. 1982).

The Teragauss magnetic field at the magnetic poles of the neutron star can affect the X-ray spectral continuum of the escaping radiation. The kinetic energies of the plasma electrons in such a strong B-field are quantized perpendicular to the field lines in discrete Landau levels (Meszaros 1992; Daugherty & Harding 1986):

$$E_c = m_{\rm e}c^2\left(\sqrt{1+2n\frac{B}{B_{\rm crit}}}-1\right), \tag{2.15}$$

where $m_{\rm e}$ is the electron rest mass, c is the speed of light, and $B_{\rm crit} = e^2c^3/(e\hbar) \sim 4.4\times10^{13}$ G – the critical field strength when the de Broglie radius of a plasma electron becomes comparable to its Larmor radius. For $B << B_{\rm crit}$ the energy spacing between these levels is given by

$$E_c \simeq \frac{\hbar eB}{m_{\rm e}c} \simeq 11.6\frac{B}{10^{12}\,{\rm G}}\,{\rm KeV}. \tag{2.16}$$

Photons with energies of $\sim nE_c$ ($n = 1, 2, 3...$) undergo resonant scattering with the Landau electrons. These photons are trapped in the dense plasma of the accretion column, being absorbed, re-emitted or spawned and absorbed again by the Landau electrons. The trapped photons may escape once their energy has changed sufficiently from the resonant Landau energies. As a result line-like features arise in the observed X-ray spectrum of a pulsar close to the Landau line energies E_c (the fundamental), $2E_c$ (first harmonic), $3E_c$ (second harmonic) etc. The observed line energy is subject to gravitational redshift z, such that the magnetic field strength may be estimated by

$$B_{12} \simeq \frac{(1+z)E_c^{\rm (obs)}}{11.6\,{\rm keV}}, \tag{2.17}$$

where $B_{12} = B/10^{12}$ G. The gravitational redshift at the neutron star surface is approximately

$$z = \left(1-\frac{2GM}{mc^2}\right)^{-\frac{1}{2}}-1, \tag{2.18}$$

where M and R are the mass and radius of the star.

The discovery of the cyclotron feature in the spectrum of Her X-1 in 1976 (Trümper et al. 1978) provided the first "direct measurement" of the magnetic field strength of a neutron star, in the sense that no other model assumptions are needed. Originally considered as an exception, cyclotron features are now known to be rather common in accreting X-ray pulsars, with more than a dozen binary pulsars now being confirmed cyclotron line sources (Coburn et al. 2002; Heindl et al. 2004).

Many X-ray pulsars exhibit the Fe K_α fluorescent emission line at ~6.4 keV. Such a line is believed to be produced when the optically thick material at the inner edge of an accretion disk is externally illuminated by hard X-rays from the central source (Basko 1980).

Chapter 3

Her X-1/HZ Her: intermediate mass X-ray binary

3.1 System overview

Hercules X-1 is one of the first X-ray pulsars discovered by the *Uhuru* satellite in 1972 (Tananbaum et al. 1972; Giacconi et al. 1973), and since then remains one of the most studied X-ray sources. The basic phenomenological picture of Her X-1 was established soon after its discovery: a close binary system consisting of an accreting magnetized neutron star with a 1.24 s spin period and a stellar companion HZ Her (first suggested by Liller 1972) – a main sequence star of the spectral type A/F (Crampton 1974). The mass of the optical companion is $\sim 2 M_{\odot}$ which places the system in the middle between high and low mass X-ray binaries. The orbital period of the system is ∼1.7 days. The binary orbit is almost circular and has an inclination $i \sim 85 - 88^{\circ}$ (Gerend & Boynton 1976). Since we see the orbit nearly edge-on, the X-ray source is regularly eclipsed by the optical companion for ∼5.5 h once per orbital revolution. The X-ray luminosity of the source is $L_{\rm X} \sim 2 \times 10^{37} \mathrm{erg\,s^{-1}}$ for a distance of ∼7 kpc found by Reynolds et al. (1997). Assuming that the radiative efficiency of the accretion is ∼10% ($L \sim 0.1 \dot{M} c^2$), such $L_{\rm X}$ corresponds to a mass accretion rate to the neutron star $\dot{M} \sim 2 \times 10^{17} \mathrm{g\,s^{-1}}$. The optical companion, HZ Her, provides a classical example of the *reflection* effect – strong orbital modulation in the optical range caused by a powerful illumination of the part of the normal star atmosphere facing the X-ray source (Bahcall & Bahcall 1972; Cherepashchuk et al. 1972).

Already, the very first *Uhuru* observations of Her X-1 revealed the presence of a long-term ∼35 d periodicity which manifests itself mainly through the alternation of so-called *on* (high X-ray flux) and *off* (low X-ray flux) states (see Fig. 4.15). The 35 d cycle contains two *on* states – the *main-on* (∼7 orbital periods) and the *short-on* (∼5 orbital cycles) – separated by ∼4–5 orbital cycles. The maximum X-ray flux of the main-on is roughly five times higher than that in the maximum of the short-on. Sometimes Her X-1 exhibits so-called *anomalous low states* where X-ray flux is strongly reduced and 35 d variability is seen only marginally (Parmar et al. 1985; Vrtilek et al. 1994; Parmar et al. 1999). The maximum X-ray flux during the anomalous low state is only 1–3% of the main-on flux.

The long-term periodicity in Her X-1/HZ Her is usually attributed to the counter-orbitally precessing tilted and warped accretion disk around the neutron star (see e.g. Gerend & Boynton

1976; Howarth & Wilson 1983; Shakura et al. 1999). Since the inclination of the binary orbit is close to 90°, we see the orbital plane nearly edge-on. The precessing warped disk, therefore, covers the central X-ray source during a substantial portion of the 35 d precessional cycle. The anomalous low states are most probably due to the reduction of the tilt of the outer disk to the system orbital plane, such that the X-ray source is permanently blocked. This hypothesis is supported by the fact that the amplitude of optical pulsations of the normal companion is only slightly reduced during anomalous low states, indicating that the X-ray illumination of the companion persists (Vrtilek et al. 1994). The mass accretion onto the neutron star, therefore, does not stop during these states.

As one can see, Her X-1 experiences strong variability on very different time scales and has many intriguing properties. Below we discuss in more details the most remarkable observational features of the system which are related to this work.

3.2 Observational properties

3.2.1 35 d period

The 35 d periodicity is one of the most enigmatic features of Her X-1. As mentioned above, it manifests itself mostly through the modulation of the X-ray light curve of the source (see Figs. 4.5 and 4.15). The sharp transition from the *off* state to the main-on state is called X-ray *turn-on* of the source and is usually used to count 35 d cycles. Transition from the *off* state to the short-on state is sometimes called *secondary* X-ray turn-on. Each observation hence can be characterized by the 35 d phase (*precessional* phase). Phase zero is usually assumed to correspond to the moment of turn-on of the source. The 35 d periodicity is also seen in systematic changes of the shape of 1.7 d optical pulsations (see e.g. Boynton et al. 1973; Gerend & Boynton 1976) and of the 1.24 s X-ray pulsations (Trümper et al. 1986; Soong et al. 1990b; Deeter et al. 1998; Ketsaris et al. 2000, see also Section 3.2.3).

The 35 d period is not stable. Already after a few turn-ons had been observed by *UHURU* it was noted that the source always turns on in two bands of orbital phases: $\phi_{\rm orb} \sim 0.2$ and 0.7 (Giacconi et al. 1973). As a result, the duration a of 35 d cycle is always a half-integer number of orbital cycles. Observations show that the 35 d period stochastically changes from cycle to cycle and in most cases is equal to 20, $20\frac{1}{2}$, or 21 orbital periods $P_{\rm orb}$ (Staubert et al. 1983; Shakura et al. 1998a).

The behavior of the 35 d period is usually explored by means of the so-called $(O-C)$ diagram which shows the difference between the observed and calculated times (assuming a constant period) of the turn-on as a function of time (or 35 d cycle number). It is, therefore, a representation of the history of the 35 d period. Figure 3.1 shows part of the historical $(O-C)$ diagram of Her X-1. A straight line on this diagram would correspond to a constant period. The value of the period would be determined by the slope of the line (going up means a larger turn-on period, going down – shorter). Almost all observed turn-ons of Her X-1 fall on parallel horizontal lines separated by $0.5 \times P_{\rm orb}$ reflecting the fact that the time interval between turn-ons is a half-integer number of orbital cycles. Since the time interval between two successive turn-ons is always 20, $20\frac{1}{2}$, or 21 (see above), the "wandering" of $(O-C)$ is in such a way, that it never jumps by more than $0.5 \times P_{\rm orb}$ from one cycle to the next. The cycle counting as well as the zero point of $(O-C)$ are arbitrary. In our work the zero point is chosen to be the turn-on at MJD = 41501.149. We assign to the corresponding 35 d cycle the number 5 (in Staubert et al. (1983) the zero point of $(O-C)$ was

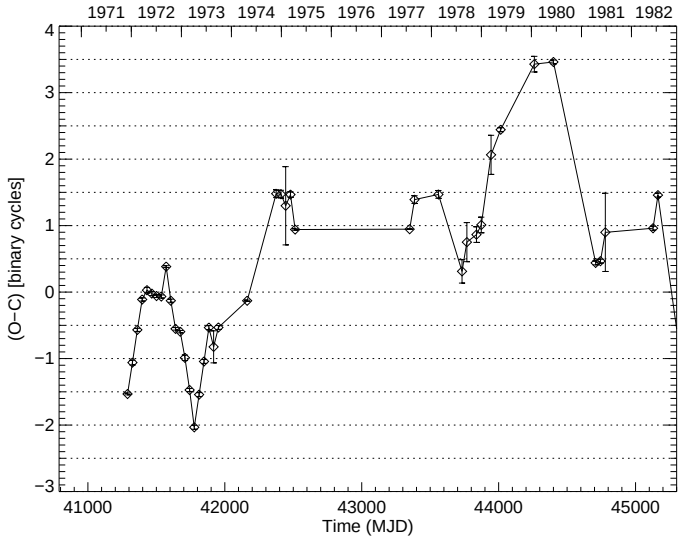

Figure 3.1 Part of the historical $(O-C)$ diagram of Her X-1. Almost all observed turn-ons fall on parallel horizontal lines separated by $0.5 \times P_{\rm orb}$.

chosen to be at MJD = 42409.849, close to the turn-on of the cycle No. 31 and differs from our $(O-C)$ by $1.5 \times P_{\rm orb}$, so that $(O-C)_{\rm Staubert(1983)} = (O-C) - 1.5 \times P_{\rm orb}$).

It has been shown that that the observed behavior of $(O-C)$ can be described by a *random walk* model with all three possible periods being about equally probable (Staubert et al. 1983; Ögelman 1987; Baykal et al. 1993). The average long term turn-on period in such a model would be identical to $20.5 \times P_{\rm orb}$ implying some sort of physical lock over long time between the 35 d period and the orbital period. However, with todays data base of turn-ons, almost three times as long and more densely populated (especially in the last 10 years due to *BATSE CGRO* and the *ASM RXTE*) this model has to be modified. The modulation in $(O-C)$ appears not to be entirely random but follows quasi-periodic variations with the period of several years (Staubert et al. 2006). We now believe that the global long-term developments in $(O-C)$ cannot be explained by a random walk. They probably involve quasi-periodic variations in mass transfer from the normal companion.

3.2.2 X-ray dips

Even more interesting features observed in Her X-1 are sudden decreases in X-ray flux accompanied by significant spectral changes – X-ray dips. They have been observed by many satellites: *UHURU* (Giacconi et al. 1973; Jones & Forman 1976), *Copernicus* and *Ariel V* (Cooke & Page 1975; Davison & Fabian 1977), *Ariel VI* (Ricketts 1982), *OSO-7, OSO-8*, (Crosa & Boynton 1980), HEAO-1, (Gorecki et al. 1982), *Tenma*, (Ushimaru et al. 1989), *EXOSAT*, (Reynolds & Parmar 1995), *Ginga*, (Choi et al. 1994; Leahy et al. 1994; Leahy 1997),*RXTE*, (Shakura et al. 1998a; Scott & Leahy 1999). X-ray dips are usually separated into three groups: *pre-eclipse dips*, which are observed once per orbital cycle and march from a position close to the eclipse toward earlier orbital phase in successive orbits; *anomalous dips*, which are observed at orbital phase $\phi_{\rm orb}$ = 0.45 – 0.65 during the first one or two orbits after turn-on (of the main on as well as of the short-on) and *post-eclipse recoveries*, which are occasionally observed as a short delay (up to a few hours) of the egress from the X-ray eclipse in the first orbit after turn-on. Examples of all three types of

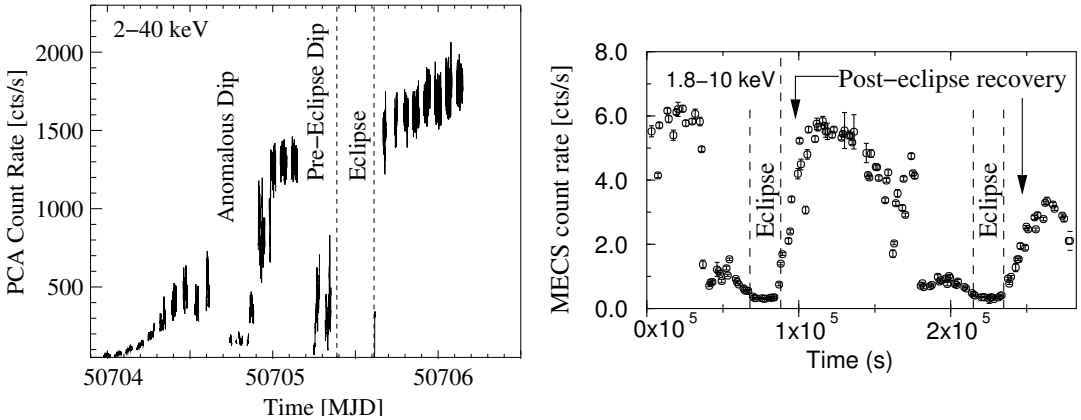

Figure 3.2 Anomalous and pre-eclipse dips observed by *PCA RXTE* during a main-on *(left panel)* and post-eclipse recoveries observed by *MECS BeppoSAX* during a short-on *(right panel)*. The pictures are taken from Kuster et al. (2005) and Oosterbroek et al. (2000), respectively.

dips are shown in Figure 3.2. The transition into a dip takes place quite sharply (at times as short as tens of minutes), similar to the transition into eclipse. However, the X-ray flux can have a finite value within the dip. The duration of the dips is on the average of the same order as the eclipse duration, but can vary from one dip to another. The dips are usually interpreted as being due to absorption of X-rays by intervening gas. This interpretation is based on the spectral data: during the dips the X-ray spectrum shows significant low-energy absorption with the typical column density of 10^{23} atom cm^{-2} (Giacconi et al. 1973).

Several physical models have been proposed to explain the properties of the X-ray dips. For example, in many models (Crosa & Boynton 1980; Gorecki et al. 1982; Leahy 1997; Schandl 1996) the dips are caused by thickening of the outer rim of the accretion disk due to interaction with the accretion stream; Vrtilek & Halpern (1985) suggested that the dips are produced by the accretion stream which is thicker than the disk (see also Bochkarev & Karitskaia 1989). However, these models made various assumptions about the disk parameters (for example, in the original model by Crosa and Boynton the disk size was uncomfortably large to explain the X-ray dip marching behavior). In our model, first elaborated by Shakura et al. (1999), pre-eclipse dips and some of the anomalous dips are produced by the accretion stream that moves out of the system's orbital plane. Most of the anomalous dips and all post-eclipse recoveries are caused by the wobbling outer part of the disk. We describe this model in more detail in Sections 3.3 and 4.4.2.

3.2.3 X-ray pulse profiles

The basic features of X-ray pulsations in Her X-1 like in other X-ray pulsars are normally explained by the oblique rotator model (Lamb et al. 1973) where X-ray emission comes from two magnetic poles of a highly magnetized rotating neutron star, whose rotation axis does not coincide with the magnetic axis. The detailed shape of the X-ray pulse profile, however, is quite complicated and can be decomposed into several distinct components (up to eight). Like in many other X-ray pulsars, the X-ray pulse profile of Her X-1 is energy-dependent. Different components of the profile vary with energy in a different way. Thus, the energy-dependence can be used to separate

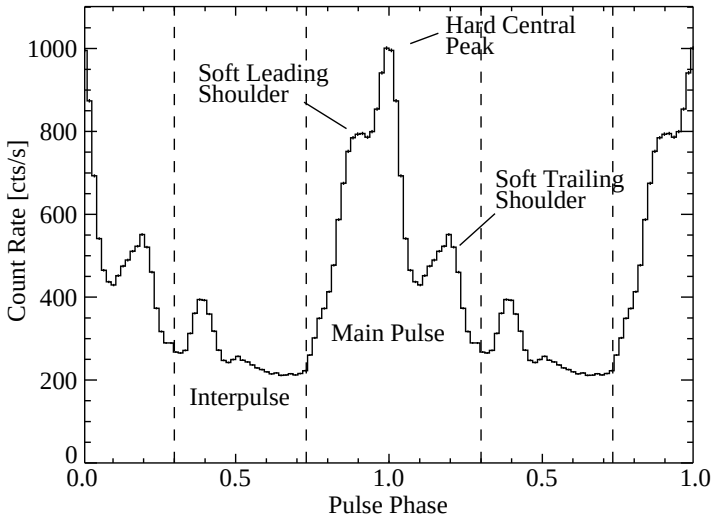

Figure 3.3 An example of Her X-1 X-ray pulse profile in the 9–13 keV energy range obtained with *PCA RXTE* during a main-on state. The picture is taken from Kuster et al. (2005).

components. A typical X-ray pulse profile of Her X-1 with adopted nomenclature for different features is shown in Figure 3.3.

Soon after the discovery of the source it was noted that the pulse profile experiences systematic variations with time (respective to the 35 d phase, see Fig. 3.4). Such variations have been found in data from *HEAO-1* (Soong et al. 1990b), *EXOSAT* (Trümper et al. 1986; Kahabka 1989), *Ginga* (Deeter et al. 1998; Scott et al. 2000), *RXTE* (Scott et al. 2000). Two basic models have been proposed to explain these variations. Trümper et al. (1986) interpreted them in terms of a freely precessing neutron star. In the course of the precession viewing conditions of the magnetic poles on the star surface change giving rise to the systematic variation of the pulse profile. Scott et al. (2000); Sheffer et al. (1992), however, argued that not free precession, but rather progressive occultation of the X-ray source by the inner edge of the precessing accretion disk is responsible.

3.2.4 Cyclotron line

The X-ray spectrum of Her X-1 is characterized by a power law continuum with exponential cut-off and an apparent line-like feature, which was discovered in 1976 (Trümper et al. 1978). This line is now generally accepted as an absorption feature due to resonant scattering of photons off electrons on quantized energy levels (Landau levels) in the Teragauss magnetic field at polar caps of the neutron star. The feature is therefore often referred to as a *cyclotron line* or *cyclotron resonant scattering feature* (CRSF). As described in Section 2.4.3, cyclotron lines provide a direct method of measuring the magnetic field strength at the site of the emission of the X-ray spectrum: $B_{12} = (1+z)E_{\rm cycl}/11.6\,{\rm keV}$, where B_{12} is the magnetic field strength in units of 10^{12} G, z is the gravitational redshift, and $E_{\rm cycl}$ is the measured energy of the cyclotron line centroid. Her X-1 was the first neutron star for which the direct measurement of the strength of the Teragauss magnetic field was obtained. The line was observed at ~40 keV. This gave an estimate of the field strength of $B \sim 3 \times 10^{12}$ G.

Repeated observations of Her X-1 with *RXTE* and *BeppoSAX* have shown that the line energy (pulse-averaged) was relatively stable (~5%) since 1996 (Gruber et al. 2001; Dal Fiume

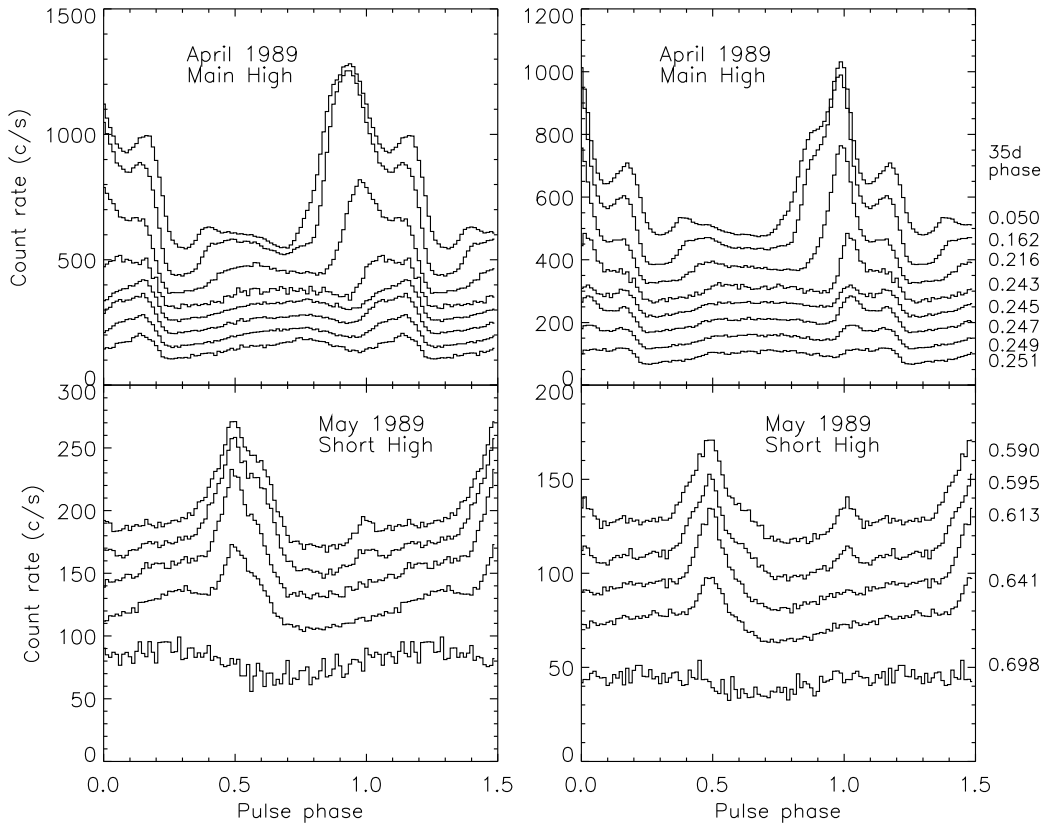

Figure 3.4 X-ray pulse profiles of Her X-1 observed with *Ginga* as a function of 35 d phase $\phi_{\rm pre}$ (Scott et al. 2000). $\phi_{\rm pre}$ = 0 corresponds to the X-ray turn-on of the source.

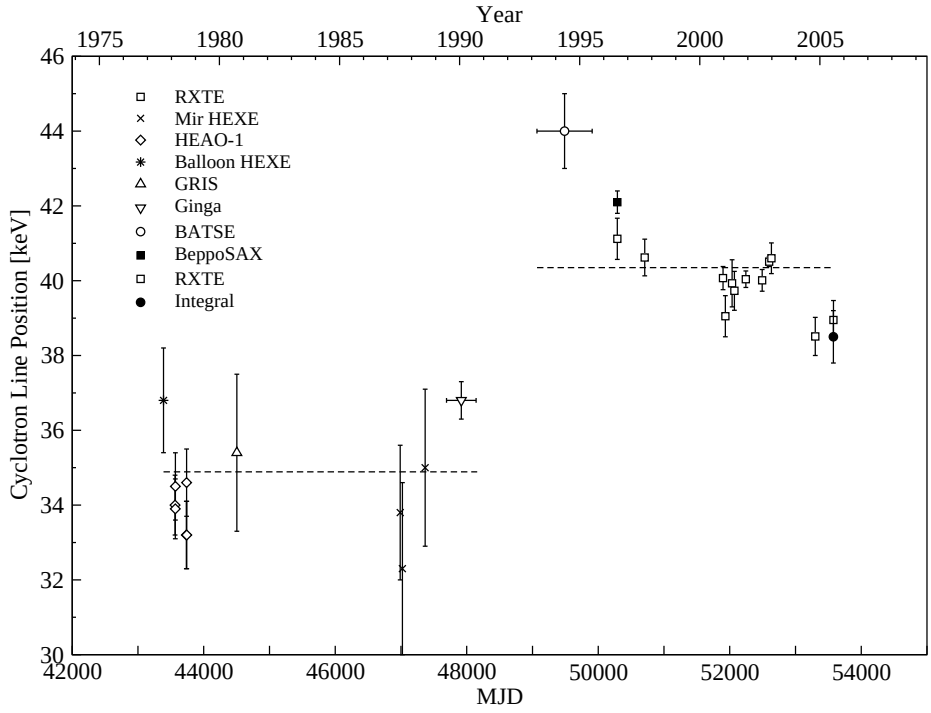

Figure 3.5 The centroid energy of the phase averaged cyclotron line in Her X-1 since its discovery. Dashed lines are mean cyclotron line energies before and after 1991 (see Staubert et al. 2007b, and references therein).

et al. 1998). When these data are compared to the previous observations (including historical data reaching back to the discovery of the line in 1976), however, an apparent jump in the line energy from ~34 to ~42 keV appears somewhere between 1991 and 1993 (Fig. 3.5). Although a comparison of measurements from different instruments is difficult because of systematic uncertainties due to calibration and analysis techniques, we believe that the large difference of ~5 keV between the mean values and the relative internal consistency within the two groups of data most likely indicate real physics.

Since the early observations, it has been known that the line parameters and (to a lower degree) the spectral continuum parameters are variable with the 1.24 s pulsation phase (Voges et al. 1982; Voges 1985; Soong et al. 1990a). This variability is usually attributed to the change of viewing direction of the complex emitting region (formed by the magnetic field including higher multipole components) with the rotational angle of the neutron star corresponding to the 1.24 s pulse phase. The pulse phase resolved spectra had, however, relatively poor statistics, especially at higher energies.

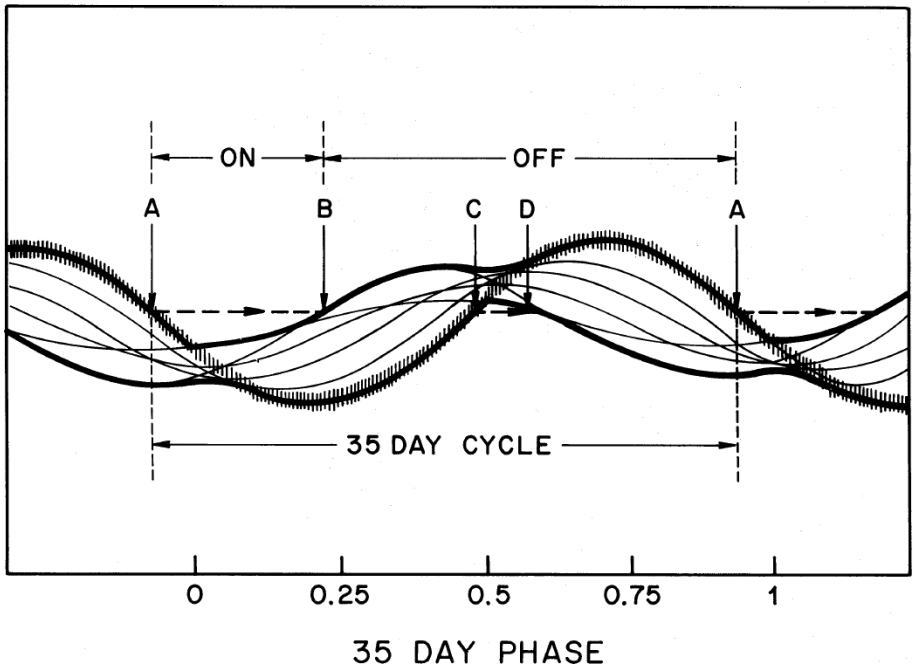

Figure 3.6 Panoramic view of the disk as seen from the neutron star. The outermost disk ring is identifiable by a fuzzy band. The horizontal dashed line shows the position of the observer at different moments in the 35 d cycle. Easily identifiable features are the main-on state (A–B), the short-on state (C–D), and off-states (B–C and D–A). Low-energy absorption is expected when the outermost ring crosses the dotted line (points A and C). The picture is taken from Petterson (1977).

3.3 Model and open questions

Despite the fact that the general properties of the Her X-1/HZ Her system are understood, we are far from having a final picture available. For example, even the basic question about the nature of the driver of the 35 d cycle is yet to be answered. Below we describe the model of the system which we adopted at the beginning of our research. Our main goals were to improve and to test different aspects of this model by analyzing the X-ray data obtained with *RXTE* and *INTEGRAL*.

As mentioned in Section 3.1, the main ingredient of the model is the counter-orbitally precessing tilted and warped accretion disk around the neutron star. The 35 d modulation of the X-ray light curve is believed to be caused by periodic obscuration of the X-ray source by the disk. The main-on state starts when the outer disk rim opens the line of sight to the source (Fig. 3.6). Subsequently, at the end of the main-on state the inner part of the disk (that may be surrounded by a hot rarefied corona) covers the source from the observer. This picture seems to be confirmed by spectral analysis. The opening of the X-ray source is accompanied by notable spectral changes including evidence for the presence of a strong absorption, whereas the decrease in X-ray intensity occurs more slowly and without appreciable spectral changes (Giacconi et al. 1973; Kuster et al. 2005, see however Oosterbroek et al. 2000).

The fact that X-ray turn-ons always occur near orbital phases $\phi_{\rm orb} \simeq 0.2$ or 0.7 has been

explained by Levine & Jernigan (1982) and Katz et al. (1982). These authors assumed that the disk undergoes a wobbling twice the synodal orbital period due to tidal torques. Calculations show that due to the wobbling the angle between the disk plane and the observer's line of sight at $\phi_{\rm orb} \simeq 0.2$ and 0.7 changes most rapidly.

The origin of all three types of X-ray dips was successfully explained by Shakura et al. (1999). In their model pre-eclipse dips occur when the accretion stream crosses the observer's line of sight before entering the disk. This can happen only if the stream is not coplanar to the system's orbital plane. The reason for the stream to move out of the orbital plane is non-uniform X-ray heating of the optical stars atmosphere by the X-ray source, which produces a temperature gradient near the inner Lagrangian point. The non-uniformity of the heating comes from the partial shadowing of the optical star surface by the accretion disk. Furthermore, such a stream forces the outer parts of the accretion disk to be tilted with respect to the orbital plane. The tidal torques cause the disk to precess in the direction opposite to the orbital motion. Due to tidal torques and the dynamical action of the accretion stream the outer parts of the disk develop a notable wobbling motion twice the synodal orbital period. For an observer, the X-ray source can be screened by the outer parts of the disk for some time during the first orbit after the X-ray turn-on. This causes anomalous dips and post-eclipse recoveries.

Acting alone, tidal forces would result in a precessional period of the disk somewhat shorter than observed. To explain the observed precessional period (about $20.5 P_{\rm orb}$), braking torques must be added. According to the stream-disk coupling model of Shakura et al. (1999), the motion of the outer parts of the disk is driven by the joint action of tidal forces and dynamical pressure induced by the impact of the gas stream on the accretion disk. The dynamical action of the gas stream over one binary period is opposite to the tidal force so the streams can slow down the tidal precession to the observed value.

As mentioned in Section. 3.2.3, the observed shape of 1.24 s pulse profile is quite complicated and asymmetric. In addition, it shows apparent systematic variations with 35 d phase. The variations seen towards the end of the main-on state have recently been studied by Scott et al. (2000) and explained by obscuration of the emitted X-ray beams by the hot inner part of the accretion disk. There is, however, a severe problem with this interpretation: it requires an extremely small radius of the (absorbing) inner part of the accretion disk which appears to be inconsistent with estimates for this radius from accretion torque theory. In this work we adopt the alternative explanation of the pulse shape variation, which assumes free precession of the neutron star (Kahabka 1987, 1989; Prokhorov et al. 1990; Shakura et al. 1998b; Ketsaris et al. 2000; Wilms et al. 2003). According to our current understanding, the observed pulse profiles are formed by a superposition of pencil-beam type emission components from the spots at the magnetic poles as well as from arc-like structures around the poles (the latter are due to higher-multipole components of the star's magnetic field). As we sweep through pulse phase (corresponding to the rotational orientation of the NS) different emission components add up to give the local flux at any phase. During free precession of the star viewing conditions of different emission regions are changing giving rise to the systematic variations of the observed pulse profile with 35 d phase.

If a rotating neutron star is not spherically symmetric but slightly elongated or contracted along a particular direction which is neither parallel nor perpendicular to its spin axis then it will undergo free precession. Figure 3.7 illustrates the geometry of the freely precessing neutron star adopted for Her X-1. $\boldsymbol{\omega}$ shows the angular momentum of the neutron star which almost coincides with its spin axis. In addition to the spin motion with the period of 1.24 s the star slowly rotates

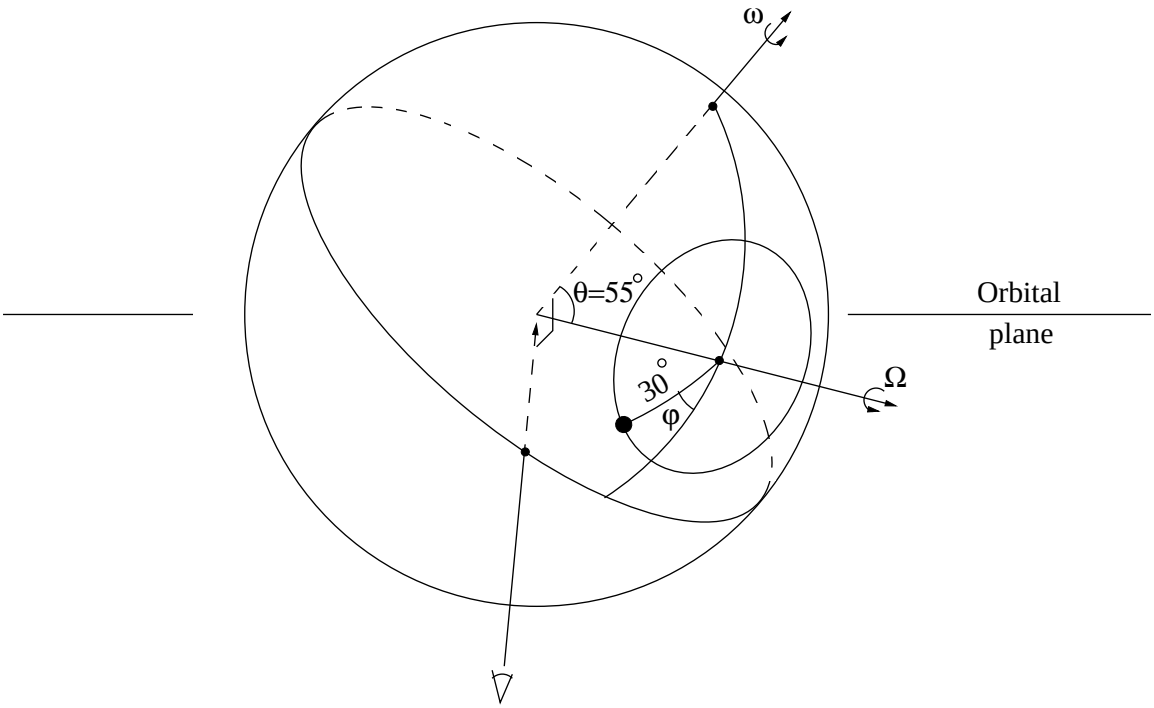

Figure 3.7 The schematic representation of the precessing neutron star geometry. $\boldsymbol{\omega}$ is the angular momentum of the neutron star. $\boldsymbol{\Omega}$ indicates the principal axis of inertia around which the star slowly precesses with the period of ~35 days (see text). The indicated values for the angles are estimated from the preliminary modeling of Her X-1 pulse profiles performed by the Moscow group.

around its axis of symmetry (marked by $\boldsymbol{\Omega}$). The orientation of the symmetry axis with respect to the spin axis is characterized by the nutation angle θ. The magnetic pole (black spot in Figure 3.7) rotates around the axis of symmetry with the period of free precession (~35 d). The phase of the precession is characterized by the angle ϕ. The preliminary modeling of Her X-1 pulse profiles observed with *RXTE* performed by the Moscow group (K. Postnov, priv. comm.) showed that the spin axis of the neutron star is almost perpendicular to the line of sight, the nutational angle $\theta \sim 55°$, and the angular distance from the symmetry axis to the magnetic pole is $\sim 30°$. The inclination of the spin axis to the orbital plane cannot be found from the model. In the picture it is arbitrarily chosen to be $\sim 40° - 50°$ in the plot.

The angle ϕ represents the precessional phase of the neutron star itself. This phase can be different from the 35 d phase defined by turn-on moments (i.e. by the precession of the accretion disk) and represent a rather stable clock. According to our model, the precessing neutron star is coupled to the inner part of the accretion disk whose orientation is affected by the neutron star magnetosphere. During the precession of the star the orientation of the inner disk rim changes. This produces systematic variations in the shadow pattern on the irradiated atmosphere of the normal companion. The shadows affect the temperature gradient near the inner Lagrangian point and, therefore, the direction of the accretion stream (see above). The stream, in turn, governs the precession rate of the accretion disk. This coupling is relatively loose allowing the disk to "wander"

in phase with respect to the uniformly precessing neutron star. Last modeling of the Her X-1 X-ray pulse profiles has shown that the precessional phase of the neutron star determined from the profiles indeed changes with respect to the precessional phase of the accretion disk determined by turn-ons. This fact provides further support to the model of free precession. For an alternative model see Schandl & Meyer (1994).

The described picture is not complete and has a number of difficulties. Although the presence of free precession has been reported for a number of pulsars (Crab, Vela, B1642-03, B1828-11; see Jones & Andersson 2001, for a review), there are strong theoretical arguments against free precession of neutron stars. The superfluid interior of a rotating neutron star is thought to be pinned with the crust nuclei (Anderson & Itoh 1975). The pinning effectively suppresses free precession (Shaham 1977; Sedrakian et al. 1999). Another effect is the strong interaction of the core's vortices and magnetic flux tubes, which also should shorten free precession periods (Ruderman 2001). The hypothesis of free precession, therefore, needs further observational confirmations.

The idea of the accretion stream – disk coupling proposed by Shakura et al. (1999) also needs to be tested. This can be done for example by exploring correlations in the long-term behavior of $(O - C)$ and spin period of the neutron star (Section 4.3.4). The numerical model of the disk wobbling presented by Shakura et al. (1999) should be modified in order to account for the new data obtained by the *ASM RXTE* (Section 4.4).

A number of open questions are related to the X-ray spectrum of Her X-1, especially to the cyclotron absorption feature around 40 keV. A negative correlation between the pulse averaged energy of the cyclotron line and X-ray luminosity has recently been reported for a number of transient sources (Mihara et al. 1998; Tsygankov et al. 2006, 2007a). For Her X-1, however, so far no clear relation between the cyclotron line energy and X-ray flux of any kind had been found (see e.g. Mihara et al. 1998; Gruber et al. 2001). In this work we report a positive correlation of the two values in Her X-1 (see Section 4.3.5 and Staubert et al. 2007b). Change of the viewing angle due to rotation of the neutron star around the axis which is inclined to the B-field axis should cause not only a change in flux (pulse profile) but also a change in the position and shape of the CRSF. This effect, although has been observed earlier on in Her X-1 (see above), needs further study using the new instruments with higher sensitivity and spectral resolution, such as *INTEGRAL* and *RXTE*. We also note that free precession (if it takes place in Her X-1) would modulate the pattern of changing of the CRSF position and shape across the pulse phase with 35 d period. This can be potentially verified by pulse-resolved spectroscopy performed for sufficiently large number of 35 d phases. Any new observation allowing pulse-resolved spectral analysis would essentially contribute to this study.

Chapter 4

RXTE observations of Her X-1

Her X-1 was repeatedly observed by the *Rossi X-ray Timing Explorer (RXTE)* in 1996–2005. The observations provided high-quality X-ray spectral and timing data. The *All Sky Monitor (ASM)* aboard the satellite performed almost uninterrupted monitoring of the 2–12 keV flux of the source. In this Chapter we use these data to probe various aspects of the system.

4.1 *Rossi XTE*: mission overview

The *Rossi X-ray Timing Explorer* was launched on December 30, 1995. The satellite is designed to explore the variability of X-ray sources using its good time resolution in combination with moderate spectral resolution. Time scales from microseconds to months are covered in a wide energy range from 2 to 250 keV. Originally designed for a required lifetime of two years with a goal of five, *RXTE* has passed that goal and is still performing well. The mission carries two pointed instruments, the *Proportional Counter Array* (*PCA*, Jahoda et al. 1996) which covers the lower part of the energy range (3–20 keV), and the *High Energy X-ray Timing Experiment* (*HEXTE*, Rothschild et al. 1998) covering the upper energy range (18–250 keV). These instruments are equipped with collimators yielding a FWHM of one degree. In addition, *RXTE* carries an *All-Sky Monitor* (*ASM*, Levine et al. 1996) that scans about 80% of the sky every orbit, allowing monitoring at the shortest time scales of 90 minutes (and longer). Data from the *PCA* and the *ASM* are processed on board by the Experiment Data System (EDS). The spacecraft is operating in a low-earth circular orbit at an altitude of 580 km, corresponding to an orbital period of about 90 minutes. This allows half-an-hour uninterrupted pointed observations separated by Earth occultations. The *RXTE* spacecraft allows extremely flexible observations, often making more than 20 discrete and scientifically motivated pointings within a day. The data modes are selectable, allowing compression which is required for bright objects (due to downlink bandwidth) to be performed in a user selected way. A diagram of the spacecraft is shown in Figure 4.1.

4.1.1 Proportional counter array

The Proportional Counter Array aboard the *Rossi XTE* consists of 5 nominally identical proportional counter units (PCUs) designed to perform observations of bright X-ray sources with high timing and modest spectral resolution. Each PCU has a net geometric collecting area

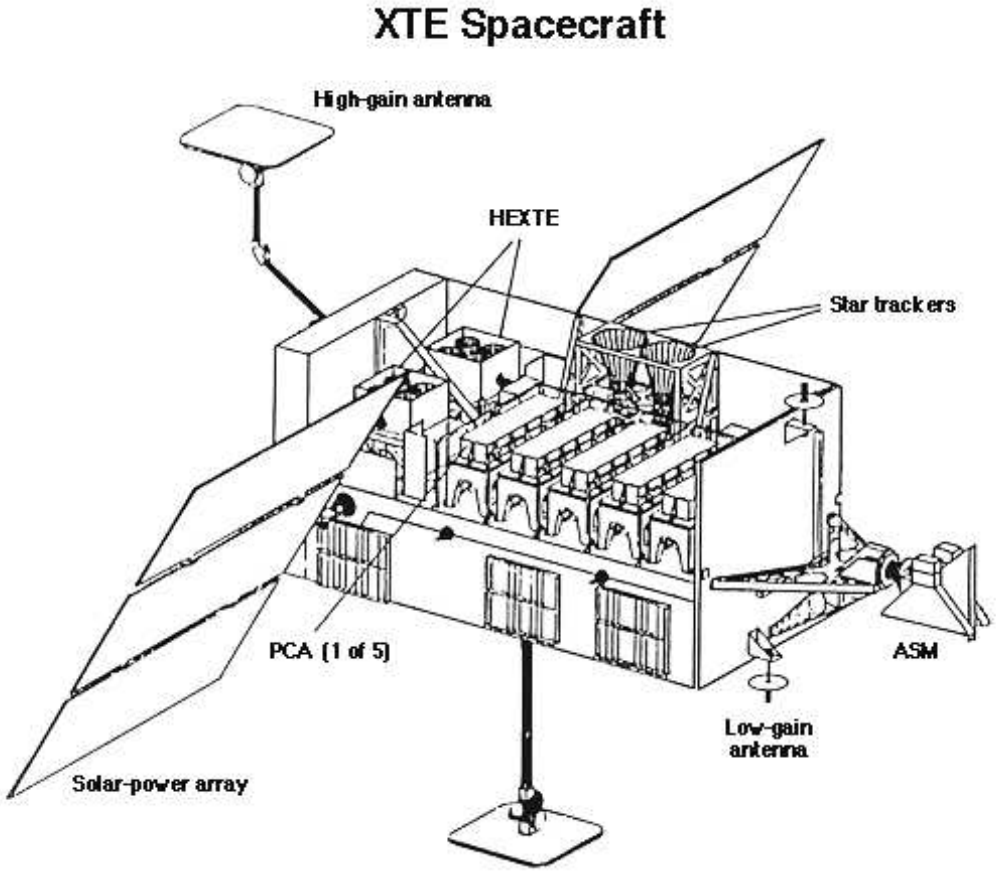

Figure 4.1 Diagram of the *RXTE* spacecraft, with instruments labeled.

of 1600 cm^2. With a 1°-collimator (FWHM) and well modeled background, the *PCA* is limited at fluxes of $\sim 4\times10^{-12}$ erg s^{-1} in the 2–10 keV band for an observing time of 10^5 s (approximately 0.3 count sec^{-1} PCU^{-1}). The detectors consist of a mechanical collimator, an aluminized mylar window, a propane filled "veto" volume, a second mylar window, and a Xenon filled main counter. There are three layers of Xenon cells, and each layer is divided in half by connecting alternate cells to either the "right" or "left" amplifier chain. The "left" and "right" chains are in mutual anticoincidence. The division of each layer is significant for data screening and background suppression. Every event, whether due to background or a cosmic source, is analyzed by EDS which applies a time-tag and performs event selection and (multiple) data compressions. Basic instrument characteristics of *PCA* are summarized in Table 4.1.

4.1.2 *HEXTE* detectors

The *HEXTE* instrument consists of two independent clusters of detectors, each containing four NaI(Tl)/CsI(Na) phoswich scintillation counters collimated by a lead honeycomb. Both clusters can rotate to either ±1.5° or ±3° about the nominal source-pointing direction of *RXTE*. The two clusters are oriented such that the axes of their rocking motions are mutually orthogonal. This enables the sampling of four background positions about the source pointing. The net open area of the eight detectors is $\sim$ 1600 cm^2, and each detector covers the energy range 15–250 keV with an average energy resolution of 15.4% FWHM at 60 keV. The cluster organization for the *HEXTE* instrument permits effective immunity to systematic background variations through the use of continuous gain control, chopping of the source signal, and anticoincidence shielding of charged particle events. The energy, time of arrival, and pulse shape associated with each detected photon are measured and digitized. For sources weaker than the Crab Nebula, all of this information may be telemetered to the ground. For very bright sources the processor has two binned analysis modes to permit considerable flexibility in data formatting and compression in order to achieve the timing and energy resolution requirements for source observations consistent with efficient data recovery. The *HEXTE* instrument is sensitive to X-ray fluxes on timescales from milliseconds to days, limited only by the telemetry and the source intensity. *HEXTE* is capable of measuring a typical, weak (~1 mCrab) X-ray source to 100 keV or greater in 10^5 live seconds, i.e., it has a 3σ sensitivity of 10^{-6}photons cm^{-2} s^{-1} keV^{-1} in a 20 keV band at 100 keV (for an observing time of 10^5 s). Basic instrument characteristics of *HEXTE* are summarized in Table 4.1.

4.1.3 All sky monitor

The *ASM* instrument consists of three Scanning Shadow Cameras (SSCs) mounted on a motorized rotation drive. Each SSC contains a one-dimensionally position-sensitive proportional counter (PSPC) that views the sky through a one-dimensional coded mask. The PSPC is used to measure the displacements and strengths of the shadow patterns cast by X-ray sources within the field of view (FOV) and thereby to infer the directions to and intensities of the sources. Each PSPC contains eight resistive carbon-coated quartz fiber anodes, each end of which is connected to a dedicated electronic measurement chain. An X-ray event detected in the volume surrounding one of these anodes yields a pair of pulse heights, which are used to compute the event energy and position (i.e., the coordinate along the one-dimensional coded mask) via the charge-division technique. The achieved position resolution is 0.2–0.5 mm, depending on photon energy. Each PSPC also contains

Table 4.1 Instrument characteristics of *PCA* and *HEXTE*.

Property	**Description *(PCA)***	**Description *(HEXTE)***
Energy range	2–60 keV	15–250 keV
Energy resolution	$< 18\%$ at 6 keV	15% at 60 keV
Time resolution	1 microsec	8 microsecond
Spatial resolution	collimator with 1° FWHM	1° FWHM
Detectors	5 proportional counters	2 clusters of 4 NaI/CsI scintillation counters
Collecting area	6500 cm^2	2×800 cm^2
3σ sensitivity for an observing time of 10^5 s	0.1 mCrab	1 mCrab
Background	2 mCrab	0.2 Crab per HEXTE cluster

Table 4.2 *ASM* instrument parameters.

Property	**Description**
Energy range	2–12 keV
Time resolution	80% of the sky every 90 min
Spatial resolution	$3' \times 15'$
Number of shadow cameras	3, each with 6 x 90 degrees FOV
Collecting area	90 cm^2
Detector	Xenon proportional counter, position-sensitive
Sensitivity (for one 90 s “dwell”)	30 mCrab

12 metal anodes that are used to veto events caused by charged particles. Event data are normally compressed within the two *ASM* Event Analyzers (EAs) in the EDS and relayed to the spacecraft for insertion in the telemetry stream. The analysis proceeds by computing intensities for sources listed as active in a master catalog and then by searching for and locating additional sources. *ASM* results are being used to alert observers to the appearance of transients and to other time-variable phenomena and to record long-term intensity histories of bright X-ray sources. Basic instrument characteristics of *ASM* are summarized in Table 4.2

4.2 Refining system orbital ephemeris

Using the *RXTE* data we refined the orbital ephemeris of Her X-1 by exploring X-ray pulse profiles of the source. It was found that the ephemeris provided by Deeter et al. (1991) do not fit well the *RXTE* observations (1996–2005). Using the historical data *(Hakucho, Tenma, Ginga)* and the *RXTE* observations we found a new orbital solution that provides a good fit to all the data. We confirm the secular decrease in the orbital period of Her X-1 (initially found by Deeter et al.

1991) over the time period of ∼30 years and update the value of $\dot{P}_{\rm orb}$. In Section 4.2.1 we describe our method. Then, in Section 4.2.2 we apply it to the *RXTE* data. In Section 4.2.3 we analyze all historical timing data of Her X-1 and derive the new orbital ephemeris.

4.2.1 Phase-connection method

The accuracy of commonly used period search technics, such as e.g. Fourier transform or epoch folding (Leahy et al. 1983), is usually not enough to study pulse period variations due to orbital motion in the binary or intrinsic spin-up/spin-down of the neutron star. It is possible, however, to significantly increase precision of the pulse period determination by comparing X-ray pulse profiles obtained at different times. The idea of the method is to identify details of different pulse profiles and to assume that these details correspond to the same rotation phase of the neutron star. By counting pulse cycles from one observation to the next one can follow the pulse period development with an accuracy which is orders of magnitudes higher than that provided by e.g. epoch folding. The only necessary conditions are: (1) the shape of the pulse profile has to be stable enough for the common details of different pulse profiles to be identifiable and (2) the time separations of the profiles should be small enough to make it possible to maintain the counting of pulse cycles through the entire period of observations. Below we describe our method step-by-step.

As a first step the photon arrival times must be translated to the solar system barycenter in order to exclude the influence of the Earth's orbital motion. Then the data must be divided into groups with the number of cycles sufficiently large for the pulse profiles to reach sufficient statistical quality for each group. To construct the pulse profiles one can fold the data with some rough pulse period found e.g. by epoch folding (if the length of the group is small the uncertainty of the folding period affects the shape of the profile only little). Depending on the folding period, the zero epoch, and the behavior of the actual pulse period the profiles will appear to be shifted in phase with respect to each other. By measuring the value of the shift (e.g. by template matching or using a well determined feature of the profile) one can determine the actual pulse period. If the period is changing with time, one can use a numerical model to predict the amount of the shift for each pulse profile. Minimizing the difference between the observed and predicted shifts one can determine the parameters of the model and hence the time evolution of the spin period. We applied this method to the *RXTE* data of Her X-1.

4.2.2 *RXTE* data

Her X-1 was repeatedly observed by *RXTE* in the period 1996–2005 (see e.g. Gruber et al. 2001; Staubert et al. 2007b). The archive of the observations is accumulated and maintained at IAAT (Tübingen). For our analysis we used the data obtained with the *PCA* which allow to construct high-quality pulse profiles in the energy range below ∼20 keV. We have chosen the data from main-on states of 35 d cycles No. 257, 303, 313, and 323 (according to the cycle counting provided in Appendix A) which are most densely covered by the observations (see Section. 3.2.1 for details of cycle numbering). All the data have been divided into groups containing between one and three *RXTE* orbits depending on statistics. For each group we constructed the 1.24 s pulse profile by folding the data with a roughly estimated period. A typical profile is shown in Figure 4.2. The obtained pulse profiles exhibit systematic phase offsets due to the time delay caused by the orbital motion of the pulsar. These offsets were studied by measuring absolute arrival times of the

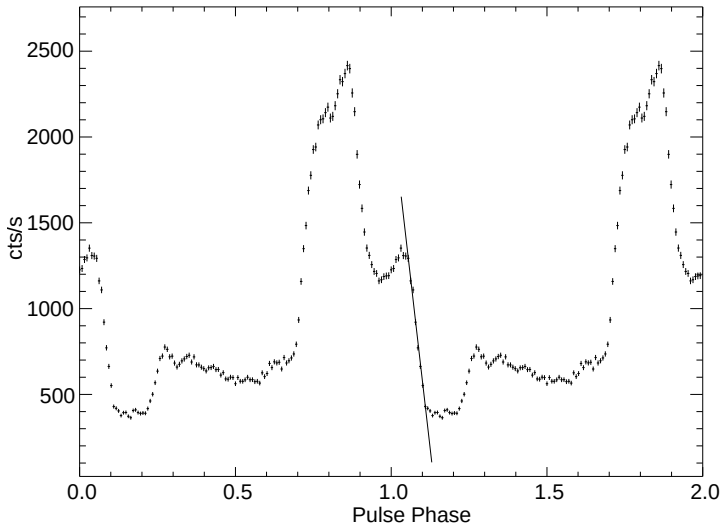

Figure 4.2 An example of *PCA RXTE* pulse profiles used to study pulse shifts due to the orbital motion of Her X-1. The solid line shows the sharp decay after the soft trailing shoulder which was used as a phase reference (see text).

sharp decay after the soft trailing shoulder of the main pulse (shown by the solid line in Figure 4.2). This stable sharp feature provides a good phase reference which can be measured with fairly high precision in each pulse profile. From now on we will call the observed time of this feature the *pulse arrival time*. In case of a circular orbit with the radius a measured in light seconds, inclination i, orbital frequency $\omega_{\rm orb} = 2\pi/P_{\rm orb}$, and an epoch of mean upper conjunction $T_{\frac{\pi}{2}}$ (the time when the mean orbital longitude of the neutron star is 90°) successive pulse arrival times can be predicted using the following simple analytic formula:

$$t^n = t^n_{\rm int} + a \sin i \cos[\omega_{\rm orb}(t - T_{\frac{\pi}{2}})], \tag{4.1}$$

where $t^n_{\rm int}$ is the intrinsic time of the reference feature in n-th 1.24 s cycle not affected by the orbital motion. In case of a constant spin period of the neutron star

$$t^n_{\rm int} = t^0_{\rm int} + nP_{\rm spin}, \tag{4.2}$$

where $t^0_{\rm int}$ is the intrinsic time of the feature corresponding to some reference cycle. In some observations (namely, in 35 d cycle No. 324) the data indicate the presence of a non-zero spin-up. In this case the intrinsic times of the phase reference are given by the formula:

$$t^n_{\rm int} = t^0_{\rm int} + nP_{\rm spin} + \frac{1}{2}n^2 \cdot P_{\rm spin}\dot{P}_{\rm spin}. \tag{4.3}$$

For all constructed pulse profiles we performed a fit of the pulse arrival times with the cosine model 4.1. If we fix the orbital parameters $T_{\frac{\pi}{2}}$, $\omega_{\rm orb}$, and $a \sin i$ to the values calculated from the ephemeris of Deeter et al. (1991) the residuals of the fit show systematic deviations correlated with the orbital phase. This means that the orbital correction is not satisfactory. The ephemeris, therefore, need to be updated. This can be done if we use $T_{\frac{\pi}{2}}$, $\omega_{\rm orb}$, and $a \sin i$ as fit parameters. By doing so we obtained the new set of orbital parameters for which the fit residuals of the pulse arrival times are flat. Figure 4.3 shows the result of our analysis for the 35 d cycle No. 314. The top panel shows the relative shift of the pulse arrival times ("pulse shift") caused by the orbital motion

Table 4.3 Orbital parameters of Her X-1 determined from *RXTE* observations during 35 d cycles No. 257, 304, 314, and 324. The uncertainties in parentheses (68%) refer to the last digit(s).

35 d cycle	257	314	304	324
$P_{\rm spin}$	1.23773946(2)	1.23776700(1)	1.23777022(2)	1.23776166(1)
$T_{\frac{\pi}{2}}$	50290.659200(18)	52242.451319(16)	51893.917025(44)	52599.486465(17)
$P_{\rm orb}$	1.700167387	1.700167289	1.700167307	1.700167272
$a \sin i$	13.1847(12)	13.1824(10)	not constrained	13.1825(10)

of the source fitted by our model. The middle panel shows the residuals of the fit using the orbital parameters of Deeter et al. (1991). The systematic deviations correlated with orbital phase are clearly seen. The bottom panel shows the residuals in case of using our best-fit orbital parameters. The results for 35 d cycles No. 257, 304, and 324 look similar.

The found orbital parameters for each of the four 35 d cycles are listed in Table 4.3. The orbital period $P_{\rm orb}$ cannot be constrained using individual observations. For each cycle we fixed it to the values calculated from the global solution ($P_{\rm orb}$ and $\dot{P}_{\rm orb}$) provided by Deeter et al. (1991). The fits are not very sensitive to slight changes in $P_{\rm orb}$ since the data cover only a couple of orbital revolutions in each cycle. $a \sin i$ found from the *RXTE* data is consistent with that provided by (Deeter et al. 1991). The values of $T_{\frac{\pi}{2}}$ are significantly different from those calculated using the global solution of Deeter et al. (1991). This discrepancy causes systematic deviations in the residuals shown in the middle panel of Figure 4.3. The reason of these deviations is the fact that the global solution for the orbital period provided by (Deeter et al. 1991) is not accurate enough to be valid over the time period of 30 years including the historical observations of Her X-1 and the new *RXTE* observation. The main source of uncertainty is the value of $\dot{P}_{\rm orb}$ which needs to be updated. In the next Section we will find the new global solution for the orbital period ($P_{\rm orb}$ and $\dot{P}_{\rm orb}$) using all available observations of the source.

4.2.3 Orbital ephemeris

Using our new values of $T_{\frac{\pi}{2}}$ and the historical data from previous missions (Deeter et al. 1981, 1991; Wilson et al. 1994) it is possible to find an improved value for the time derivative of the orbital period $\dot{P}_{\rm orb}$ and, therefore, to construct the new orbital ephemeris of Her X-1 valid for the whole 30 year period of observations of the source. Modeling of all $T_{\frac{\pi}{2}}$ values (historical observations plus *RXTE* data) by a linear ephemeris ($\dot{P}_{\rm orb} \equiv 0$) results in very poor fit: $\chi^2_{\rm red} = 48.2$ for 26 d.o.f. Thus, the linear ephemeris can clearly be rejected. Figure 4.4 shows the residuals of $T_{\frac{\pi}{2}}$ after subtracting the linear part of the quadratic best-fit ephemeris. For the quadratic ephemeris ($\dot{P}_{\rm orb} \neq 0$, shown by the solid curve in Figure 4.4) the fit gives $\chi_{\rm red} = 2.3$ for 25 d.o.f. The best fit parameters for the quadratic ephemeris are listed in Table 4.4. $P^{\rm ref}_{\rm orb}$ is the orbital period at the reference time $T^{\rm ref}_{\frac{\pi}{2}}$. For any particular observations $T_{\frac{\pi}{2}}$ and $P_{\rm orb}$ can be found using the following formulae:

$$P_{\rm orb}(t) = P^{\rm ref}_{\rm orb} + \dot{P}_{\rm orb}(t - T^{\rm ref}_{\frac{\pi}{2}}), \tag{4.4}$$

$$T_{\frac{\pi}{2}}(n) = T^{\rm ref}_{\frac{\pi}{2}} + nP^{\rm ref}_{\rm orb} + \frac{1}{2}n^2 P_{\rm orb}\dot{P}_{\rm orb}; \tag{4.5}$$

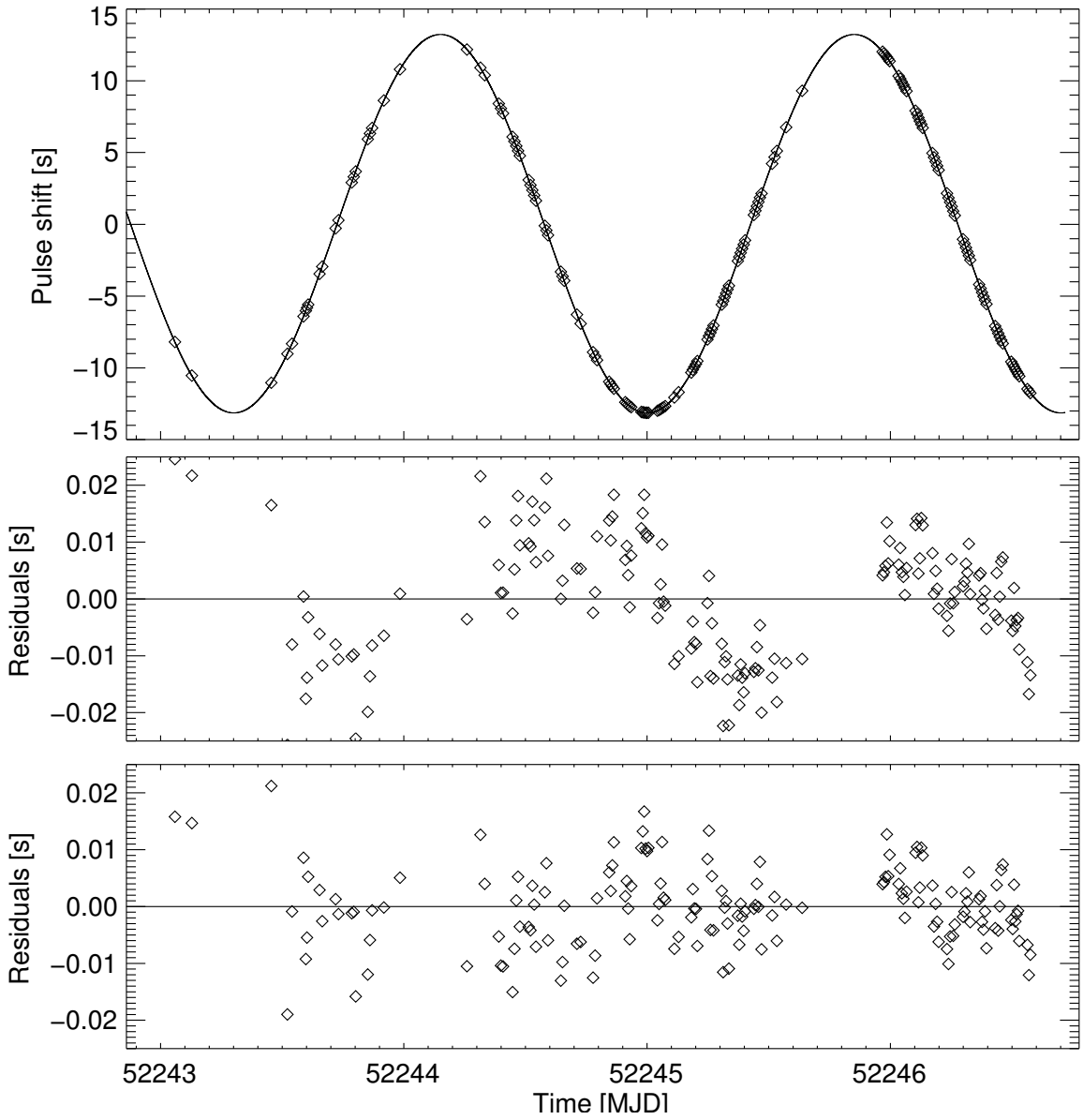

Figure 4.3 Delays of the pulse arrival time in Her X-1 due to its orbital motion fitted by the cosine formula 4.1 for the 35 d cycle No. 314 *(top panel)*, the residuals of the fit using the orbital parameters from Deeter et al. (1991) *(middle panel)* and using our best-fit parameters *(bottom panel)*.

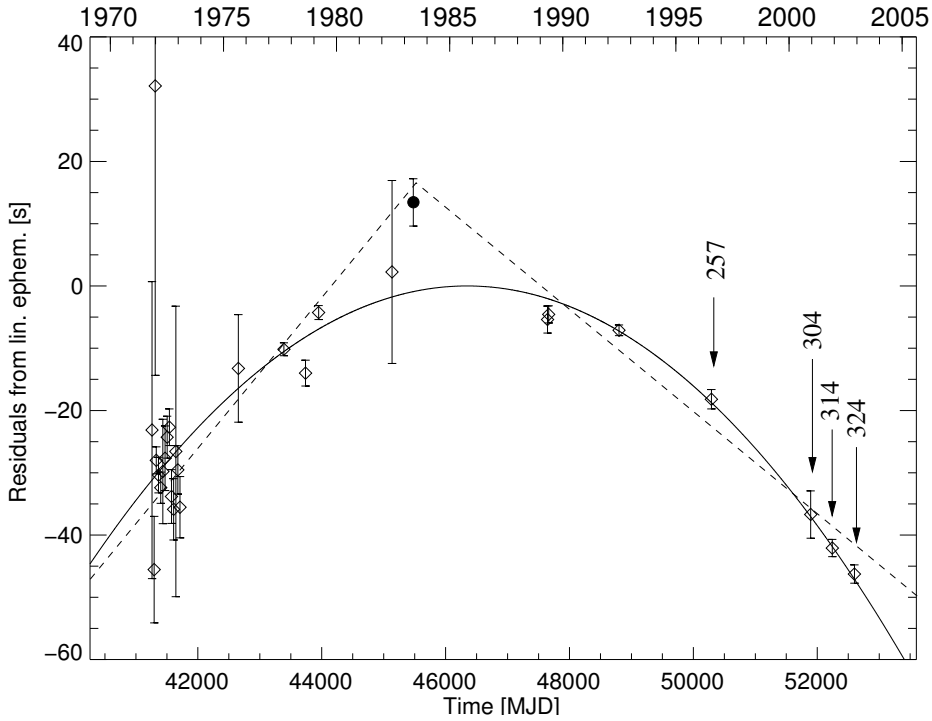

Figure 4.4 Residuals of $T_{\frac{\pi}{2}}$ after subtracting the linear part of the quadratic best-fit ephemeris. For *RXTE* observations analyzed in this work 35 d cycle numbers are indicated. The dashed line shows a fit by the linear ephemeris with a sudden jump of the orbital period around 1983. The filled circle corresponds to the questionable value obtained with the *Tenma* satellite.

where n is the orbital cycle number ($n = 0$ corresponds to $T^{\rm ref}_{\frac{\pi}{2}}$).

Following the suggestion of Deeter et al. (1991) of a constant orbital period with a sudden change in 1983 (MJD ~45000), we performed a separate fit of the data before and after 1983 with a linear ephemeris (the dashed lines in Figure 4.4). The fit gives $\chi_{\rm red} = 4.0$ for 26 d.o.f. which is about two times larger than for the quadratic ephemeris. We can, therefore, reject the sudden change of the orbital period in 1983.

The filled circle in Figure 4.4 corresponds to the data obtained by the *Tenma* satellite. The linear solution with the jump of $P_{\rm orb}$ around 1983 is mainly driven by this data point which deviates from the quadratic fit by more than 3σ. Removing the *Tenma* point from the analysis improves the fit of the quadratic ephemeris, giving $\chi_{\rm red} = 1.8$ for 24 d.o.f. The linear fit with the sudden jump in $P_{\rm orb}$ gives $\chi_{\rm red} = 4.2$ for 25 d.o.f. Thus, without the *Tenma* point the data strongly favour the solution with a gradual decrease of the orbital period corresponding to the quadratic ephemeris.

4.3 Measuring parameters of individual 35 d cycles

The All Sky Monitor aboard *(ASM) RXTE* provides almost uninterrupted monitoring of X-ray fluxes for several hundred bright X-ray sources. The archive contains X-ray flux measure-

Table 4.4 Quadratic ephemeris of Her X-1 determined from a common fit of the historical observations and *RXTE* data. The uncertainties in parentheses (68%) refer to the last digit(s).

$T_{\frac{\pi}{2}}^{\rm ref}$ [MJD(TDB)]	46359.871938(6)
$P_{\rm orb}^{\rm ref}$ [days]	1.700167591(2)
$\dot{P}_{\rm orb}$ [d/d]	$-4.74(9)\times10^{-11}$

ments in the 2–12 keV band, averaged over ∼90 s. The monitoring began in February 1996 and continues up to date. The *ASM* data of Her X-1 analyzed in this work contain some 70000 individual flux measurements and cover more than hundred 35 d cycles. We use these data to analyze the long-term behavior of the Her X-1 X-ray light curve[1]. The accuracy of the light curve is limited: the *ASM* count rate for Her X-1 is $\lesssim 10$ count s^{-1} (the maximum *Uhuru* count rate from Her X-1 was about 100 count s^{-1}). Nevertheless, for cycles with no gaps in the data, one may e.g. clearly distinguish around which orbital phase, 0.25 or 0.75, each cycle turned on.

By analyzing the *ASM* data we would like first to measure the characteristics of individual cycles, such as the time of turn-on and the maximum flux of the main-on (we use the latter as a measure of the intrinsic X-ray luminosity of the source, see below) and second, to construct averaged X-ray light curves by superposition of many 35 d cycles (this allows to explore the common details of the light curve which are not seen in individual 35 d cycles due to low statistics). In this Section we study the parameters of individual 35 d cycles. The averaged X-ray light curves are analyzed in Section 4.4.

4.3.1 Preliminary processing

Before measuring characteristics of individual 35 d cycles we performed preliminary processing of the *ASM* light curve. The goal of this processing is the reduction of the dispersion of the flux through rebinning and removal of X-ray dips and eclipses, resulting in a smoothed light curve. First, we removed all data points falling into X-ray eclipses assuming the eclipse duration of 5.5 h (Giacconi et al. 1973). Then, we combined consecutive data points into groups such that the time spread of the points inside each group did not exceed 0.05 days. The group has been centered to the mean time of the points inside it. The observed count rates, C_k, were averaged inside each group with a weight inversely proportional to the variance σ_k^2:

$$\overline{C} = \frac{\sum\limits_{k=1}^{n} C_k/\sigma_k^2}{\sum\limits_{k=1}^{n} 1/\sigma_k^2}, \tag{4.6}$$

where n is the total number of individual points in each group. The variance of the averaged count rate $\overline{C}$ was determined by the formula:

[1]We use results provided by the ASM RXTE teams at MIT and at the RXTE SOF and GOF at NASA's GSFC. http://xte.mit.edu/ASM_lc.html

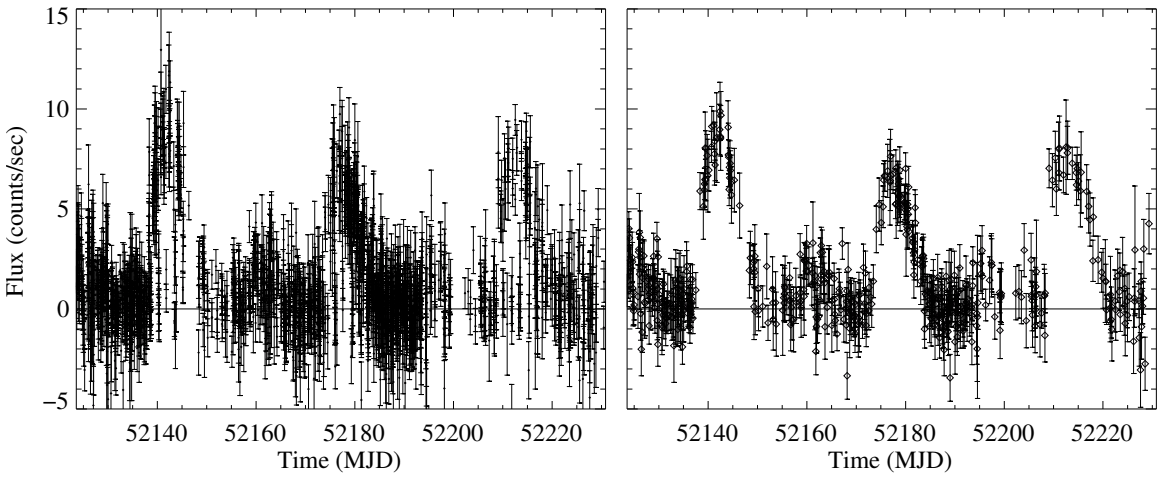

Figure 4.5 *Left:* Her X-1 *ASM* light curve sample. *Right:* the same light curve after preliminary processing (see text).

$$\sigma^2 = \frac{1}{n^2}\sum_{k=1}^{n}\sigma_k^2 + \frac{1}{n-1}\frac{\sum\limits_{k=1}^{n}(\overline{C}-C_k)^2/\sigma_k^2}{\sum\limits_{k=1}^{n}1/\sigma_k^2}. \tag{4.7}$$

Then we removed data points falling into X-ray dips. We used the ephemeris of dips provided by Shakura et al. (1998a). As a result we obtained a smooth light curve which contains only flux variations related to the alternation of on- and off-states. The left panel of Figure 4.5 shows an example of the original *ASM* light curve. The right panel represents the same light curve after processing.

4.3.2 Turn-on times and $(O-C)$ diagram

The *ASM* light curve processed by the method described above was then used to determine the turn-on time of each 35 d cycle. This was done in the following way. First, we divided all cycles into two groups: (1) the cycles where the main-on state contains a gap (or gaps) longer than one day (we call them "bad" cycles) and (2) the cycles without such gaps in the main-on ("good" cycles). The main-on of each "good" cycle was fitted with an analytical function of the following form:

$$f(t) = A_0\frac{1}{1+\exp[(t-A_1)/A_2]}\left(1-\exp\frac{t-A_3}{A_4}\right), \tag{4.8}$$

where t is the time, $A_0,..,A_4$ are the fitting parameters. This function consists of two smoothed "steps", the first representing the beginning of a main-on state, the second representing the end of the main-on. Figure 4.6 shows an example fit of a main-on state observed by *ASM* with the above analytical function. For the "good" cycles the turn-on was assumed to happen at the time where the fitted analytical curve rises to 30% of its maximum value. The error range of the turn-on time was determined by the closest data point with the signal-to-noise ratio $\overline{C}/\sigma \leq 3$ on the left side

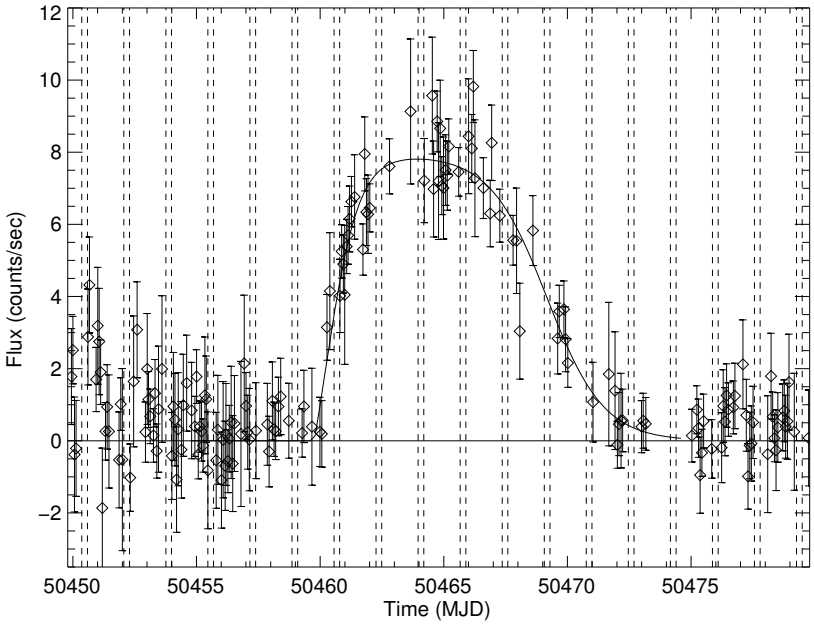

Figure 4.6 An example of the processed Her X-1 *ASM* light curve fitted by the analytical function 4.8. Vertical dashed lines show intervals of X-ray eclipses.

and the closest data point with $\overline{C}/\sigma > 3$ on the right side ($\overline{C}$ and σ are determined by Eqs. 4.6 and 4.7). For the "bad" cycles turn-on moments were determined in a different way. The analytical curves obtained from fitting "good" cycles were used as a template library, assuming that each "bad" cycle can be well described by one of these analytical curves. For a given "bad" cycle we find a corresponding curve from our library that fits it best in terms of χ^2, and we determine the turn-on time from this curve. The errors of the turn-on times were calculated in the same way as for the "good" cycles.

The resulting list of determined turn-on times can be found in Appendix A The corresponding $(O-C)$ diagram is shown in Figure 4.7. Horizontal lines on the diagram would correspond to the 35 d period of $20.5 \times P_{\rm orb}$. The zero-point is arbitrarily chosen to be at MJD=41501.149 (the turn-on moment of the cycle No. 5, see Section 3.2.1). Two anomalous low states that took place since the beginning of the *ASM* monitoring are indicated by shaded areas.

4.3.3 Maximum main-on flux

One of the most important parameters of the system is the X-ray luminosity $L_{\rm X}$ which reflects the mass accretion rate onto the neutron star $\dot{M}$:

$$L_{\rm X} \sim \eta \dot{M} c^2, \tag{4.9}$$

where η is the radiative efficiency of accretion usually assumed to be of the order of 10%. Due to high orbit inclination the view to the X-ray source in Her X-1 is blocked (or partially blocked) by the accretion disk during a substantial part of the 35 d period. The X-ray flux measured at a particular time, therefore, is subject to modulation by variable absorption/shading by the accretion disk and cannot be directly used to deduce $L_{\rm X}$. In our model we assume that the source is not screened by the accretion disk near the maximum of the main-on state (Fig. 3.6). Thus, we used the main-on state maximum flux as a measure of $L_{\rm X}$.

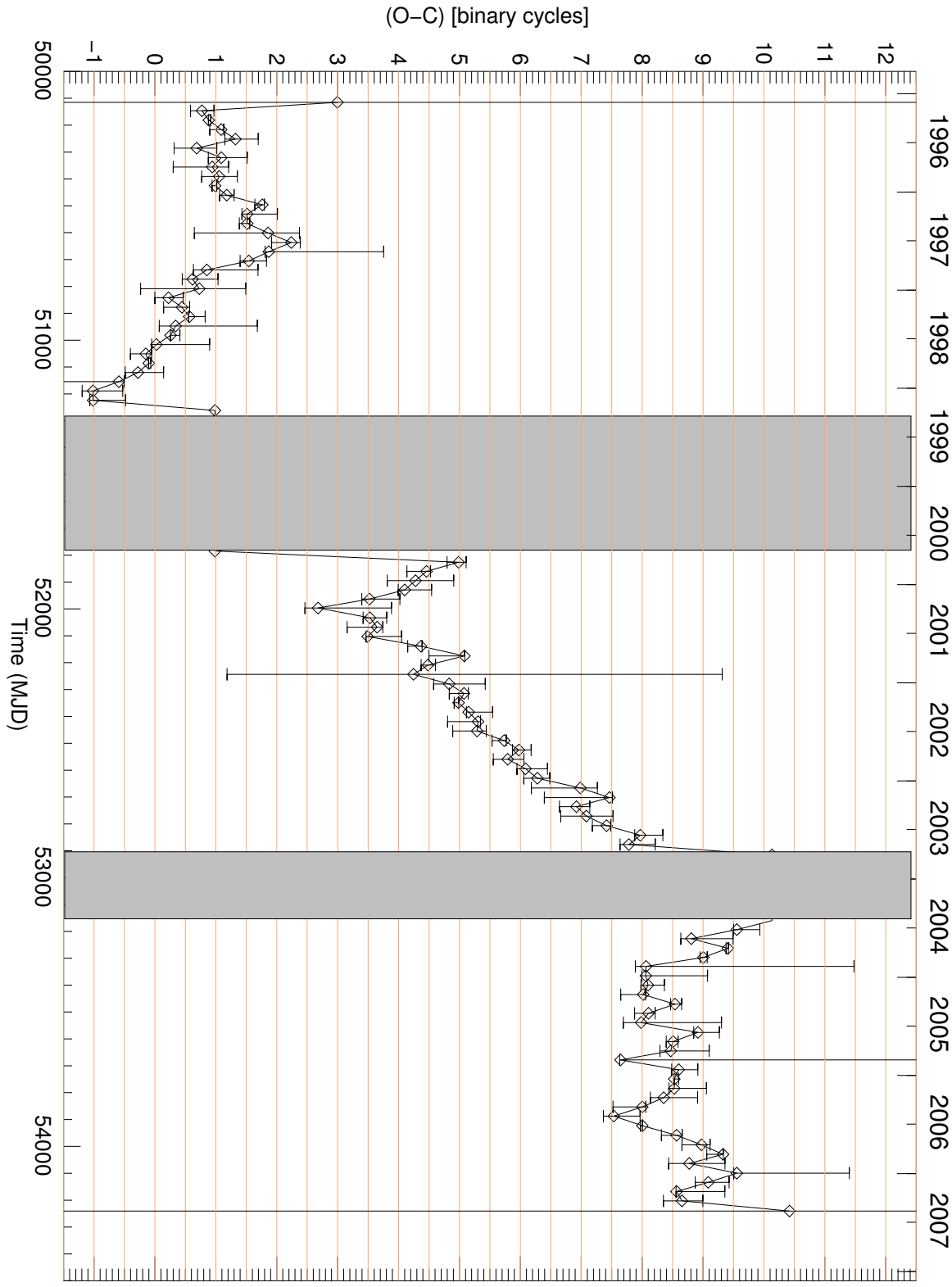

Figure 4.7 The $(O-C)$ diagram corresponding to the turn-on moments determined from the *ASM RXTE* data. Horizontal line would correspond to the 35 d period of $20.5 \times P_{\mathrm{orb}}$. Shaded areas mark anomalous low states.

We used two ways of measuring the maximum main-on flux: (1) from the analytical function described in Section 4.3.2 (simply taking its maximum), and (2) calculating the average *ASM* flux from the data points close to the maximum of the main-on state. The results obtained with both methods are consistent with each other and shown in Figure 4.8. To be specific we will use the second method in the following. The resulting list of determined main-on fluxes can be found in Appendix A

4.3.4 Correlations between $(O-C)$, maximum main-on flux, and the pulse period

In this Section we explore correlations between $(O-C)$, $L_{\rm X}$ (measured through the maximum main-on flux), and 1.24 s pulse period. The methods of determining turn-on times and maximum main-on fluxes on the basis of *ASM RXTE* data are described in previous Sections. Historical data of the pulse period (before *RXTE* and *BATSE* era) are taken from a compilation of Kunz (1996) which is mainly based on the collection by Nagase (1989) and Sunyaev et al. (1988). Additional data are from *MIR-HEXE* (Kunz 1996) and several highly accurate values from pointed observations by *RXTE*. *BATSE* data were added as follows: the publicly available pulse search data were taken and "screened", that is extreme values ($\geq 4\sigma$ different from the mean) were removed and for each on-state an averaged pulse period and a weighted uncertainty were calculated. The historical turn-on times are also taken from a compilation of Kunz (1996), which is largely based on papers by Staubert et al. (1983) and Ögelman et al. (1985). For determination of the turn-on times from the *BATSE* data publicly available occultation data of Her X-1 were used [2].

A comparison of the spin period development with $(O-C)$ immediately shows that the large features in the development of the two values are highly (anti-)correlated (see top and middle panels of Figure 4.9). The anticorrelation becomes clearer if one subtracts a linear spin-up trend $dP_{\rm spin}/dt = -1.1\times10^{-13}$ s/s (shown by the dotted line on the top panel) from the pulse period. The residuals after the subtraction are shown in the bottom panel. The following global features appear simultaneously: (1) maxima in pulse period residuals, corresponding to (relative) spin-down, (2) minima in $(O-C)$ (going into the minimum means a short turn-on period, see Section 3.2.1), (3) the appearance of Anomalous Low States (ALSs, shaded areas) around these extrema.

We should note that the next to last ALS (MJD 51300–51800) was so long that one cannot unambiguously extend the 35 d cycle counting from the beginning to the end of the state. In other words, we cannot say for sure how many cycles took place during the ALS. Two solutions are possible: (1) the first turn-on after the ALS is the beginning the 17-th cycle since the start of the state, which corresponds to the averaged over the ALS 35 d period of $20.9\times P_{\rm orb}$; (2) the first turn-on after the ALS is the beginning of the 18-th cycle and the average period during the ALS is $19.7\times P_{\rm orb}$. The first solution is used in Figures 4.7 and 4.9 since it is closer to the averaged duration of the 35 d cycle over the whole data set $\sim 20.5\times P_{\rm orb}$. However, the second solution is more consistent with the observed anti-correlation between $(O-C)$ and $P_{\rm spin}$: the huge spin-down occurred during the ALS would correspond the large decrease in $(O-C)$. Another argument in support of the second solution is the general observation that the 35 d period is always shorter ($\sim 20\times P_{\rm orb}$) when approaching an ALS (see e.g. Fig 4.9). Coming out of the ALS in 2000, it is still short for several cycles before it changes to a higher value (increasing $(O-C)$). So, the 35 d period is likely to remain low (or decrease further) inside the ALS. The $(O-C)$ diagram corresponding to

[2]The data are provided by the *BATSE* Instrument Team at the Marshall Space Flight Center

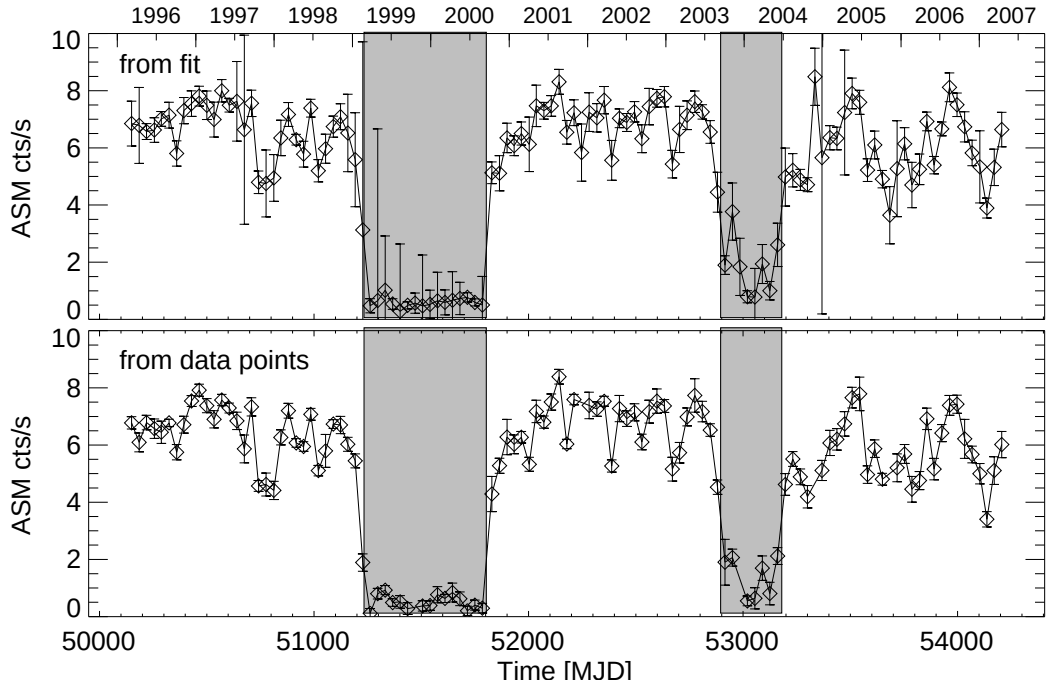

Figure 4.8 The maximum main-on flux of Her X-1 measured by fitting each main-on state with an analytical curve defined by Eq. 4.8 (*top*), and by averaging the *ASM* data points close to the maximum of main-ons (*bottom*). Shaded areas mark two ALS.

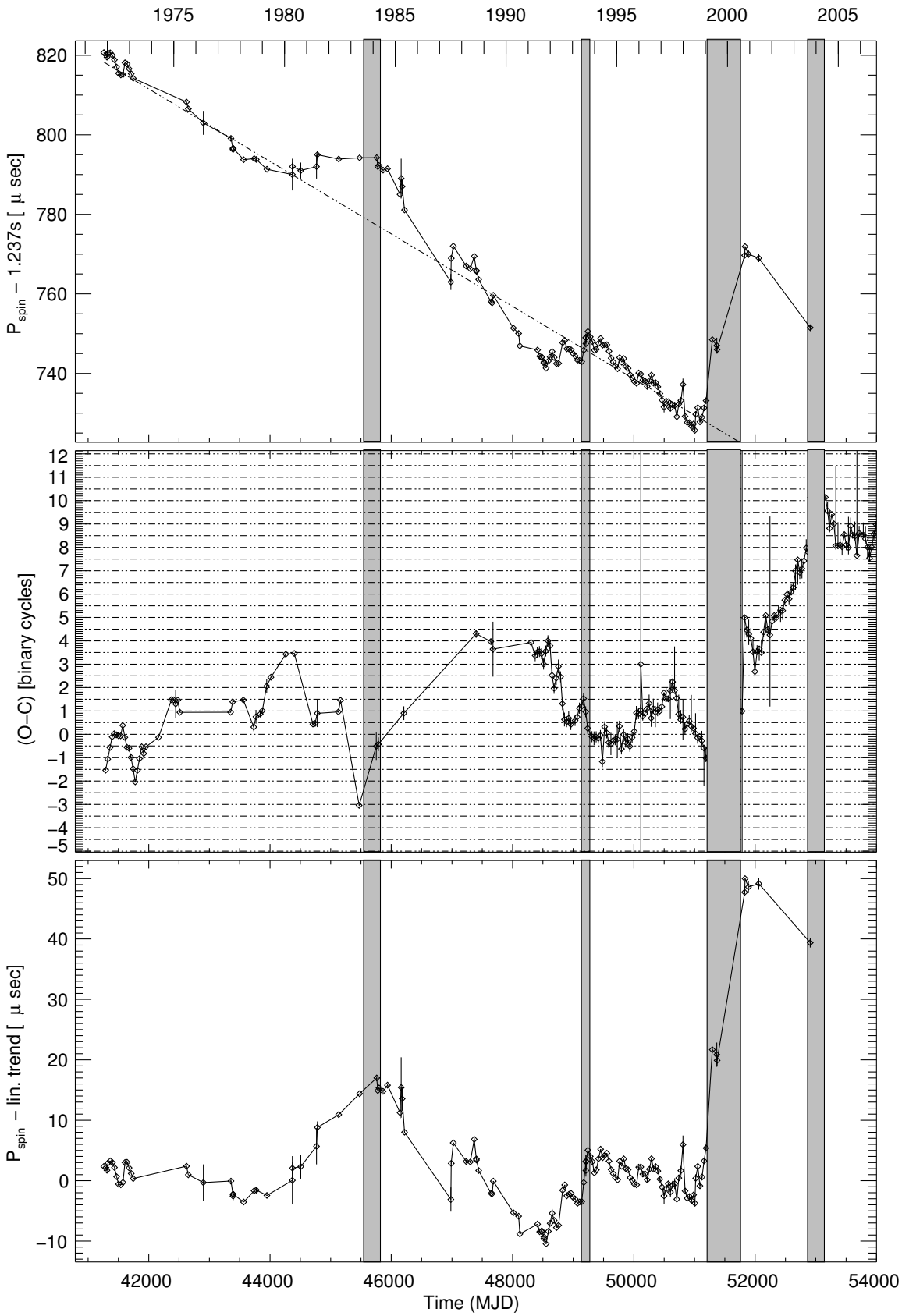

Figure 4.9 The long-term behavior of the pulse period of Her X-1 (*top*) and the ($O - C$) diagram (*middle*). The anti-correlation between the two values is clearer if one subtracts a linear spin-up trend (shown by the dotted line in the top panel) from the pulse period. The *bottom* panel shows the residuals after the subtraction. Shaded areas mark anomalous low states.

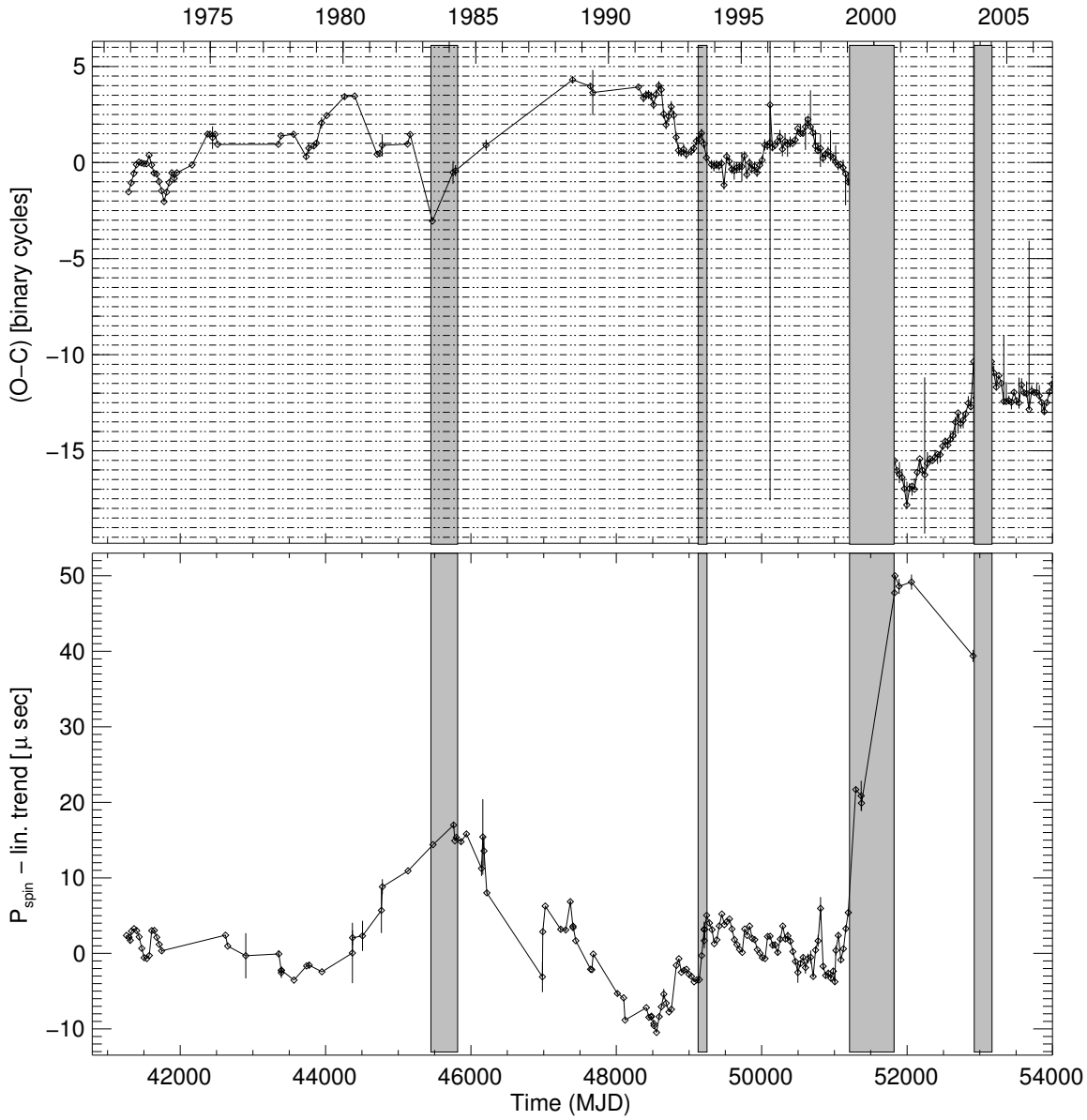

Figure 4.10 The same as in the middle and bottom panels of Figure 4.9 but assuming a different counting of 35 d cycles during the ALS at MJD 51300–51800.

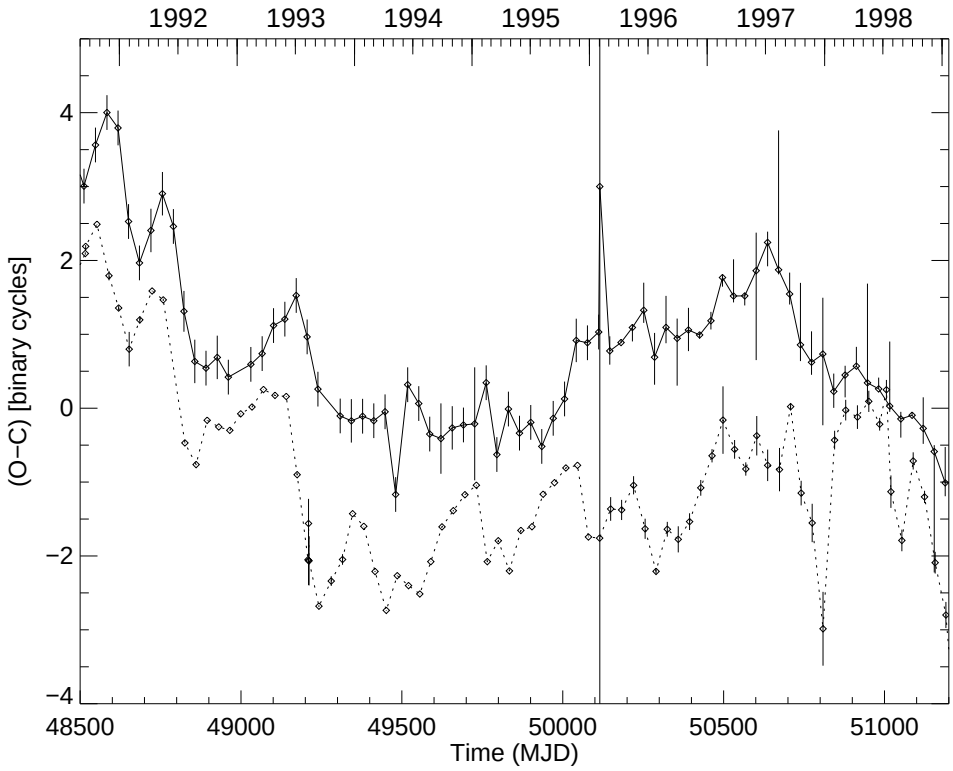

Figure 4.11 The $(O - C)$ diagram (solid curve) for the time period MJD: 48500–51200. The dotted curve represents inverted, shifted and stretched vertically pulse period residuals (after subtracting the linear spin-up trend) (Staubert et al. 2006).

the second solution is shown in the top panel of Figure 4.10.

There is also clear anti-correlation on shorter time scales (a few hundred days), as shown in Figure 4.11 (see Staubert et al. 2006, and references therein). The pulse period residuals shown by the dotted curve are inverted, shifted and stretched vertically in this plot. We note that this kind of correlation has been seen earlier by Ögelman et al. (1985) on the basis of smaller sets of data. The data in Figure 4.11 are due to the dense sampling by *BATSE CGRO*.

We have also searched for the correlation of the spin-up rate of the neutron star and the X-ray luminosity. Such a correlation for an accreting pulsar is generally expected in accretion theory (see e.g. Lipunov 1992), where an increase of the mass accretion rate $\dot{M}$ leads to an increase of the rate of change of the neutron star's angular momentum:

$$\frac{d(I\omega)}{dt} = \dot{M}\sqrt{GMR_{\rm A}} - \kappa\frac{\mu^2}{R_c^3}, \tag{4.10}$$

where I is the moment of inertia of the neutron star, ω is the angular frequency, $R_{\rm A}$ is the Alfvén radius, M is the mass of the neutron star, μ is its magnetic moment, R_c is the corotational radius, and κ is the numerical coefficient of the order of unity. $\dot{M}$ is proportional to the X-ray luminosity $L_{\rm X}$ (Eq. 4.9). Such a correlation has been observed in many other accreting pulsars (see e.g. Bildsten

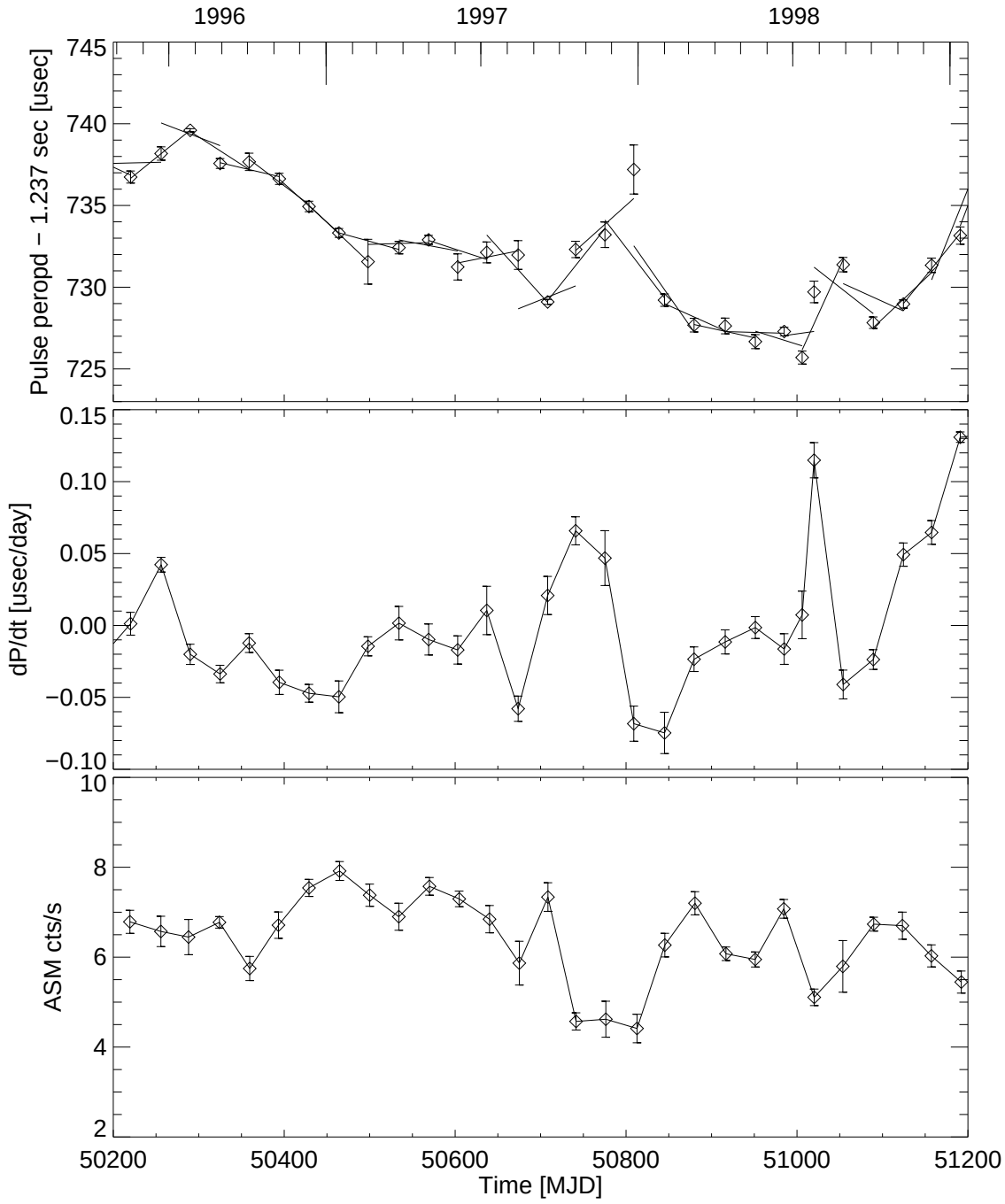

Figure 4.12 *Top:* Pulse period $P_{\rm spin}$ of Her X-1 as a function of time. Each three adjacent points are fitted by a straight line to determine $\dot{P}_{\rm spin}$ at each point. *Middle:* $\dot{P}_{\rm spin}$. *Bottom:* Maximum main-on flux.

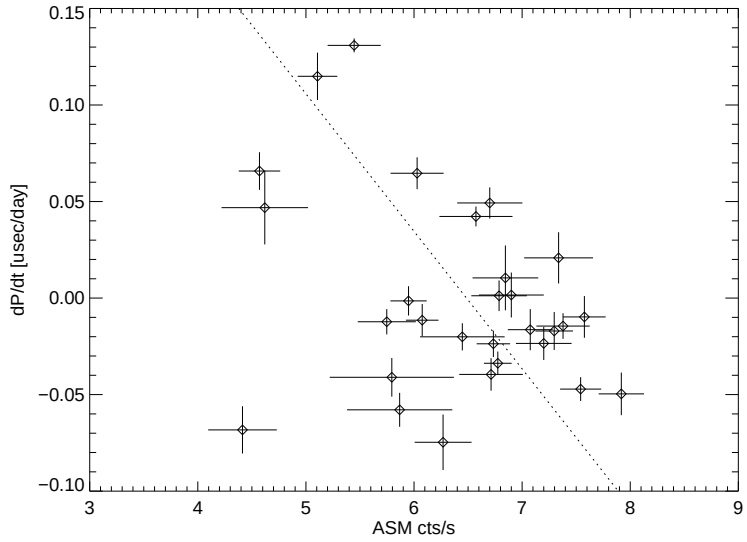

Figure 4.13 The pulse period derivative $\dot{P}_{\rm spin}$ of Her X-1 versus the maximum flux during the corresponding 35 day main-on as observed by the *ASM RXTE*. A linear fit (taking uncertainties in both variables into account) defines a slope of $(72\pm 5)\times 10^{-9}$ s/day.

et al. 1997, for a review). In Her X-1, however, the correlation was so far questionable (see however Wilson et al. 1994). In this work we use the maximum main-on flux as a measure of $L_{\rm X}$ (see Section 4.3.3). To check the correlation we used the time interval MJD 50000–51200, where the data sets from the *BATSE CGRO* and *ASM RXTE* are overlapping. The first one provides good pulse period measurements while the second is used to derive the maximum main-on flux for each 35 d cycle. In order to reconstruct pulse period derivatives $\dot{P}_{\rm spin}$ from the pulse period data we used the following method. For each pulse period data point (except for the first and the last point) we performed a linear fit of this point with the two adjacent (left and right) data points (see the top panel of Figure 4.12). $\dot{P}_{\rm spin}$ was determined from the slope of the fits (shown in the middle panel of Figure 4.12). The bottom panel shows the maximum main-on flux during corresponding 35 d cycles. An indication of an anti-correlation between $\dot{P}_{\rm spin}$ and the flux can already be seen in Figure 4.12.

In Figure 4.13 we plot the pulse period derivative $\dot{P}_{\rm spin}$ as a function of the maximum main-on *ASM* flux. The dashed line is from a linear fit, taking uncertainties of both variables into account (see e.g. *Numerical Recipes, 15.3*), and it defines a slope of $(72\pm 5)\times 10^{-9}$ s/day. Pearsons linear correlation coefficient is -0.35 (corresponding to the probabilities to find the correlation by chance of $\sim$ 2%). We consider this correlation as rather poor. This is not surprising because, as pointed out in Section 2.4.1, the interchange of the angular momentum between the accretion disk and the neutron star can be much more complicated than described by Eq. 4.10. Also the maximum main-on flux might still be not a perfect indicator of $\dot{M}$. However, in Discussion (Section 8.1.3) we will show that the found dependence of the maximum main-on flux on $\dot{P}_{\rm spin}$ is in a *quantitative* agreement with the prediction of the accretion torque model developed by Ghosh & Lamb (1979) for parameters of Her X-1. This agreement suggests that the found correlation is real.

Table 4.5 Recent cyclotron line energy measurements in Her X-1 by *RXTE*. Uncertainties are at the 68% level.

Observation month/year	35 d cycle	Center MJD	Line Energy keV	max. Flux ASM cts/s
July 96	257	50029.75	41.12 ± 0.55	7.37 ± 0.34
Sep 97	269	50707.06	40.62 ± 0.49	7.49 ± 0.73
Dec 00	304	51897.69	40.07 ± 0.31	6.04 ± 0.47
Jan 01	305	51933.67	39.05 ± 0.55	5.72 ± 0.34
May 01	308	52035.48	39.93 ± 0.63	7.15 ± 0.50
June 01	309	52071.16	39.73 ± 0.52	6.93 ± 0.20
Dec 01	314	52245.09	40.04 ± 0.22	
Aug 02	321	52492.96	40.01 ± 0.29	7.19 ± 0.26
Nov 02	324	52599.32	40.51 ± 0.13	7.64 ± 0.30
Dec 02	325	52634.01	40.60 ± 0.41	7.55 ± 0.34
Oct 04	344	53300.95	38.51 ± 0.51	4.50 ± 0.24
July 05	352	53577.35	38.95 ± 0.52	5.12 ± 0.37

4.3.5 Correlation between the CRSF energy and the maximum main-on flux

As mentioned in Section 3.2.4 the X-ray spectrum of Her X-1, including CRSF has been measured by many instruments since its discovery. Starting from 1996 the source was repeatedly observed by the *RXTE* pointing instruments, *PCA* and *HEXTE*. This allowed a coherent analysis of the X-ray spectral data spread over the period of ten years (1996–2005). The measured centroid of the cyclotron line, $E_{\rm cycl}$, is shown in Figure 3.5 along with other historical observations (Staubert et al. 2007b). A comparison of the line centroid energy behavior with the maximum main-on flux (2–10 keV, see Section 4.3.3) from the 35 d cycles corresponding to the pointed *RXTE* observations shows that there is a significant positive correlation between the two values. If we take the locally measured fluxes (e.g. from our spectral fits) we find that they track the maximum *ASM* flux quite well and they show the same correlation with $E_{\rm cycl}$. However, we prefer the main-on state maximum flux as the better information on the accretion state of the source, since, as we mentioned above, the locally measured flux is subject to modulation by variable absorption/shading by the accretion disk.

For a quantitative analysis of this correlation we restrict ourselves to the results from *RXTE* data only (see Table 4.3.5), because they offer the advantage of maximum comparability due to a uniform analysis of data from the same instruments. In Figure 4.14 we plot the cyclotron line centroid energy $E_{\rm cycl}$ as a function of the maximum 35 d main-on state *ASM* flux. The dashed line is from a linear fit, taking uncertainties of both variables into account, and it defines a slope of $0.66 \pm 0.10\,(68\%)$ keV/(ASM cts/s). Pearsons linear correlation coefficient is 0.90, the Spearman Rank correlation coefficient is 0.85 (corresponding to the probabilities to find these correlations by chance of $\leq 6\times10^{-5}$ and $\leq 4\times10^{-4}$, respectively. We consider this correlation as highly significant. Its physical implications are discussed in Section 8.1.4.

We also point out here, that the apparent decrease of $E_{\rm cycl}$ (and the correlated *ASM* count rate) with time after 1991, seen in Figure 3.5, is an artifact due to the general variability of the source

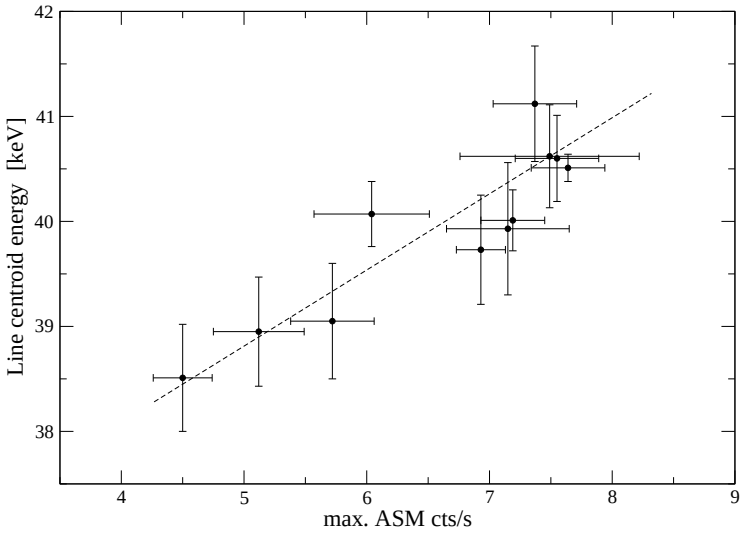

Figure 4.14 The centroid cyclotron line energy of Her X-1 versus the maximum flux during the corresponding 35 day main-on as observed by the *ASM RXTE*. A linear fit (taking uncertainties in both variables into account) defines a slope of 0.66 ± 0.10 keV/(ASM cts/s) (Staubert et al. 2007b).

and the random way by which the data happened to be taken, and not a secular decrease. Despite strong short-term variability the *ASM* light curve of Her X-1 does not provide any indication for a long-term (≥ 5 yrs) change of the mean X-ray luminosity.

4.4 Averaged *ASM* light curves

Using the *ASM RXTE* (with ~5 cts/s from Her X-1 in the main-on) details cannot be explored in individual 35 d cycles. However, through superposition of many 35 d light curves common details (e.g. X-ray dips, post-eclipse recoveries) become recognizable. This approach has been used by Shakura et al. (1998a); Scott & Leahy (1999); Still & Boyd (2004). The *ASM* archive, however, has grown considerably, allowing to construct averaged light curves with smaller dispersion than in previous works.

To construct the averaged light curves we used the original *ASM* data (without processing described in Section 4.3.1). As mentioned above, in most cases turn-ons occur near orbital phases 0.2 and 0.7. Thus all 35 d cycles have been divided into two groups – with the turn-on near $\phi_{\rm orb} = 0.2$ and near $\phi_{\rm orb} = 0.7$. Inside each group the light curves were superposed and averaged, after shifting them in such a way that the eclipses coincided. The superposed light curves are shown in Figure4.15.

In the averaged light curve corresponding to the turn-on near $\phi_{\rm orb} = 0.7$ (upper panel) one can see that the flux starts to increase already near $\phi_{\rm orb} = 0.2$ and then is is suppressed by a strong anomalous dip around $\phi_{\rm orb} = 0.5$. This is due to the fact that some cycles classified to turn-on near $\phi_{\rm orb} = 0.7$ actually turned on near $\phi_{\rm orb} = 0.2$, but this cannot be recognized in the individual light curve due to low statistics. This shows some limitations of determining the turn-on times from *ASM* data.

4.4.1 Evidence for a change in the disk tilt during the 35 d cycle

In the short-on state complicated dip patterns can be observed. Anomalous dips near $\phi_{\rm orb} = 0.5$ are present on two (or even three) successive orbits after the beginning of the short-on

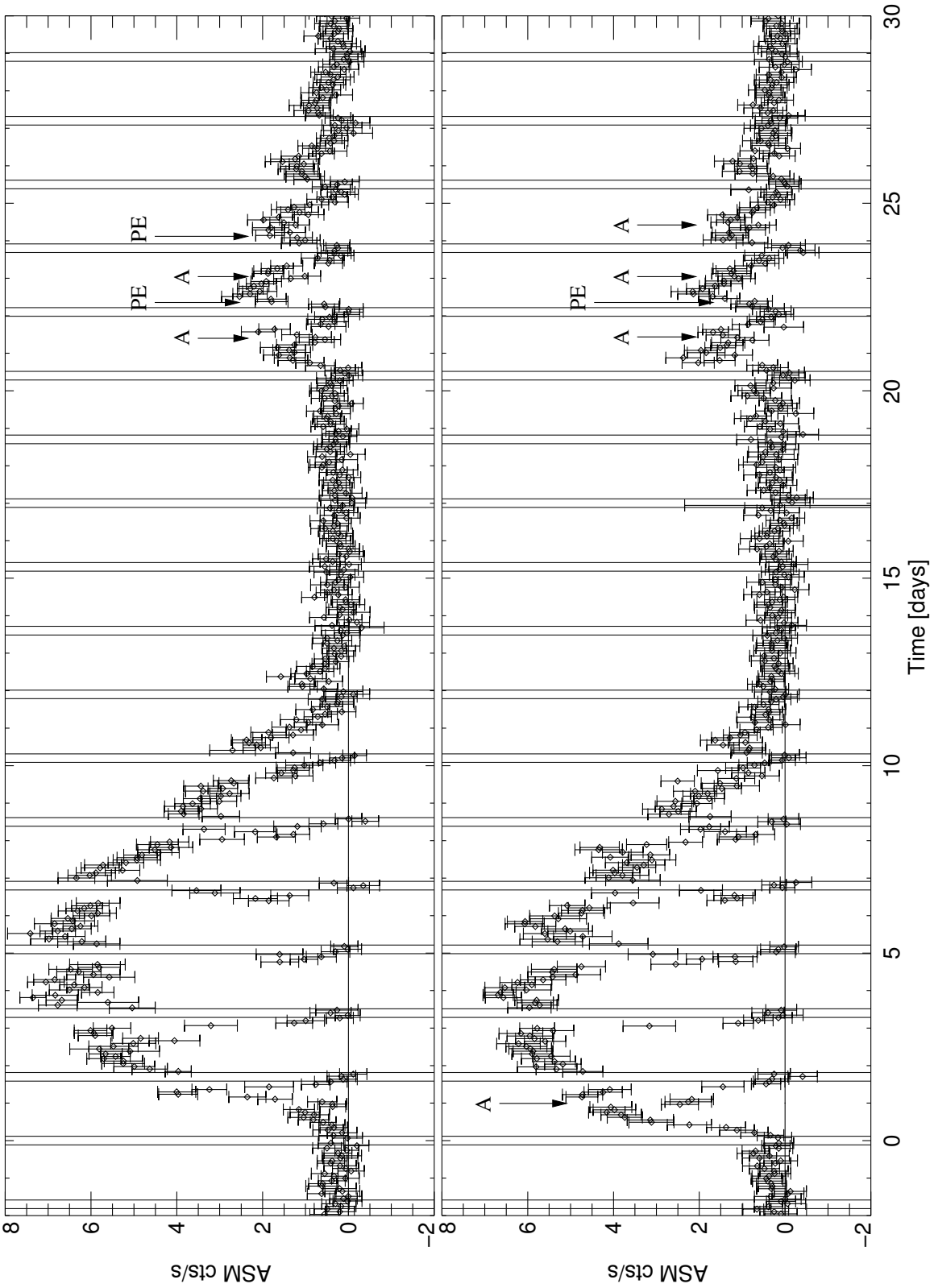

Figure 4.15 Averaged 35 d *ASM RXTE* light curves of Her X-1 for the cycles with turn-ons around $\phi_{\rm orb} = 0.7$ *(top)* and for the cycles with turn-ons around $\phi_{\rm orb} = 0.2$ *(bottom)*. Arrows mark anomalous dips (A) and post-eclipse recoveries (PE).

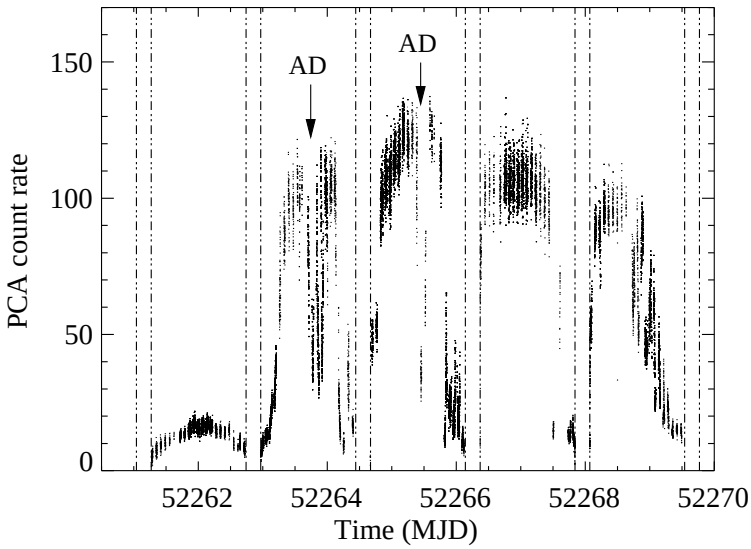

Figure 4.16 3–20 keV *PCA RXTE* light curve of Her X-1 during the short-on from one of the *RXTE* pointed observations. The arrows indicate anomalous dips (AD) that are present on two successive orbits after the beginning of the short-on state.

state. This is also seen on an individual short-on light curve taken with the *PCA* during a pointed *RXTE* observation (Fig. 4.16).

The fact that during the short-on state of Her X-1 more absorption dips appear on the X-ray light curve (the anomalous dips and post-eclipse recoveries during two successive orbits of the averaged short-on as well as in an individual short-on observed by the *PCA* (Figs. 4.15 and 4.16) suggests that the angle ϵ between the disk and the line of sight remains close to zero during the first two orbits after the turn-on in the short-on state. This is in contrast to the main-on state, where such features are observed only during one orbit after turn-on. This observation implies a generic asymmetry between the beginning of the main-on and short-on states. This asymmetry can take place only if the tilt of the disk, θ, changes with precession phase $\phi_{\rm pre}$. Indeed, the angle ϵ of the plane of the disk with the line of sight is

$$\sin\epsilon = \cos i\cos\theta + \sin i\sin\theta\cos\phi_{\rm pre}\,, \tag{4.11}$$

where i is the binary inclination angle. So with constant i and θ, $|d\epsilon/d\phi_{\rm pre}| \sim |\sin\phi_{\rm pre}|$, the same for precession phases with $\epsilon = 0$ (i.e. at the beginning of the both *on*-states), although the line of sight to the X-ray source lies nearer to the plane of the disk during the short-on state. As the binary inclination angle i could not change over the precession period, the only way to recover the asymmetry is to suppose that θ is a function of $\phi_{\rm pre}$. The physical reason of this is discussed below. The tilt of the disk is generally determined by the action of various torques acting on the disk. These include (1) the tidal torque from the optical star, (2) the dynamical torque caused by gas streams, (3) the viscous torque, (4) the torque caused by the radiation pressure and possibly (5) a disk wind torque, (6) magnetic torque at the inner rim of the disk from the neutron star's magnetosphere. The joint action of these torques determines the shape of tilted and twisted accretion disk (see, for example, calculations of the stationary disk shape for the disk wind model in Schandl & Meyer 1994). However, if the mass transfer rate through the inner Lagrange point into the disk changes with the precession phase, so will the tilt of the disk. For example, if free precession of the neutron star is ultimately responsible for the 35-day cycle in Her X-1 (see Section 3.3) the conditions of

X-ray illumination of the optical star's atmosphere will periodically change with the precessional phase. This in turn will lead to changes in the velocity components of the gas stream in the vicinity of the inner Lagrangian point and hence in the matter supply rate to the accretion disk.

As a first approximation the periodic change of the tilt of the disk with precessional phase can be parameterized in the form

$$\theta = \theta_0[a + b\cos(\omega_{\rm pre}t + \Delta)]\,, \tag{4.12}$$

where $\omega_{\rm pre}$ is the 35 d precessional frequency, Δ is the phase delay, and a and b are numerical constants. The phase delay Δ is zero for the observer whose line of sight is perpendicular to the disk's node line at the extrema of the disk tilt θ, which is quite improbable. So in general one expects $\Delta \neq 0$. The effect of the disk tilt changing with the angle ϵ is shown in Figure 4.17 for different phase delays $\Delta = 0$, 30° and 60°. It is seen that in a fairly broad range of Δ the possibility appears for ϵ to be close to zero during several orbits in the short-on state.

4.4.2 The model for reproducing the behavior of dips

In this section we qualitatively describe our model for reproducing the observed anomalous dip behavior, which is based on the model of Shakura et al. (1999). The detailed numerical calculations can be found in Appendix C and Klochkov et al. (2006). As mentioned in Sections. 3.2.2 and 3.3, the anomalous dips and post-eclipse recoveries can be attributed to the wobbling of the outer parts of the accretion disk. The wobbling of the outer disk rim occurs twice during the orbital binary period and is primarily caused by the tidal torques (Katz et al. 1982; Levine & Jernigan 1982). The tidal torque vanishes when the companion crosses the node line of the disk, so a wobbling appears as a sine-like component with one half of the synodic orbital period on top of the mean disk tilt. This explains, in addition to the occurrence of the turn-ons at the preferred 0.2 and 0.7 binary phases, the appearance of anomalous dips during the first orbit after the turn-on both in the main-on and in the short-on states. The appreciable tidal wobbling (with the amplitude of order of one degree) can be experienced by the disk with the outer radius $r_{\rm d} \sim 0.3a$ (a is the binary separation). In our model the accretion stream (which is non-complanar with the orbital plane, see Section 3.3) exerts a torque tilting the disk, which counterbalances the viscous torque and therefore limits the tilt of the disk (Bardeen & Petterson 1975). So the outer regions of the accretion disk are normally kept tilted at some equilibrium angle defined by the joint action of viscous and dynamical torques. This model allows to successfully reproduce the phase behavior of pre-eclipse dips as the result of regular screening of the X-ray source by the out-of-the-orbital-plane. The accretion stream also exerts a torque which reduces the precession rate of the disk to the observed value (the period of the tidal precession is shorter than $20.5P_{\rm orb}$, see Section 3.3 and Shakura et al. 1999).

Our calculations show that the gas stream impacts the tilted disk deeply inside its outer radius at distances $r_{\rm imp} \sim 0.1a$ from the neutron star. Assuming the standard accretion disk, the viscous time from the impact region to the disk center is around 10 days, and scales as $r^{3/2}$. However, the region of the disk beyond $r_{\rm imp}$, where there is no matter supply (called the "the stagnation zone") and which mediates the angular momentum transfer outwards for accretion to proceed, can react to perturbations induced by the stream impact much faster than on the viscous time scale. Indeed, in a binary system, tidal-induced standing structures can appear in the outer zone of the accretion disk (see e.g. Blondin 2000, and references therein) and perturbations of angular momentum can propagate through this region with a velocity close to the sound speed (while the matter will accrete on the

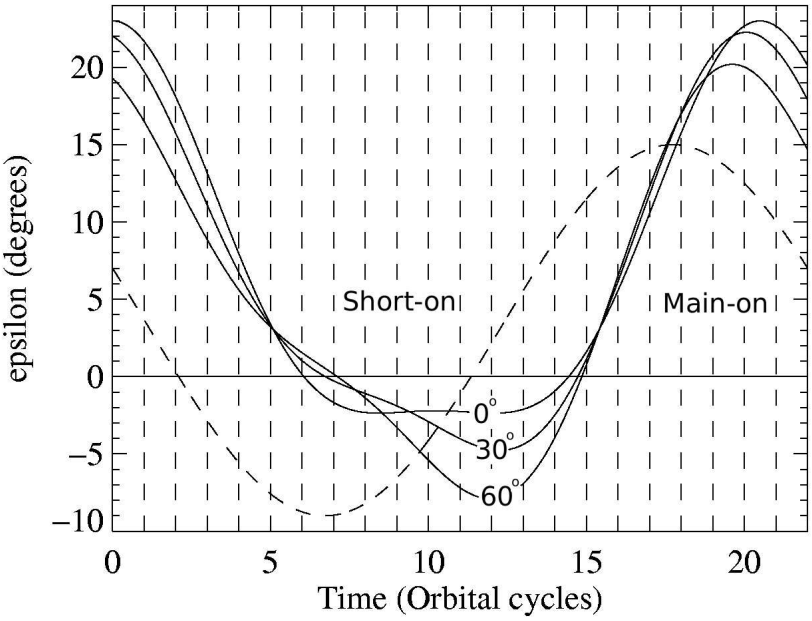

Figure 4.17 The effect of changing tilt of the disk on the angle ϵ between the line of sight and the outer plane of a flat disk (solid lines) for different phase delays $\Delta = 0$, 30° and 60°. The phase delay causes the asymmetry in the short-on and main-on states. The larger Δ, the more asymmetric is the changing of ϵ. The dashed sine-like curve shows the changing of ϵ for the inner parts of the twisted disk.

much slower viscous time scale!). Recent analysis of broad-band variability of SS 433 (Revnivtsev et al. 2006) suggests that such a picture is realized in the accretion disk in that source.

The physical picture of the change of the disks tilt adopted here is as follows. The rate of mass transfer $\dot{M}$ supplied by HZ Her (which for a given moment can be different from the accretion rate of the neutron star because the viscous time scale for mass transport through the disk both delays and smoothes the mass flow) changes periodically over the precession cycle in response, for example, to changing illumination of the optical star atmosphere due to free precession of the neutron star as well as the changing shading by the disk itself. The stream's action causes the outer disk to precess slower than it would do if only tidal torque was acting, and it also changes the outer disk tilt on the dynamical time scale of about 10 days (see below), which is sufficient to explain periodic disk tilt variations over the precession cycle. The wobbling of the outer disk is mainly due to tidal forces (the dynamical action of the stream provides minor contribution). The viscous time scale in the "stagnation zone" is much longer, so the viscous torques cannot smooth out the external disk variations.

In Appendix C we present details of the calculation of the disk wobbling under the action of tidal and stream torques, and the result is shown in Figure 4.18 for the standard accretion disk semi-thickness $H/R = 0.04$. In these calculations, there are two characteristic radii: the outer radius

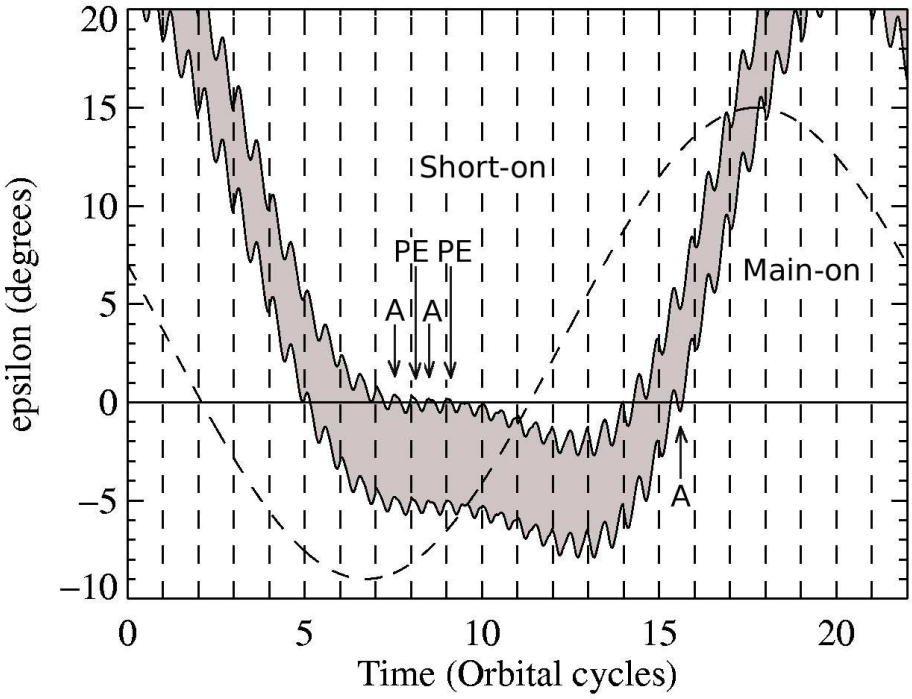

Figure 4.18 he angle ϵ between the direction from the center of the neutron star to the observer and to the outer parts of the accretion disk with non-zero thickness. The dashed sine-like curve shows schematically the angle ϵ for the inner accretion disk regions which eclipses the X-ray source at the end of on-states. The vertical dashed lines mark centers of the binary eclipses. Arrows mark anomalous dips (A) and post-eclipse recoveries (PE). The binary system inclination i, parameters θ_0 and Δ of the disk tilt change (Eq.4.12) and twisting angle of the disk (determining the location of the inner disk regions in this figure) are chosen such that to reproduce the observed durations of the main-on and short-on states and the observed behavior of anomalous and pre-eclipse dips.

of the disk $r_{\rm out} \sim 0.3a$ which determines the tidal wobbling amplitude, and the effective radius $r_{\rm eff} \sim 0.18a$ which determines the mean precession motion of the disk. The value of this effective radius is found from the requirement that the net precession period of the entire disk be equal to the observed value $20.5P_{\rm orb}$ and the dynamical time scale $t_{\rm d} = M_{\rm d}/\dot{M}$ (which characterizes the dynamical action of the stream) be 10 days. This value for the dynamical time is chosen to be of order of the viscous time from the impact radius $\sim 0.1a$ to meet (quasi) stationary conditions: at larger $t_{\rm d}$ the disk would rapidly empty out, at smaller $t_{\rm d}$ the matter would be stored in the disk. We emphasize again that the changing tilt of the outer parts of the disk (at $r_{\rm out}$) occurs very rapidly (on the sound velocity time scale!), while the precessional motion of the entire disk changes on much longer dynamical time scale $t_{\rm d}$ in response to the $\dot{M}$ variations.

Figure 4.18 shows the result of the calculations (see Appendix C) of the angle ϵ between the direction from the center of the neutron star to the observer and to the outer parts of the accretion disk with non-zero thickness. The complex shape of the disks wobbling is clearly seen. The sine-like dashed curve shows schematically the angle ϵ for the inner accretion disk regions which eclipses the X-ray source at the end of on-states. The horizontal line is the observer's plane and the vertical dashed lines mark centers of the binary eclipses. The main-on and short-on states are indicated. The source is screened by the disk when the observer is in the shaded area or between this area and the inner disk line. It is seen that the wobbling effects can be responsible for the observed (several) anomalous dips and post-eclipse recoveries at the beginning of the short-on state. These additional dips become more pronounced with the disk tilt decreasing and possibly we see them as unusual anomalous dips and post-eclipse recoveries at the end of the short-on preceeding the anomalous low state observed by *BeppoSAX* (Oosterbroek et al. 2000) and *RXTE* (Still et al. 2001).

Chapter 5

INTEGRAL observations of Her X-1

5.1 *INTEGRAL* observatory: mission overview

The **INTE**rnational **G**amma-**R**ay **A**strophysics **L**aboratory (*INTEGRAL*) was launched on 17 October 2002 on a highly eccentric orbit with the period of ~3 days. It is a 15 keV – 10 MeV gamma-ray observatory mission with concurrent source monitoring in the X-rays (3–35 keV) and in the optical range (V, 500–600 nm). The scientific goals of *INTEGRAL* are attained by high resolution spectroscopy with fine imaging and accurate positioning of celestial sources of gamma-ray emission. The *INTEGRAL* payload consists of two main gamma-ray instruments: the Spectrometer, *SPI*, and the Imager *IBIS*. Each of them has both spectral and angular resolution, but they are differently optimized in order to complement each other and to achieve overall excellent performance. These instruments are supported by two monitor instruments which provide complementary observations in the X-ray and optical energy bands: X-Ray Monitor *JEM-X* and Optical Monitoring Camera *OMC*. The Spectrometer, Imager and *JEM-X* share a common principle of operation: they are all coded-mask telescopes. The overall view of the *INTEGRAL* is given at Figure 5.1. The main characteristics of the X-ray instruments are summarized in Table 5.1.

Three types of scientific observation strategies are distinguished for *INTEGRAL*:

- The first type uses the method of dithering: in order to suppress systematic effects on spatial and temporal background variations in the spectrometer (*SPI*) detectors, a controlled and systematic spacecraft dithering (Raster Scan) manoeuvre capability is required. Such manoeuvres consist of several off-pointings of the spacecraft pointing axis from the target.

- The second type of observation covers the “Galactic Plane Scan”. At weekly intervals, a saw-tooth-path scan inclined at 21° with regard to the galactic equator is employed. Each scan consists of a series of individual exposures of 965 s each. The individual exposures are separated by 6° along the scan path.

- The third type of observation is called “Galactic Centre Radian Deep Exposure”. This one is concentrated on the observation of the galactic center region for an accumulated time of about 46 days/year.

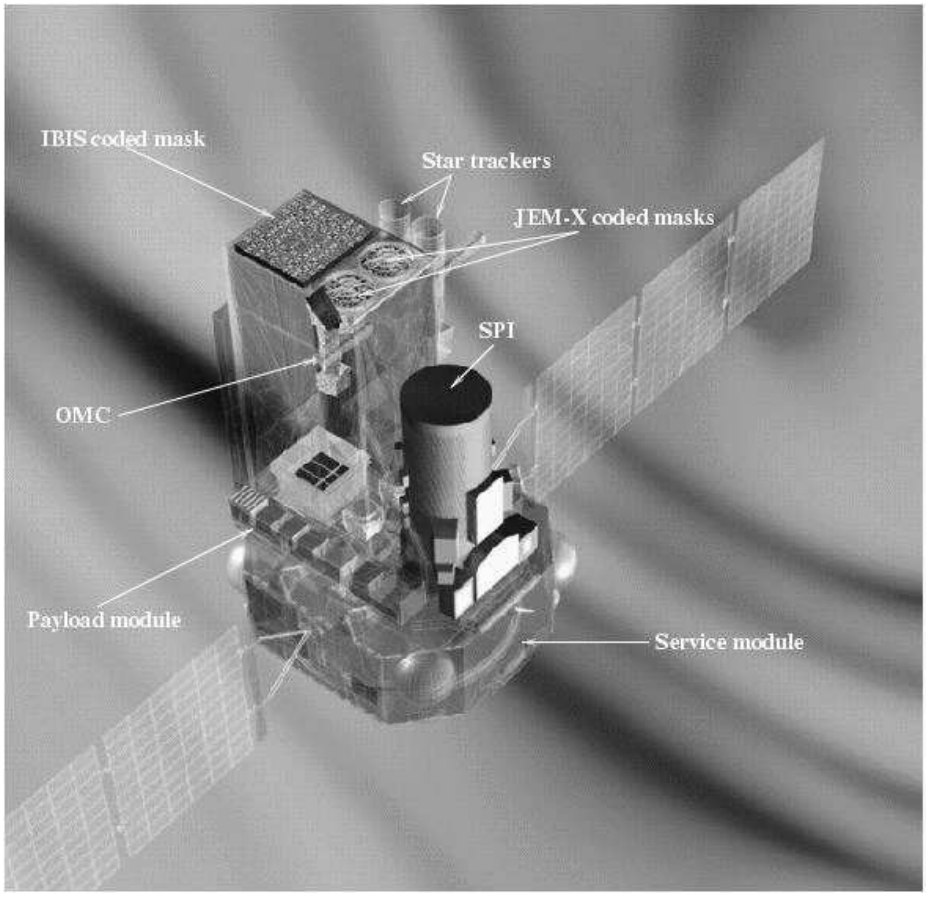

Figure 5.1 The *INTEGRAL* spacecraft with the payload module on the top of the service module. The coded masks for *IBIS* and *JEM-X* are located 3.2 m above the detection planes. *IBIS* and *JEM-X* detectors are inside the payload module structure.

Table 5.1 Main characteristics of the *INTEGRAL* instruments.

Property	***SPI***	***IBIS***	***JEM-X***
Energy range	20 keV–8 MeV	15 keV–10 MeV	3 keV–35 keV
Detector	19 Ge detectors cooled to 85K	16384 CdTe detectors (ISGRI) 4096 CsI detectors (PICsIT)	Microstrip Xe/CH_4-gas detector (1.5 bar)
Detector area (cm^2)	500	2600 (CdTe), 3100 (CsI)	2×500
Spectral resolution (FWHM)	2.3 keV 1.3 MeV	9 keV 100 keV	1.2 keV 10 keV
Field of view (fully coded)	16°(corner to corner)	$9° \times 9°$	4.8°
Angular resolution (FWHM)	2.5° (point source)	12′	3′
Source location (radius)	$< 1.3°$	$< 1'$	$< 30''$
Absolute timing accuracy (3σ)	129 μs	92 μs	122 μs

5.1.1 IBIS

The Imager *IBIS* provides diagnostic capabilities of fine imaging (12 arcmin FWHM), source identification and spectral sensitivity to both continuum and broad lines over a broad (15 keV – 10 MeV) energy range. The Imager exploits simultaneously with the other instruments on *INTEGRAL* celestial objects of all classes ranging from the most compact galactic systems to extragalactic objects. A tungsten coded-aperture mask (located at 3.2 m above the detection plane) is optimized for high angular resolution. As diffraction is negligible at gamma-ray wavelengths, the angular resolution obtainable with a coded mask telescope is limited by the spatial resolution of the detector array (the scale of the coding pattern of the mask is equally important but it is usually chosen according to the detector resolution). The Imager design takes advantage of this by utilizing a detector with a large number of spatially resolved pixels implemented as physically distinct elements. The detector uses two planes: one 2600 cm^2 front layer of Cadmium-Telluride (CdTe) pixels, each (4x4x2) mm (width x depth x height); and a 3100 cm^2 layer of Caesium-Iodide (CsI) pixels, each (9x9x30) mm. The CdTe array (*ISGRI*) and the CsI array (*PICsIT*) are separated by 90 mm. The detector provides the wide energy range and high sensitivity continuum spectroscopy required for *INTEGRAL*. The two-layer structure allows the paths of the photons to be tracked in 3D, as they scatter and interact with more than one element. Events can be categorized and the signal to noise ratio improved by rejecting those which are unlikely to correspond to real (celestial) photons, e.g. towards the high end of the energy range. The aperture is restricted by a lead shielding tube and shielded in all other directions by an active Bismuth Germanate (BGO) scintillator veto system. Additional information about *IBIS* can be found in Ubertini et al. (2003).

5.1.2 *SPI*

The spectrometer *SPI* performs spectral analysis of gamma-ray point sources and extended regions in the 20 keV – 8 MeV energy range with an energy resolution of 2.2 keV (FWHM) at 1.33 MeV. This is accomplished with an array of 19 hexagonal high purity Germanium detectors cooled by a Stirling cooler system to an operating temperature of 85 K. A hexagonal coded aperture mask is located 1.7 m above the detection plane in order to image large regions of the sky (fully coded field of view is 16°) with an angular resolution of 2°. In order to reduce background radiation, the detector assembly is shielded by a veto (anticoincidence) system which extends around the bottom and side of the detector almost completely up to the coded mask. The aperture (and hence contribution by cosmic diffuse radiation) is limited to 30°. A plastic veto is provided below the mask to further reduce the 511 keV background. Additional information about *SPI* can be found in Vedrenne et al. (2003).

5.1.3 *JEM-X*

The Joint European X-Ray Monitor *JEM-X* supplements the main *INTEGRAL* instruments and plays a crucial role in the detection and identification of the gamma-ray sources and in the analysis and scientific interpretation of *INTEGRAL* gamma-ray data. *JEM-X* makes observations simultaneously with the main gamma-ray instruments, albeit with a narrower field of view, and provides images with arcminute angular resolution in the 3–35 keV prime energy band. The baseline photon detection system consists of two identical high pressure imaging microstrip gas chambers (1.5 bar, 90% Xenon + 10% Methane). Each detector unit views the sky through its coded aperture mask located at a distance of approximately 3.2 m above the detection plane.

Due to unforeseen problems with eroding anodes, detected after launch, the high voltage inside the two *JEM-X* detectors had to be lowered, reducing the gain by a factor of 3 for *JEM-X* 1 and a factor of 2 for *JEM-X* 2. As additional safeguard measure, only *JEM-X* 1 is operated for normal observations at the time of writing while *JEM-X* 2 is being kept in a safe state. Additional information about the instrument can be found in Lund et al. (2003).

5.2 Observations and data reduction

5.2.1 Summary of observations

Her X-1 was observed by *INTEGRAL* on July 22 – August 3, 2005 (MJD 53573–53585) in response to the proposal by N. I. Shakura et al. The observations include ∼5 orbital revolutions of the satellite: revolutions. 338, 339, 340, 341, and 342. The total exposure time is ∼630 ksec. The observations were performed in the “dithering” mode (see Section 5.1). Due to a strong solar flare during the revolution 341 a part of the low-energy data (*JEM-X*) was rejected. The total exposure times for each of the three X-ray instruments are listed in Table 5.2. The *INTEGRAL* observations are made of many pointings of about 30 minutes (∼2 ksec) separated by slews. Each pointing and slew, or a part of them if they are too long, is called a *Science Window* (ScW). Only pointing ScWs are usually used to extract useful scientific information. The Her X-1 observations contain 205 pointing ScWs.

Table 5.2 Summary of observations.

Instrument	Total good time (s)
ISGRI	440867
SPI	523263
JEM-X	410668

5.2.2 *IBIS/ISGRI* data processing

As mentioned in Section 5.1.1, the *IBIS* telescope is a device based on a coded aperture imaging system. Below we briefly describe the working concept of such instruments. More details can bee found in e.g. Caroli et al. (1987) or Skinner & Ponman (1994). Any coded mask camera consists of (1) a coded mask, i.e. a plate with areas that are transparent or opaque to photons with energies in a certain range and distributed in a pre-determined pattern, and (2) a position-sensitive detector, whose spatial resolution is sufficiently matched to the mask-pattern grid size. The principle of the camera is straightforward: photons from a certain direction in the sky project the mask onto the detector; this projection has the same coding as the mask pattern, but is shifted relative to the central position over a distance uniquely correspondent to the direction of the photons. The detector accumulates the sum of a number of shifted mask patterns, one for each source in the sky (individual photons are measured). Each shift encodes the position and its strength encodes the intensity of the sky at that position. It is clear that each part of the detector may detect photons incident from any position within the observed sky. After a certain illumination period, the accumulated detector image – *shadowgram* – may be decoded to a sky image using the method described below. The mask chosen for *IBIS* is based on a cyclic replication of MURA (Modified Uniformly Redundant Array) of order 53, expanded to 95 pixels. Such a pattern has the remarkable property that its cyclic autocorrelation gives a delta function. The decoding principle is the following. Representing the mask with an array M of "1" (open elements) and "0" (opaque ones), the detector array D will be given by the convolution of the sky image S by M plus an unmodulated background array term B:

$$D = S \star M + B \tag{5.1}$$

Let us define the decoding array G as inverse to M where $G = 2M - 1$ (i.e., $G = +1$ for $M = 1$ and $G = -1$ for $M = 0$). With the help of array G we can reconstruct the sky:

$$S' = D \star G = S + B \star G. \tag{5.2}$$

where S' differs from S only by the $B \star G$ term, which for a flat array B is a constant level that can be measured and removed.

For the analysis of the *IBIS/ISGRI* data we used the version 6.0 *Offline Science Analysis* (OSA) software distributed by ISDC (Courvoisier et al. 2003). The processing pipeline is divided into the following steps:

- *COR – Data Correction:* Tags noisy pixels of the detector, corrects energy of the photons for different effects, transforms channels to energy.

- *GTI – Good Time Handling:* Generates, selects, and merges *Good Time Intervals* (GTI) to produce a unique GTI that is then used by the software to select good events.
- *DEAD – Dead Time Calculation:* Calculates the total dead time during which incoming photons may be lost due to the processing of the previous events.
- *BIN_I – Event Binning for Imaging:* Sorts data into energy bins. For each energy range, the intensity shadowgram and a corresponding efficiency map are created.
- *BKG_I – Background Correction:* Creates rebinned maps for background and absorption of support mask corrections. Corrects for efficiency and subtracts background.
- *CAT_I – Catalog Source Selection for Imaging:* Selects from the given catalog a list of sources in the Field of View matching the criteria defined by script parameters, and creates an output list with location and expected flux values of the selected sources.
- *IMA – Image Reconstruction:* Shadowgrams are deconvolved, a source search is performed in the single images as well as in the mosaic (combination of different images) and a list of detected sources is created.
- *BIN_S – Event Binning for Spectra:* Creates rebinned maps for background and absorption of support mask corrections. Sorts data into energy bins. For each energy range the shadowgram and a corresponding efficiency shadowgram is created.
- *SPE – ISGRI spectra extraction:* For each source of interest, one PIF[1] is produced. Spectral extraction is done for all catalog sources with the use of these PIFs.
- *LCR – source light curve extraction:* For all sources from the input catalog light curves are extracted.

For the pulse-phase-resolved spectroscopy we also used the software developed at IASF, Palermo (Mineo et al. 2006).

One of the main goals of our observations was the precise measuring of the position of the cyclotron line in the spectrum of Her X-1 (see Section 3.2.4). As this measurement is mainly based on the *ISGRI* data, it requires a reliable energy scale of the instrument. To check the energy calibration we constructed the energy spectra of all events detected during each pointing. The spectra are completely dominated by the instrumental background (see Fig. 5.2). It was found that the tungsten fluorescence line which is most prominent (shown by the thick arrow) is shifted to lower energies by ~1.5 keV with respect to its nominal position, 59.3 keV. We interpreted this shift as a result of a non-corrected time-dependent gain shift of the instrument. To correct this effect we modeled the background spectrum of each ScW by the sum of a power-law continuum with an exponential cut-off and five gaussians representing the background emission lines. This allowed us to determine the energy of the tungsten line which we then used to calculate the gain for each ScW. Figure 5.3 shows the measured energy of the line for the revolution 339. In order to apply the corresponding energy correction we stopped the OSA pipeline at the COR level, updated the energies of all events according to the calculated gain and resumed the analysis.

[1] PIF is a number between 0 and 1, which expresses the theoretical degree of illumination of each detector pixel for a given source in the sky.

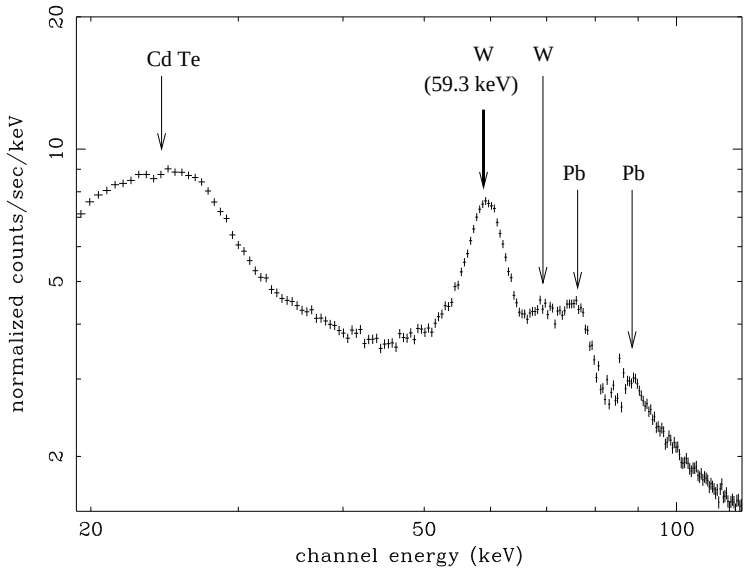

Figure 5.2 *IBIS/ISGRI* background spectrum accumulated during one ScW. Background emission lines are indicated. The thick arrow shows the 59.3 keV tungsten fluorescence line that was used to correct the energy scale (see text).

5.2.3 *SPI* data processing

The spectrometer *SPI* is also a coded mask instrument. It has, however, lower angular resolution as it mostly optimized for spectral study of sources. The principles of image reconstruction are similar to those of *ISGRI* (see above). The analysis of the Her X-1 observations is done using the standard pipe-line of OSA 6.0 without any additional corrections. An overview of the successive steps of the standard pipe-line is given below:

- *CAT_I:* Extracts from the *INTEGRAL* reference catalogue information (position and flux) about known sources lying in the field-of-view.
- *BIN_I:* Extracts the start/stop times and the *SPI* attitude for all pointings included in the observation, and stores the results. On request, this program can access a list of bad pointings (usually of order of 1–2% of the total) and exclude them from the further analysis.
- *BKG_I:* Defines the energy bins. Performs on-the-fly energy correction, event binning, and derivation of the dead times. Computes background models from different indicators.
- *IMA/SPE/LCR:* Carries out image reconstruction (IMA), spectral extraction (SPE) or timing analysis (LCR) depending on the chosen "mode". This is the most difficult and critical step. If the pulse phase binning has been selected (e.g. for a pulsar), all phase bins are processed independently in turn. Creates the appropriate RMF response matrix required for XSPEC spectral fitting.

5.2.4 *JEM-X* data processing

JEM-X is based on the same principle as the two gamma-ray instruments on *INTEGRAL*. The processing of the *JEM-X* data was also done with the OSA 6.0 pipe-line provided by ISDC

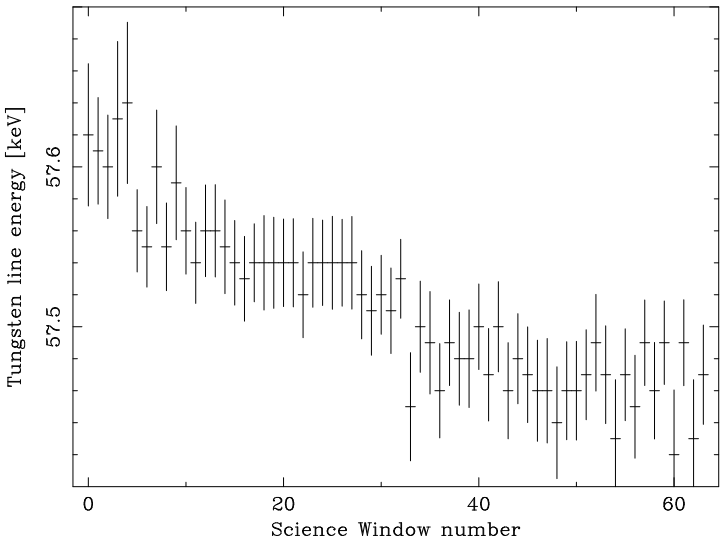

Figure 5.3 Tungsten fluorescence line energy in the *ISGRI* background spectrum during the revolution 339. The nominal energy of the line is 59.3 keV.

without additional corrections. The data analysis steps are very similar to those of *ISGRI* (see Section 5.2.2).

5.3 Timing analysis

5.3.1 Light curve

Figure 5.4 shows light curves of Her X-1 obtained with *ISGRI* (20–100 keV, top) and *JEM-X* (3–20 keV, bottom). The observations partially cover a main-on state of the source, 35 d phases $\phi_{\rm pre} \sim 0.0-0.11$ and $0.20-0.28$ ($\phi_{\rm pre} = 0$ corresponds the turn-on moment of the source). As one can see the turn-on occurred at MJD $\sim$ 53574.7 and orbital phase $\phi_{\rm orb} \sim 0.7$. The solid curve on top of the *JEM-X* light curve is the *ASM RXTE* light curve averaged over many 35 d cycles with turn-ons around $\phi_{\rm orb} \sim 0.7$ (see Section 4.4) and stretched vertically to match the one from *JEM-X*. As mentioned above, all *JEM-X* data from the revolution 341 were rejected due to a strong solar flare. The data points with high count rate during the revolution 342 in the bottom panel of Figure 5.4 are probably due to a underestimated background caused by the flare. It is seen that the light curve is quite typical for Her X-1. The characteristic details such as X-ray eclipses (marked by vertical dashed lines) and pre-eclipse dips (sharp decrease of the flux just before the eclipse, see Section 3.2.2) marching to earlier orbital phases at consecutive orbits are clearly seen.

5.3.2 Pulse profiles

To construct 1.24 s pulse profiles of the source all times were translated to the solar system barycenter and corrected for orbital motion in the binary. The orbital parameters used for the binary correction were calculated using the orbital ephemeris determined in Section 4.2:

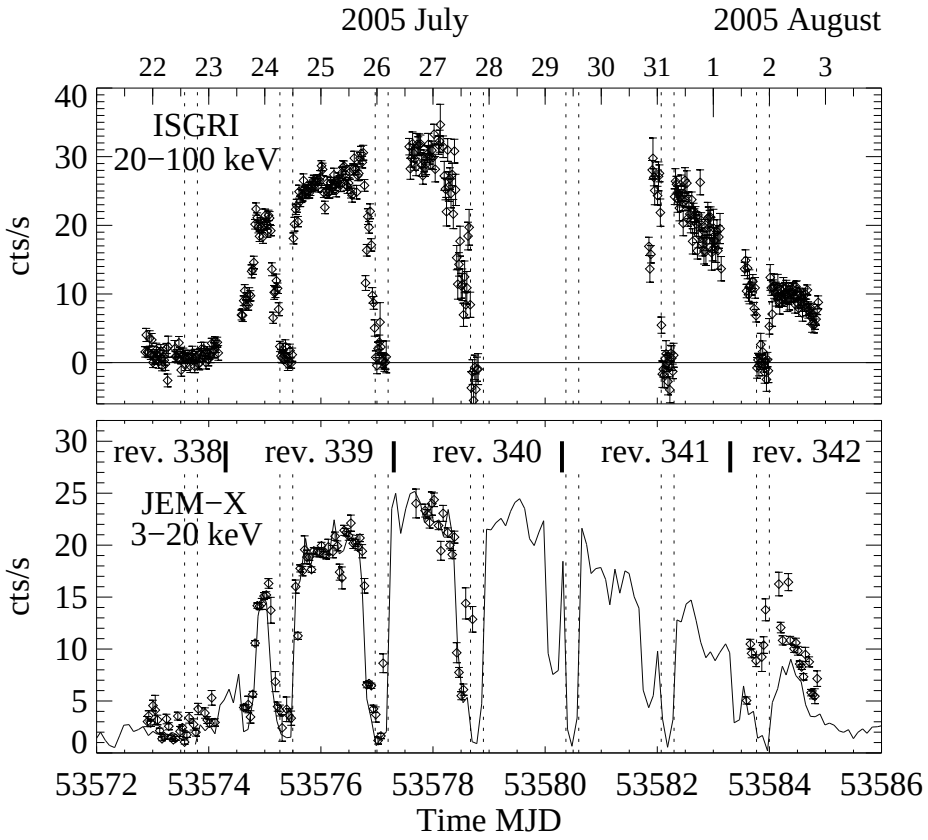

Figure 5.4 X-ray light curve of Her X-1 obtained with *ISGRI (top panel)* and *JEM-X (bottom panel)*. The solid curve in the bottom panel shows the *ASM RXTE* light curve averaged over many 35 d cycles. Satellite revolution numbers are indicated.

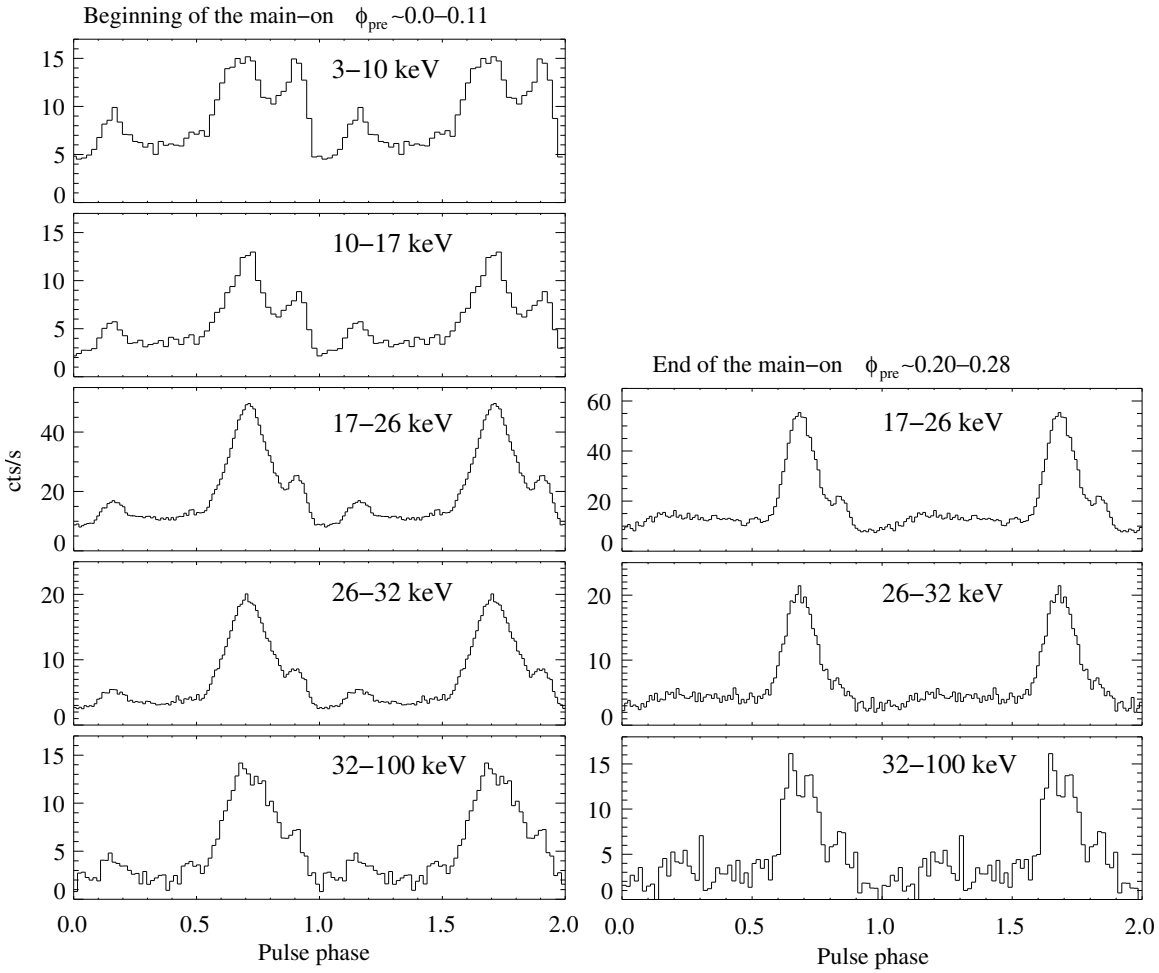

Figure 5.5 Energy-resolved X-ray pulse profiles of Her X-1 at the beginning of the main-on (left column) and at the end of the main-on (right column).

$$
\begin{aligned}
P_{\rm orb} &= 1.700167233\ {\rm d},\\
T_{\frac{\pi}{2}} &= 53571.982111\ ({\rm MJD}),\\
a\sin i &= 13.1831\ {\rm light\ sec}.
\end{aligned}
$$

As a folding period for constructing pulse profiles we used the period obtained with the standard epoch folding method: $P_{\rm spin} = 1.23775836(10)$ s.

It was found that the pulse profiles do not change significantly during the beginning (revolutions 339 and 340) and during the end (revolution 341) of the main-on state. Therefore, we constructed the pulse profiles separately for these two intervals without further splitting in time. We excluded the data falling inside X-ray eclipses, pre-eclipse dips or located outside the main-on state (during the off-state the data are very noisy and show only marginal sine-like pulsations). The resulting energy-resolved pulse profiles are shown in Figure 5.5. It is seen that the profiles change significantly from the beginning to the end of the main-on state. The main peak is stronger and

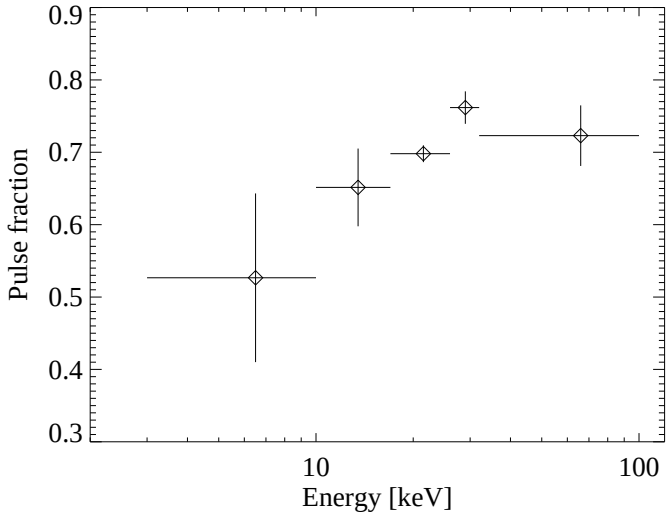

Figure 5.6 Pulse fraction of Her X-1 as a function of energy.

narrower at the end of the main-on. The interpulse almost disappears. This behavior is typical for Her X-1: analogous pulse profiles were observed by *RXTE* at different times (see e.g. Kuster et al. 2005). We also studied the energy-dependence the pulse fraction P determined as:

$$P = \frac{I_{\max} - I_{\min}}{I_{\max} + I_{\min}}, \tag{5.3}$$

where $I_{\max}$ and $I_{\min}$ are background-corrected count rates in the maximum and minimum of the pulse profile respectively. It is clearly seen (Fig. 5.6) that the pulse fraction increases with energy. The structure of the profile is also energy-dependent, going from a double-peaked shape at lower energies to an almost single-peaked at higher energies. The main peak becomes narrower toward higher energies.

5.3.3 Pulse period behavior

To explore more precisely the intrinsic (not affected by the orbital motion in the binary) spin period of the neutron star $P_{\rm spin}$ during the *INTEGRAL* observations we used the phase-connection method described in Section 4.2.1. Figure 5.7 shows the observed pulse arrival times minus calculated using a constant pulse period. The linear fit to the data corresponding to a constant pulse period (dashed line) gives $\chi^2_{\rm red} = 1.9$ for 23 d.o.f. while the quadratic fit corresponding to the presence of a non-zero $\dot{P}_{\rm spin}$ results in $\chi^2_{\rm red} = 1.0$ for 22 d.o.f. We conclude, therefore, that the neutron star is spinning up with $-\dot{P}_{\rm spin} = (5.8 \pm 1.5) \times 10^{-13}$s/s. This value is significantly higher than the averaged spin-up trend of Her X-1 which is $\sim 1.1 \times 10^{-13}$ s/s (see Section 4.3.4 and Fig. 4.9). This shows strong local variability of the pulse period on the time scale of a few days.

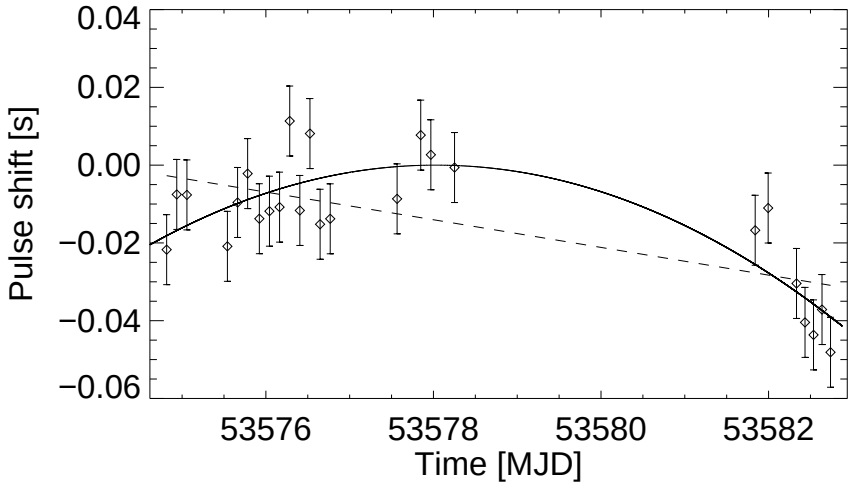

Figure 5.7 Observed pulse arrival times of Her X-1 minus calculated using a constant pulse period. The dashed line shows a linear fit corresponding to a constant pulse period while the solid line shows a quadratic fit corresponding to a non-zero $\dot{P}_{\rm spin}$.

5.4 Spectral analysis

The spectral analysis of the observations has been performed using the `XSPEC` v.11.3.2l spectral fitting package (Arnaud 1996). For the beginning of the main-on the data from all three X-ray instruments have been used. The fit, however, is mainly driven by *JEM-X* ($\lesssim$ 20 keV) and *ISGRI* ($\gtrsim$ 20 keV) data. The spectra obtained with *SPI* ($\gtrsim$ 22 keV) have much lower statistics. For the end of the main-on only the higher energy part of the spectrum is available since the *JEM-X* data were rejected due to a solar flare (see above). Following OSA User Manuals[2], we added systematic errors at a level of 2% to all *JEM-X* and *ISGRI* spectra in order to account for uncertainties in the response matrices of the respective instruments.

5.4.1 Pulse averaged spectrum.

For constructing the pulse-averaged spectrum, we used the data from revolutions 339 and 340 (the beginning of the main-on state, see Fig. 5.4). During this interval the data from all three X-ray instruments are available. Eclipses and dips were excluded from the analysis. To model the broad band spectral continuum we used a power law with an exponential cutoff (`highecut` model of `XSPEC`):

$$I_{\rm cont} \propto \begin{cases} E^{-\Gamma}, & \text{if } E \le E_{\rm cutoff} \\ E^{-\Gamma} \cdot \exp\left(\frac{E-E_{\rm cutoff}}{E_{\rm fold}}\right), & \text{if } E > E_{\rm cutoff}, \end{cases} \tag{5.4}$$

[2] http://isdc.unige.ch/index.cgi?Soft+download

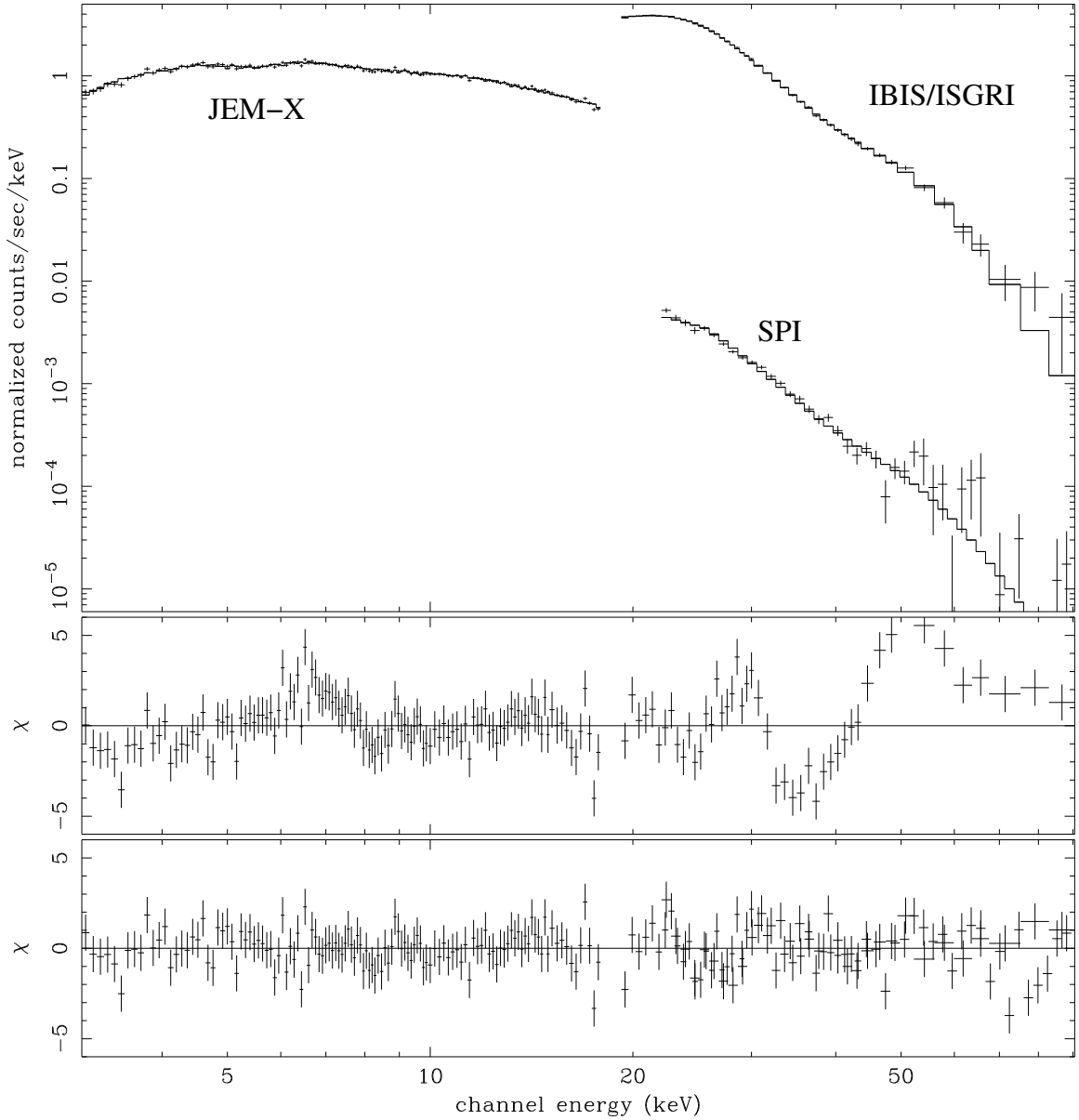

Figure 5.8 *Top:* The pulse-averaged X-ray spectrum of Her X-1 obtained during revolutions 339 and 340 (beginning of the main-on); *middle:* residuals after fitting the spectrum with the continuum model described by Eq. 5.4 without introducing the iron emission line and cyclotron absorption line (to avoid confusion the *SPI* data are not shown in this panel, their statistics is low); *bottom:* the residuals after inclusion of the iron and cyclotron lines in the model.

Table 5.3 Best fit spectral parameters of Her X-1. 1σ(68%)-uncertainties for one parameter of interest are shown.

Parameter	Value
Γ	0.91 ± 0.01
$E_{\rm cutoff}$ [keV]	$25.5^{+0.2}_{-0.3}$
$E_{\rm fold}$ [keV]	$9.0^{+0.3}_{-0.2}$
$E_{\rm Fe}$ [keV]	$6.57^{+0.11}_{-0.13}$
$\sigma_{\rm Fe}$ [keV]	$0.50^{+0.17}_{-0.16}$
$E_{\rm cycl}$	$38.2^{+0.79}_{-0.62}$
$\sigma_{\rm cycl}$	$9.3^{+0.4}_{-0.5}$
$\tau_{\rm cycl}$	$0.63^{+0.04}_{-0.06}$
$F_{\rm JEM\text{-}X}$	1.0 (fixed)
$F_{\rm ISGRI}$	$0.81^{+0.01}_{-0.02}$
$F_{\rm SPI}$	0.96 ± 0.02
$\chi^2_{\rm red}$/d.o.f.	1.19/207

where E is the energy of the photons; Γ, $E_{\rm cutoff}$, and $E_{\rm fold}$ are model parameters. A Gaussian line is added to model the iron emission line at ~6.5 keV. The cyclotron absorption feature is firmly observed and modeled with a Gaussian absorption line at ~38.2 keV. So, the final spectral function I is the following:

$$I = I_{\rm cont} \cdot \exp\left\{-\tau_{\rm cycl} \exp\left(-\frac{(E-E_{\rm cycl})^2}{2\sigma^2_{\rm cycl}}\right)\right\} + K \exp\left(-\frac{(E-E_{\rm Fe})^2}{2\sigma^2_{\rm Fe}}\right), \quad (5.5)$$

where $E_{\rm cycl}$ and $\sigma_{\rm cycl}$ are the energy and width of the cyclotron line, $E_{\rm Fe}$ and $\sigma_{\rm Fe}$ are the energy and width of the iron emission line, and K is the numerical constant, describing the strength of the iron line. The count rate spectrum is shown in Figure 5.8. The middle panel shows the residuals after fitting the spectrum with the continuum model without the iron emission line and the cyclotron absorption line. Systematic features around 6 and 40 keV are clearly seen.

To account for large systematic uncertainties in the absolute flux measured by the instruments we introduced in our models a free multiplicative factor for each instrument: $F_{\rm ISGRI}$, $F_{\rm SPI}$ and $F_{\rm JEM-X}$ (for *JEM-X* the factor was fixed to 1.0). The best-fit parameters with corresponding 1σ(68%)-uncertainties are listed in Table 5.3. The position of the cyclotron line ($38.2^{+0.79}_{-0.62}$ keV) is consistent with that measured by *RXTE* at a similar time (see Table 4.3.5) and, therefore, supports the found anti-correlation between the cyclotron line energy and the maximum main-on flux (Section 4.3.5).

We have checked the presence and the centroid energy of the cyclotron line using different continuum models (such as e.g. Fermi-Dirac cutoff, Tanaka 1986) as well as using different line profiles (e.g. Lorentzian profile). It was found that the presence and the energy of the feature are independent of the choice of the continuum and the line profile model. The `highecut` model

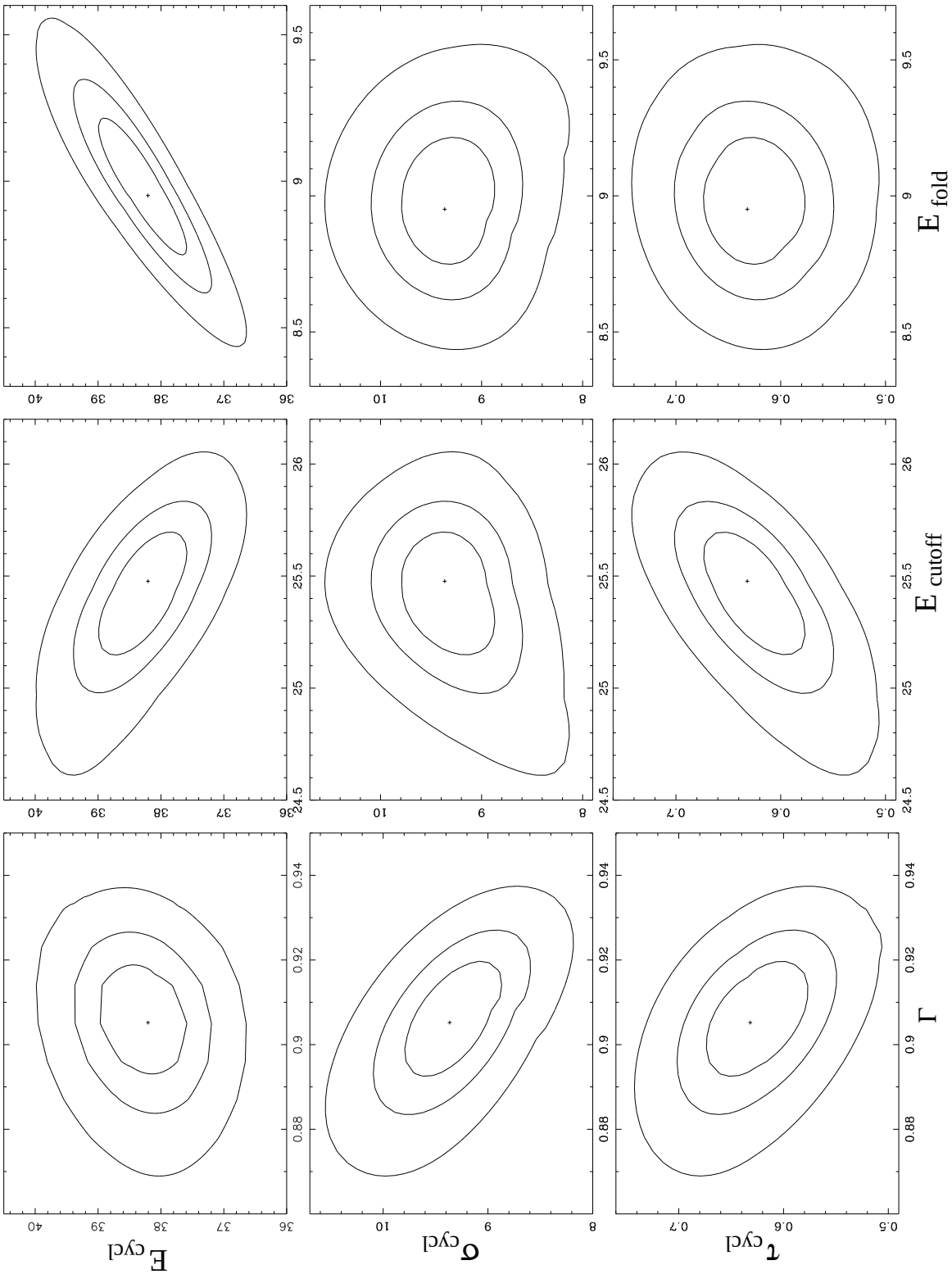

Figure 5.9 χ^2-maps for different pairs of parameters. The position of the minimum ($\chi^2_{\rm min}$) is marked by the cross. For each pair of parameters three contours are shown: ($\chi^2_{\rm min}$ + 1.0), ($\chi^2_{\rm min}$ + 2.71), and ($\chi^2_{\rm min}$ + 6.63).

was found to provide a better description of the spectral continuum in Her X-1 with respect to other models. Additionally, it allows to compare our results with previous observations of the source, most of which were analyzed using the `highecut` model (see e.g. Gruber et al. 2001). A discontinuity of the first derivative of the spectral function at $E_{\rm cutoff} \sim 25$ keV (which can be noticed in the residuals in Fig. 5.8) is far from the cyclotron line energy and does not affect the line parameters.

We also explored the pulse-average spectrum obtained during the revolution 341 (end of the main-on). The continuum spectral parameters are poorly constrained in this case due to the absence of the low-energy ($\lesssim 20$ keV) part of the spectrum. However, the found position of the cyclotron line $E_{\rm cycl} = 37.3^{+1.3}_{-1.1}$ keV is consistent with that measured in revolutions 339 and 340.

Since the cyclotron line characteristics are of particular interest, we check their possible dependencies on the continuum parameters by constructing χ^2-maps for pairs of parameters. The maps are shown in Figure 5.9. The position of the minimum ($\chi^2_{\rm min}$) is marked by the cross. For each pair of parameters three contours are shown: ($\chi^2_{\rm min} + 1.0$), ($\chi^2_{\rm min} + 2.71$), and ($\chi^2_{\rm min} + 6.63$). Projections of these contours onto the parameter axes correspond to the 68%, 90%, and 99% confidence intervals respectively. It is seen that in some cases the model parameters are significantly correlated ($E_{\rm cycl} - E_{\rm cutoff}, E_{\rm cycl} - E_{\rm fold}$). However, the χ^2-minimum is well defined in each case and the projections of the 68%-contours to the parameter axes are consistent with the uncertainties of the respective parameters quoted in Table 5.3 (also for those parameters which show significant correlation with the others).

5.4.2 X-ray dips

In the X-ray light curve taken with *INTEGRAL* one can see pre-eclipse dips on three subsequent orbits after the turn-on (Fig. 5.4). The turn-on of the source can be considered as egress from an anomalous dip at $\phi_{\rm orb} \sim 0.5$ (according to our model, the source is partially screened by the outer accretion disk rim in both cases: during the turn-on of the source and during anomalous dips). Thus, the light curve obtained with *INTEGRAL* contains three pre-eclipse dips and one anomalous dip. Using the *JEM-X* data we calculated the ratio $H = I_{8-20\,\rm keV}/I_{3-8\,\rm keV}$, where $I_{8-20\,\rm keV}$ and $I_{3-8\,\rm keV}$ are the count rates in the respective energy ranges. The ratio H as a function of time is shown in the bottom panel of Fig. 5.10. It can be seen that H increases during X-ray dips most probably indicating the low-energy absorption by the cold matter in the accretion stream (during the pre-eclipse dips) and in the outer rim of the disk (during the anomalous dip).

To check the absorption hypothesis we constructed *JEM-X* and *ISGRI* spectra corresponding to the dips and compared them with those obtained outside the dips. To fit the spectrum from the dips we used the approach of Kuster et al. (2005). It was assumed that a combination of direct and absorbed radiation is observed during the dips. Thus, we used a partial covering model which combines both, absorbed and non-absorbed spectra to fit the data during the dips. We used the same continuum model as in the previous section. The final spectral model can be written as

$$I(E) = A \cdot [1 + \alpha(E) \cdot I_{\rm cont}], \tag{5.6}$$

where $I_{\rm cont}$ is the continuum model described in the previous section, and

$$\alpha(E) = B \cdot e^{-N_{\rm H}\sigma_{\rm bf}(E)}, \tag{5.7}$$

where $\sigma_{\rm bf}(E)$ is the photoabsorption cross-section per hydrogen atom for matter of cosmic abundances (Bałucińska-Church & McCammon 1992) used in the `phabs` model of `XSPEC` and $N_{\rm H}$ is the

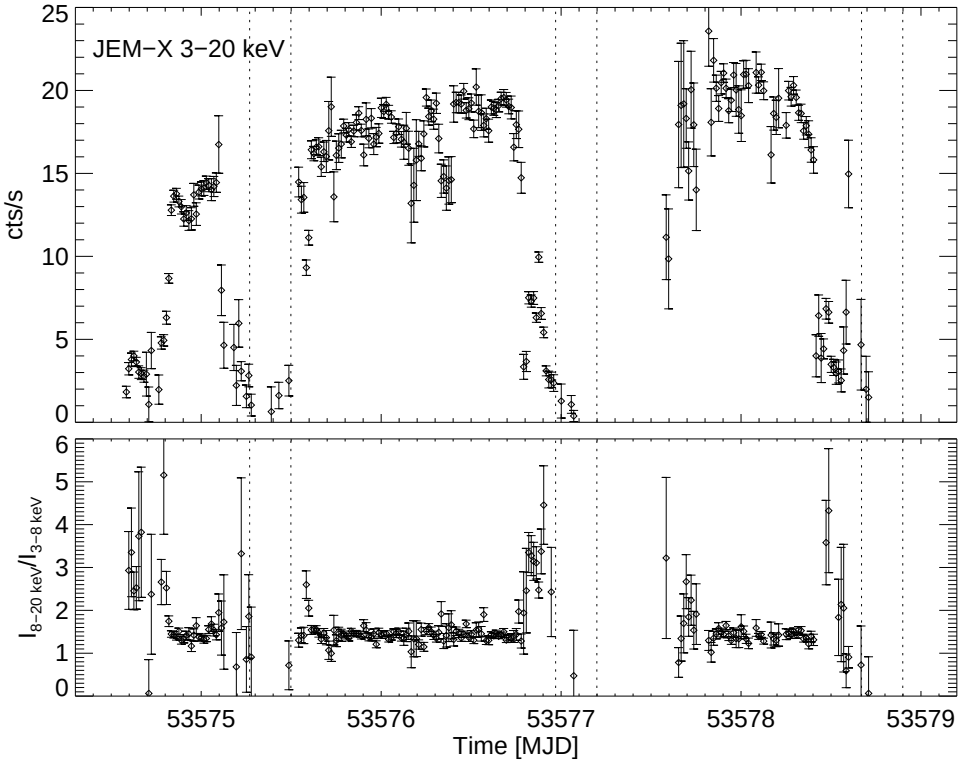

Figure 5.10 The *JEM-X* 3–20 keV light curve *(top panel)* and the ratio of count rates in the harder (8–20 keV) and softer (3–8 keV) energy ranges as a function of time *(bottom panel)*.

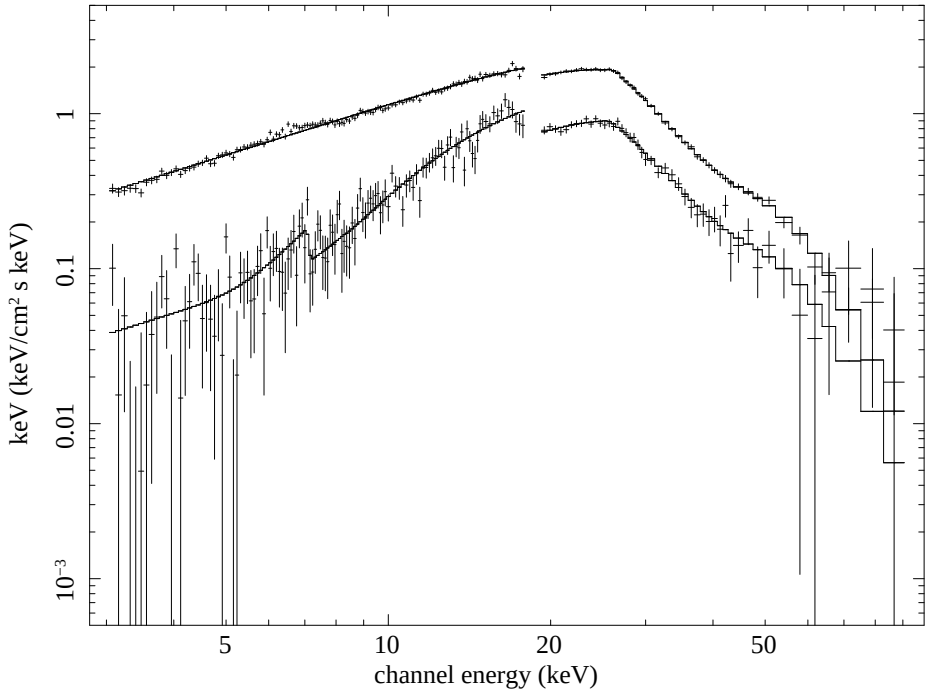

Figure 5.11 Examples of pulse-averaged spectra of Her X-1 from the dips (lower curve) and outside the dips (upper curve). The difference of the spectral shape at lower energies caused by photo-absorption inside the dips is clearly seen. The step-like feature at ~7 keV in the spectrum from the dips corresponds to the iron K-edge.

equivalent hydrogen column density. A larger value of B implies a larger degree of absorbed flux. From the fit of the spectrum from the dips we found $B = 0.24 \pm 0.03$ and $N_{\rm H} = (111^{+18}_{-19}) \times 10^{22}$ cm^{-2}. The best-fit parameters of the spectral continuum $I_{\rm cont}$ are consistent with those found from the spectrum outside the dips (Table 5.3). To compare this result with the spectrum outside the dips, the latter was also fit by the partial covering model. Both spectra (inside and outside the dips) are shown in Figure 5.11 For the spectrum outside the dips (the upper one) the $N_{\rm H}$ parameter was found to be consistent with zero and the B factor, consequently, was not restricted. We conclude therefore, that the X-ray data of Her X-1 during the dips are consistent with the partial absorption by the outer parts of the accretion disk and/or by the accretion stream (see also Section 8.1.7).

5.4.3 Pulse-phase-resolved spectra

It is well known that the X-ray spectrum of Her X-1 varies with 1.24 s pulse phase (see Section 3.2.4). So, we have performed a separate analysis of the spectra accumulated in different pulse phase intervals. Figure 5.12 shows an example of pulse resolved spectra of the source. Variability of the continuum and the cyclotron line is clearly seen.

Since the shape of the pulse profile is changing significantly from the beginning of the main-on (revolutions 339, 340) to its the end (revolution 341), we analyzed the data from these two intervals separately. The phase binning in each case was chosen to provide a similar statistics of

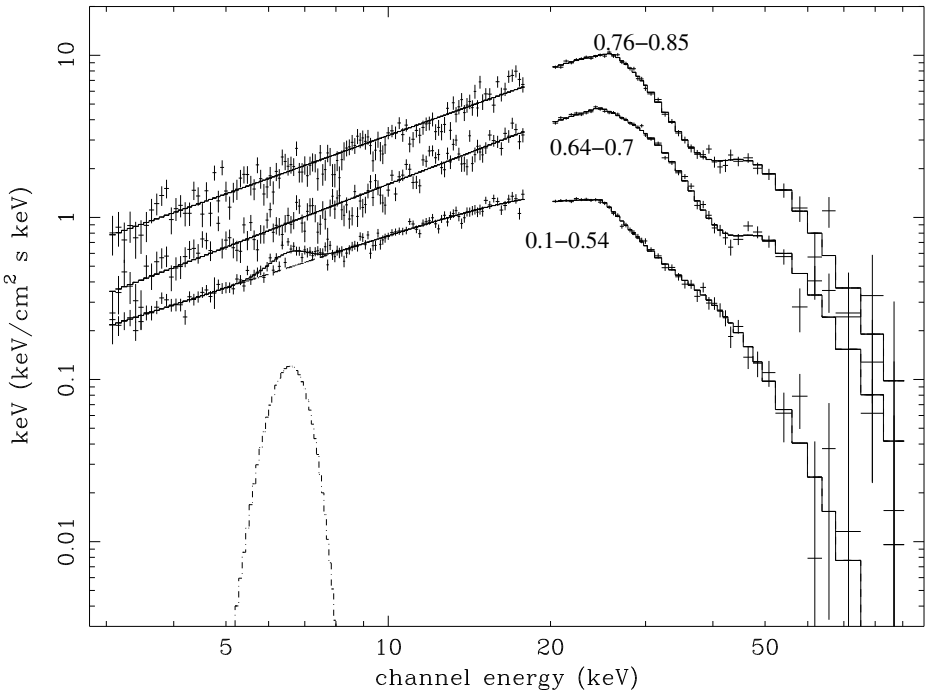

Figure 5.12 Examples of pulse resolved X-ray spectra of Her X-1 during revolutions 339 and 340. Phase intervals are indicated (the pulse phase zero is the same as in Figure 5.5).

the spectrum in each bin. The phase zero is the same as in Figure 5.5. The X-ray spectrum from each phase bin was fitted with the spectral model described in Section 5.4.1. Figures 5.13 and 5.14 show the best-fit spectral parameters as functions of the pulse phase for revolutions 339 and 340 *(left)* and the revolution 341 *(right)*. Vertical error bars correspond to 1σ(68%)-uncertainties. The dotted line shows the corresponding pulse profile. The spectral parameters in different pulse phase bins are also listed in Table 5.4. Since no *JEM-X* data for the revolution 341 are available the power law photon index Γ could not be restricted by the fit in this case. The iron line at ∼6.5 keV was detected only in the phase bin 1–0.54 corresponding to the off-pulse interval. The data from other phase intervals do not require inclusion of the line in the spectral model to obtain a good fit. For the data corresponding to revolutions 339 and 340 it is seen that all continuum and the cyclotron line parameters are highly variable with the pulse phase. For the revolution 341 the picture is not so clear due to the absence of the low-energy ($\lesssim$ 20 keV) part of the spectrum. Also the total exposure time and the average flux of the source in this interval are smaller than those during revolutions 339 and 340. The changing of the spectral parameters with the pulse phase is discussed in Section 8.1.8

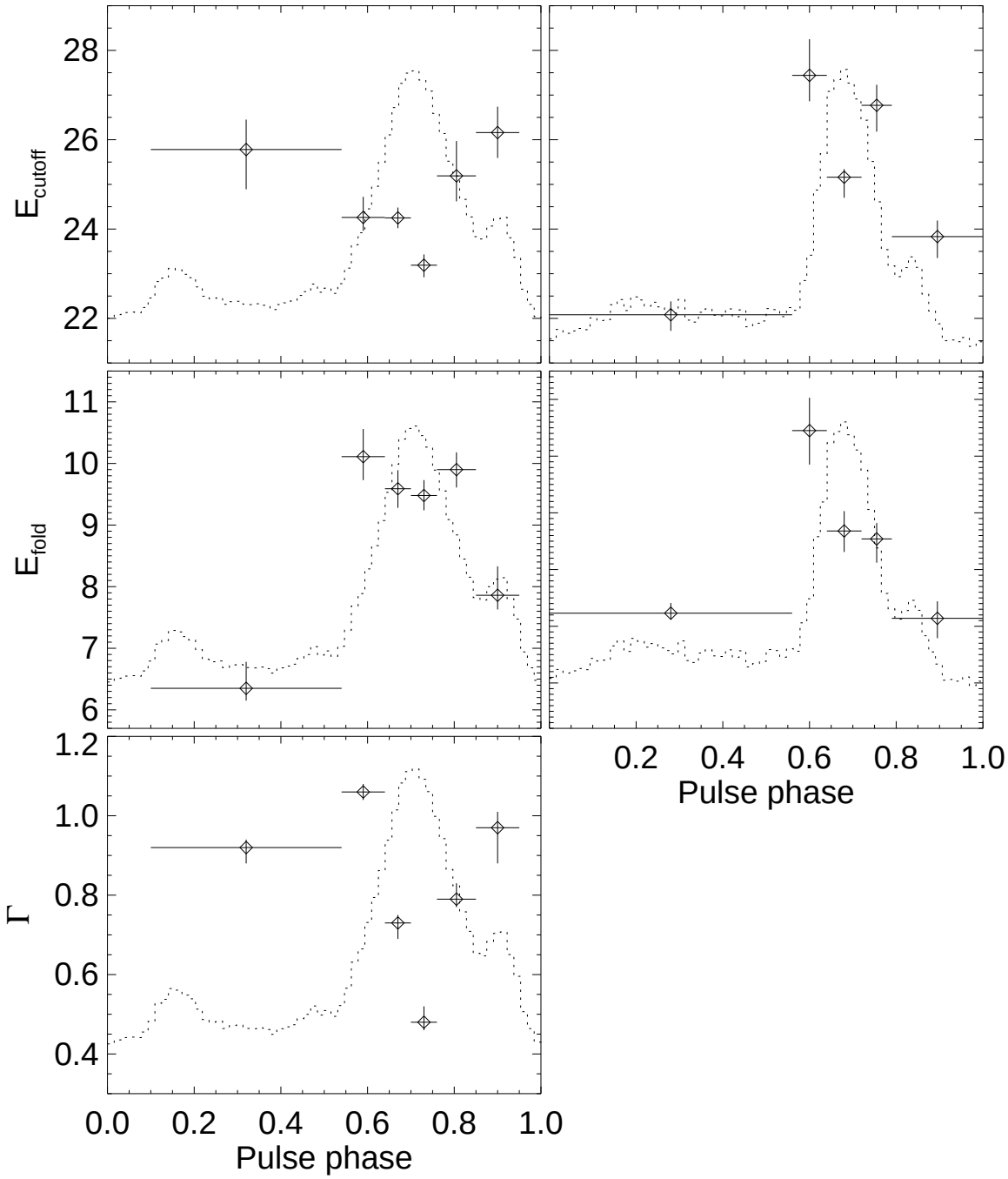

Figure 5.13 Best-fit spectral continuum parameters as functions of the pulse phase for revolutions 339 and 340 *(left)* and the revolution 341 *(right)*. The dotted curve shows the corresponding pulse profile. Vertical error bars correspond to 1σ(68%)-uncertainties.

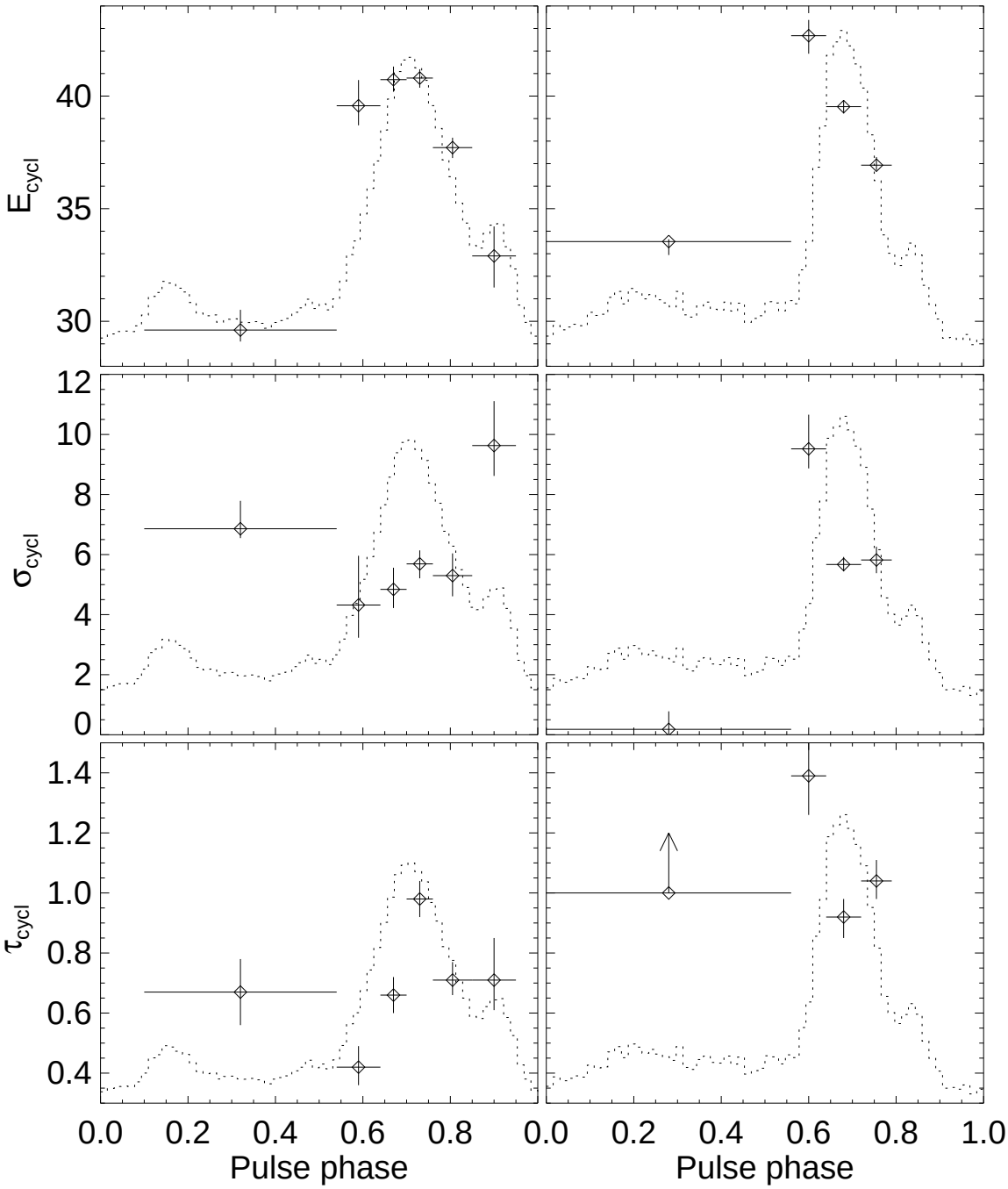

Figure 5.14 The same as in Figure 5.13 but for the cyclotron line parameters (left: revolutions 339 and 340; right: revolution 341).

Table 5.4 Best fit spectral parameters of Her X-1 in different pulse phase intervals. 1σ(68%)-uncertainties ($\chi^2_{\rm min}$ + 1) for one parameter of interest are shown.

Phase bin	Γ	$E_{\rm cutoff}$	$E_{\rm fold}$	$E_{\rm cycl}$	$\sigma_{\rm cycl}$	$\tau_{\rm cycl}$
Revs. 339 and 340						
0.10–0.54	$0.92^{+0.02}_{-0.04}$	$25.8^{+0.7}_{-0.9}$	$6.35^{+0.43}_{-0.20}$	$29.6^{+0.9}_{-0.5}$	$6.86^{+0.93}_{-0.31}$	$0.67^{+0.11}_{-0.11}$
0.54–0.64	$1.06^{+0.02}_{-0.02}$	$24.3^{+0.5}_{-0.3}$	$10.11^{+0.45}_{-0.38}$	$39.6^{+1.1}_{-0.9}$	$4.32^{+1.64}_{-1.09}$	$0.42^{+0.07}_{-0.06}$
0.64–0.70	$0.73^{+0.02}_{-0.04}$	$24.3^{+0.2}_{-0.2}$	$9.59^{+0.30}_{-0.31}$	$40.7^{+0.6}_{-0.5}$	$4.84^{+0.72}_{-0.62}$	$0.66^{+0.06}_{-0.06}$
0.70–0.76	$0.48^{+0.04}_{-0.02}$	$23.2^{+0.2}_{-0.3}$	$9.48^{+0.25}_{-0.24}$	$40.8^{+0.4}_{-0.4}$	$5.69^{+0.45}_{-0.48}$	$0.98^{+0.06}_{-0.06}$
0.76–0.85	$0.79^{+0.04}_{-0.02}$	$25.2^{+0.8}_{-0.6}$	$9.90^{+0.28}_{-0.29}$	$37.7^{+0.4}_{-0.5}$	$5.30^{+0.74}_{-0.69}$	$0.71^{+0.06}_{-0.05}$
0.85–0.95	$0.97^{+0.04}_{-0.09}$	$26.2^{+0.6}_{-0.6}$	$7.86^{+0.47}_{-0.23}$	$32.9^{+1.3}_{-1.4}$	$9.63^{+1.48}_{-1.01}$	$0.71^{+0.14}_{-0.10}$
Rev. 341						
0.00–0.56	—	$22.1^{+0.3}_{-0.4}$	$8.23^{+0.18}_{-0.11}$	$33.5^{+0.1}_{-0.6}$	$0.18^{+0.60}_{-0.17}$	≥ 1.0
0.56–0.64	—	$27.4^{+0.8}_{-0.6}$	$11.45^{+0.58}_{-0.60}$	$42.7^{+0.7}_{-0.8}$	$9.52^{+1.14}_{-0.65}$	$1.39^{+0.13}_{-0.13}$
0.64–0.72	—	$25.2^{+0.2}_{-0.5}$	$9.68^{+0.35}_{-0.37}$	$39.5^{+0.3}_{-0.3}$	$5.67^{+0.25}_{-0.23}$	$0.92^{+0.06}_{-0.07}$
0.72–0.79	—	$26.8^{+0.5}_{-0.6}$	$9.54^{+0.28}_{-0.42}$	$36.9^{+0.4}_{-0.2}$	$5.82^{+0.44}_{-0.44}$	$1.04^{+0.07}_{-0.06}$
0.79–1.00	—	$23.8^{+0.4}_{-0.5}$	$8.14^{+0.30}_{-0.35}$	—	—	—

Chapter 6

EXO 2030+375: Be X-ray binary

6.1 System description

Be/X-ray binaries are the most common type of accreting X-ray pulsar systems. They consist of a pulsar and a Be (or Oe) star, a main-sequence star of spectral type B (or O) that shows Balmer emission lines (see e.g. Slettebak 1988, for a review). The line emission is believed to be associated with an equatorial outflow of material expelled from the rapidly rotating Be star that probably forms a quasi-Keplerian disk its equator the Be star (Hanuschik 1996; Quirrenbach et al. 1997). If the disk reaches a radius comparable to the periastron separation, then disk gas accreted by the neutron star can power a significant (and usually transient) X-ray source. Be/X-ray binaries typically show two types of outburst behavior:

(1) Normal (or type I) outbursts. They are characterized by relatively low X-ray luminosities $L_{\rm X} \sim 10^{36}$–10^{37} erg s^{-1} and low spin-up rates (if any), and reccurence at the orbital period (or its multiples). Such outbursts last for days to weeks and are associated with the periastron passages of the neutron star.

(2) Giant (or type II) outbursts. They are characterized by higher X-ray luminosities $L_{\rm X} \gtrsim 10^{37}$ erg s^{-1} and high spin-up rates. Such outbursts occur irregularly, they last several weeks and are not correlated with any particular orbital phase. The typical recurrence time is of the order of several years. Giant outbursts are thought to be due to a dramatic expansion of the disk surrounding the Be star, leading to the formation of an accretion disk around the compact object.

The number of known Be/X-ray binaries is growing fast and, due to the transient nature of their emission, it is likely to continue its fast growth in the future. At present, there are no doubts, that such systems dominate the population of the massive X-ray binaries. Comprehensive reviews of the properties of Be/X-ray systems can be found e.g. in Coe (2000) and Ziolkowski (2002).

The transient accreting X-ray pulsar EXO 2030+375 is one of the best studied members of the described class of X-ray binary systems. It was discovered with the *EXOSAT* mission during a giant outburst in 1985 (Parmar et al. 1989b). The optical companion of the pulsar is a B0 Ve star identified by optical and infrared observations of the *EXOSAT* error circle (Motch & Janot-Pacheco 1987; Janot-Pacheco et al. 1988; Coe et al. 1988). The orbital period and eccentricity of the system are ~ 46 d and ~ 0.42, respectively (Wilson et al. 2002). The period of X-ray pulsations is ~ 42 s. There were two giant outbursts in the history of observations of EXO 2030+375. During the first one in 1985 (when the source was discovered) the X-ray luminosity of the source reached a value of

$L_{1-20\ \mathrm{keV}} \sim 2{\times}10^{38}$ erg s^{-1} (assuming a distance of 7.1 kpc Wilson et al. (2002)). The spin frequency of the pulsar changed dramatically, with a spin-up time scale $-P/\dot{P} \approx 30$ yr indicating the formation of an accretion disk around the neutron star. After the outburst the source was nearly continuously monitored by the Burst and Transient Source Experiment (*BATSE*) on the Compton Gamma Ray Observatory (*CGRO*) and later by the All Sky Monitor (*ASM*) on the Rossi X-ray Timing Explorer (*RXTE*, see Section 4.1). The second giant outburst took place in June–September 2006 (Corbet & Levine 2006; Krimm et al. 2006; McCollough et al. 2006) and was again accompanied by a strong spin-up of the neutron star. The X-ray luminosity at the maximum of the outburst was slightly lower than that during the 1985 giant outburst: $L_{1-20\ \mathrm{keV}} \sim 1.2 \times 10^{38}\,\mathrm{erg\,s^{-1}}$ (Wilson & Finger 2006). During the 2006 giant outburst the source was observed as a Target of Opportunity by the *INTEGRAL* and *Swift* satellites (see Section 5.1 for the *INTEGRAL* and Sect 7.1 for the *Swift* missions descriptions). We performed the analysis of these observations. The results are presented in Klochkov et al. (2007) and described in the next Chapter.

6.2 X-ray and optical monitoring

As mentioned above, since the discovery EXO 2030+375 was a subject of a comprehensive multiwavelength monitoring campaign. The 1985 giant outburst and the subsequent normal outburst were recorded by *EXOSAT* which provided detailed timing and spectral information (see Parmar et al. 1989b). The most extensive X-ray observations of the source between the two giant outbursts were made with the Large Area Detectors (*LAD*s) of *BATSE* onboard *CGRO*. From its launch in 1991 April until *CGRO* was deorbited in 2000 June, *BATSE* provided nearly continuous coverage of EXO 2030+375 providing the X-ray flux and pulse period information. Starting from 1996 March normal outbursts of the source were regularly detected with the *ASM* onboard *RXTE*. Apart from the long-term monitoring there were several pointed observations of the system performed by *RXTE*, *INTEGRAL*, and *Swift* which provided detailed information about the X-ray properties of the source, such as X-ray spectrum and energy-resolved pulse profiles (also during the second giant outburst in 2006, see the next Chapter). Soon after its discovery EXO 2030+375 was incorporated into the Southampton/Valencia Universities long-term monitoring campaign of Be/X-ray binaries (Coe et al. 1993; Reig et al. 1997) providing a large amount of optical and infrared data on the normal companion of the source.

Below we briefly describe the main results of the X-ray and optical observations of EXO 2030+375 available by today.

6.2.1 Pulse period and X-ray flux history

Since April 1991 (launch of *CGRO*) normal outbursts of EXO 2030+375 were detected at most periastron passages and continue to be detected with the *ASM RXTE* and *INTEGRAL*. The typical peak luminosity of these outbursts is $0.3 \times 10^{37} \leq L_{\mathrm{X}} \leq 3 \times 10^{37}$ erg s^{-1}. Figure 6.1 shows the light curve of the source obtained with the *ASM RXTE*. The dotted vertical lines mark periastron passages of the source. One can see that the maximum luminosity of normal outbursts varies by a factor of several, probably reflecting changes in the Be disk density. The giant outbursts are not shown in the picture. Their luminosity is an order of magnitude higher than that of normal outbursts (see above).

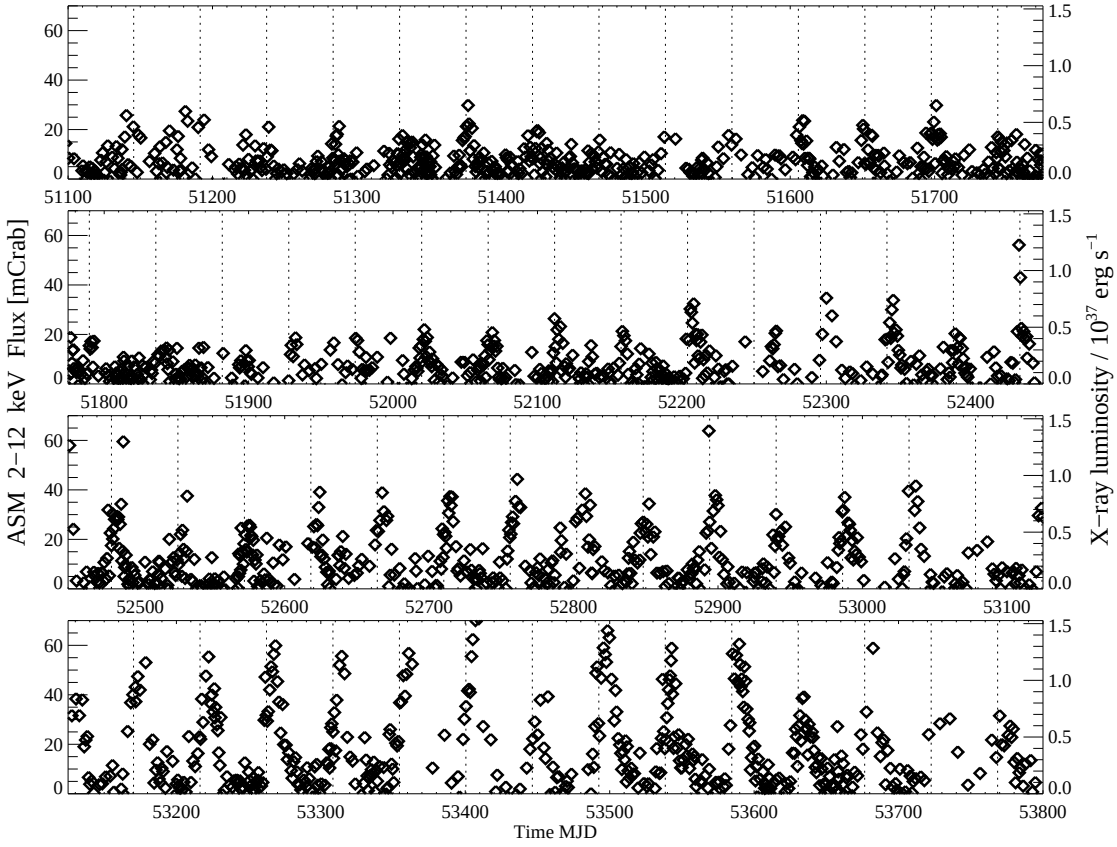

Figure 6.1 *ASM RXTE* light curve of EXO 2030+375. The dotted vertical lines denote predicted time of periastron passages. The right Y-axis shows the 2–20 keV X-ray luminosity assuming the distance of 7.1 kpc (Wilson et al. 2005).

The intrinsic spin period of EXO 2030+375 changed dramatically during the 1985 giant outburst, with a characteristic spin-up timescale $-P/\dot{P} \sim 30 - 40$ yr (Parmar et al. 1989b). We found a similar spin-up rate during the 2006 giant outburst of the source (see the next Chapter and Klochkov et al. 2007). Between the giant outbursts, during most of the normal outbursts of the system the pulse period was measured with *BATSE*. There were also several pointed observations made with *RXTE* which also provided pulse period information (a compilation of these data can be found in Wilson et al. 2002, 2005). The historical pulse frequency behavior of EXO 2030+375 is shown in Figure 6.2. Strong spin-up during the 1985 and 2006 giant outbursts are clearly seen. The large triangles correspond to our pulse frequency measurements. The other data points are taken from Wilson et al. (2002, 2005) The pulse period remained roughly constant for about a year after the beginning of the monitoring by *BATSE* in 1991, followed by 2 years of relatively slow spin-up and 6 years of slow spin-down. After 2002 a transition to a global spin-up along with an overall brightening of the normal outbursts was reported by Wilson et al. (2005) (see also Fig. 6.1).

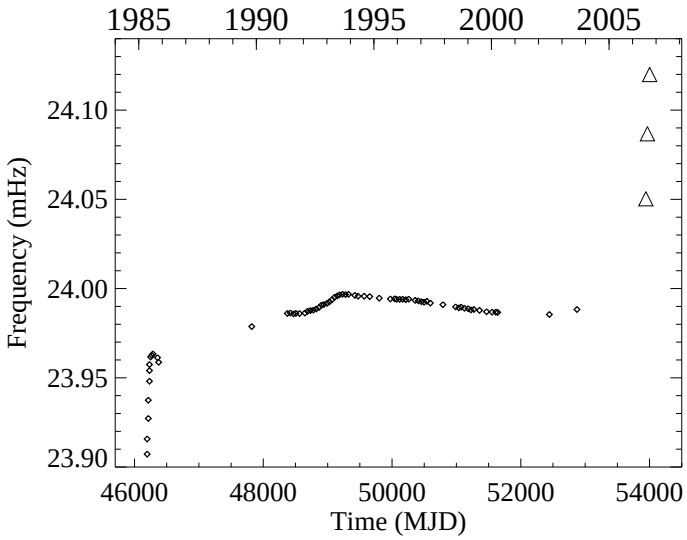

Figure 6.2 Spin frequency of EXO 2030+375. The large triangles correspond to our pulse frequency measurements during the 2006 giant outburst. Other data points are taken from Wilson et al. (2002, 2005) The uncertainties of measurements and the duration of each observation are smaller than the size of symbols in the plot.

6.2.2 Type I X-ray outbursts

As mentioned before, the normal (type II) outbursts of EXO 2030+375 were detected at most periastron passages of the neutron star. However, the exact orbital phase of the peak of the outbursts varies by several days. Figure 6.3 shows the orbital phase of the outbursts versus time as presented by Wilson et al. (2005). The dashed lines indicate the intervals of orbital phase when pulsations were detected with *BATSE*. One can see that the outbursts prior to MJD 50000 (1995 October) peaked at a very regular orbital phase of about 6 days after periastron passage. The outburst just after MJD 50000 peaked at a much earlier orbital phase, 4 days before periastron passage, and then gradually shifted to earlier orbital phases.

The shape of the outbursts light curves is also non-trivial. An initial sharp spike before the main outburst and a possible second spike during the decay of the outburst were reported by Camero Arranz et al. (2005) during the normal outburst observed with *INTEGRAL* in December 2002 (Fig. 6.4). They also argued that evidences of the spikes are also present in the *BATSE* and *RXTE* light curves. A sharp initial spike was also observed during a normal outburst of another Be/X-ray binary, A 0535+262 (Caballero et al. 2007). Thus, such sharp spikes might be a common feature in this type of binary systems.

6.2.3 Optical/IR observations

Optical/IR observation of EXO 2030+375 were obtained as part of the Southampton-Valencia monitoring campaign, using mainly the 1.5-m Carlos Sánchez Telescope (Teide observatory, Tenerife). Details can be found in Reig et al. (1998). The goal of these observations was to monitor the magnitude of the optical companion in the infrared bands (*JHK*) and the equivalent width of H_α line in the optical spectrum of the source. It is known that these characteristics may serve as indicators of the size and density of the circumstellar disk around the Be companion (see e.g. Negueruela et al. 2001; Miroshnichenko et al. 2001).

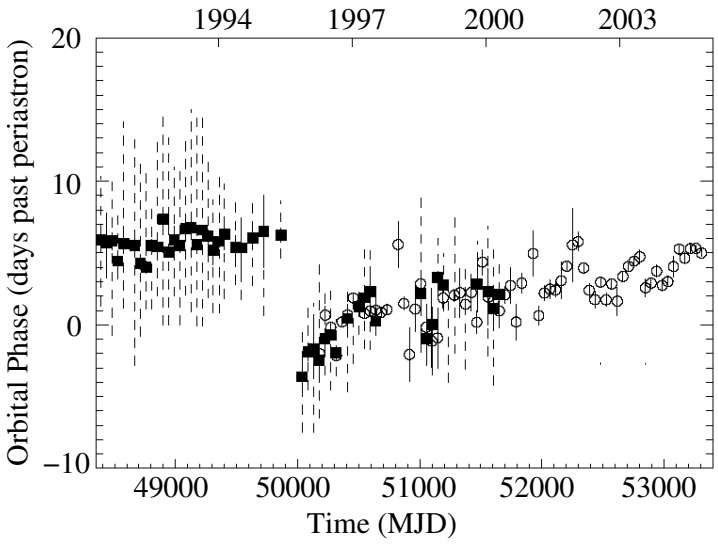

Figure 6.3 Orbital phase of EXO 2030+375 outburst peaks versus time taken from (Wilson et al. 2005). Filled squares indicate the times of peaks measured with *BATSE*. Open circles indicate the times of outburst peaks estimated from the *ASM RXTE*.

A comparison of the Optical/IR observations with X-ray measurements suggests a relationship between the Optical/IR behavior and the X-ray activity. At approximately the same time when the peak flux of the normal outburst dropped dramatically in the *BATSE* data, the K-band infrared flux from the companion also dropped, indicating a decrease in density of the Be star's disk. Brightening of the X-ray outbursts as observed by the *ASM RXTE* appeared to approximately coincide with the brightening of the Be disk, indicating that the disk density had again increased. Thus, on the long term the Be disk density appears to drive the X-ray flux of the normal outbursts.

6.2.4 X-ray pulse profiles

First X-ray pulse profiles of EXO 2030+375 were obtained with *EXOSAT* ($\lesssim$ 20 keV) during the 1985 giant outburst (Parmar et al. 1989b). The shape of the profiles was found to depend strongly on luminosity (Fig. 6.5). At higher luminosities the pulse profile consisted of a smooth asymmetric main pulse separated by $\sim 180^\circ$ in phase from a small interpulse. As the luminosity decreased by a factor of ~100 the relative strength of the two pulses reversed, with the interpulse becoming the dominant pulse. 2–10 keV pulse profiles were observed with the *PCA RXTE* during a normal outburst of the source in July 1996 (Reig & Coe 1998). The profiles were consistent with the *EXOSAT* profiles observed at low luminosity. Reig & Coe (1998) explored the energy dependence of the pulse profile but their analysis was restricted by the low statistics above ~20 keV.

The first high energy (> 20 keV) pulse profiles of EXO 2030+375 during a giant outburst were obtained with *INTEGRAL* during the 2006 outburst. The analysis of these data is presented in the next Chapter.

6.2.5 X-ray spectrum

The X-ray spectrum of EXO 2030+375 during the 1985 giant outburst observed by *EXOSAT* (2–25 keV) was similar to that of other accreting pulsars: it can be represented by a power law modified at lower energies by significant absorption and at higher energies by an exponential

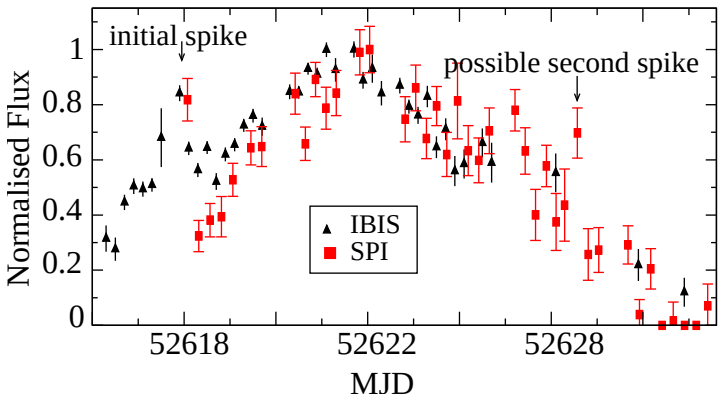

Figure 6.4 The *INTEGRAL* light curve of EXO 2030+375 during a normal outburst seen in December 2003. The unusual features are marked.

cutoff (Reynolds et al. 1993). An iron emission line at ~6.5 keV was observed. The spectrum showed a significant evolution during the decay of the outburst. As the luminosity decreased by a factor of ~100, the X-ray spectrum became harder with the photon index decreasing from 1.8 to 1.3. In addition, the high energy cutoff decreased from 20 to 10 keV.

A normal outburst of EXO 2030+375 was observed in 1996 July with *RXTE*. The spectrum was shown to agree with that from *EXOSAT* when an extrapolation at low luminosities is realized (Reig & Coe 1999). A black body component (with $kT \sim 1.2$ keV and the emission radius of ~1 km) was observed at the low-energy part of the spectrum. The authors for the first time explored the hard X-ray spectrum (17–65 keV) of EXO 2030+375 obtained with *HEXTE* (high-energy detector onboard *RXTE*), although the data were scarce. They found an evidence of a possible cyclotron feature at ~36 keV. The first broad band spectrum (3–300 keV) of the source with good statistics was obtained with *INTEGRAL* during a normal outburst in December 2002 (Camero Arranz et al. 2005) who found a hard X-ray component which can be described by a nonattenuated power law with the photon index ~2. The authors also added a black body component with $kT \sim 8$ keV to describe the low-energy part of the spectrum.

6.3 The model and open questions

In Section 6.1 we described the main physical properties of EXO 2030+357. Below we will try to explain how these properties cause the observed behavior of the system according to the presently accepted model. We will also outline the main problems in understanding of the source's physics, mainly focusing on those affected by our work.

As mentioned above, the key feature of Be/X-ray binaries is the circumstellar gaseous disk (Be disk) around the optical companion. According to the currently accepted model (see e.g. Lee et al. 1991; Porter 1999; Okazaki 2001) the viscosity in such a disk transports material outward, so that it moves in quasi-Keplerian velocity with low radial velocities. It was shown (Negueruela et al. 2001) that such a disk cannot reach a steady state due to tidal and resonant interaction with the neutron star, and it is truncated at some radial distance. According to the modeling of Okazaki & Negueruela (2001), the Be disk in EXO 2030+375 is likely truncated at the 4:1 resonance radius (i.e. where the orbital period of the matter in the disk is four times shorter than the orbital period of the binary). This is close to the radius where matter can be captured by the neutron star close to the

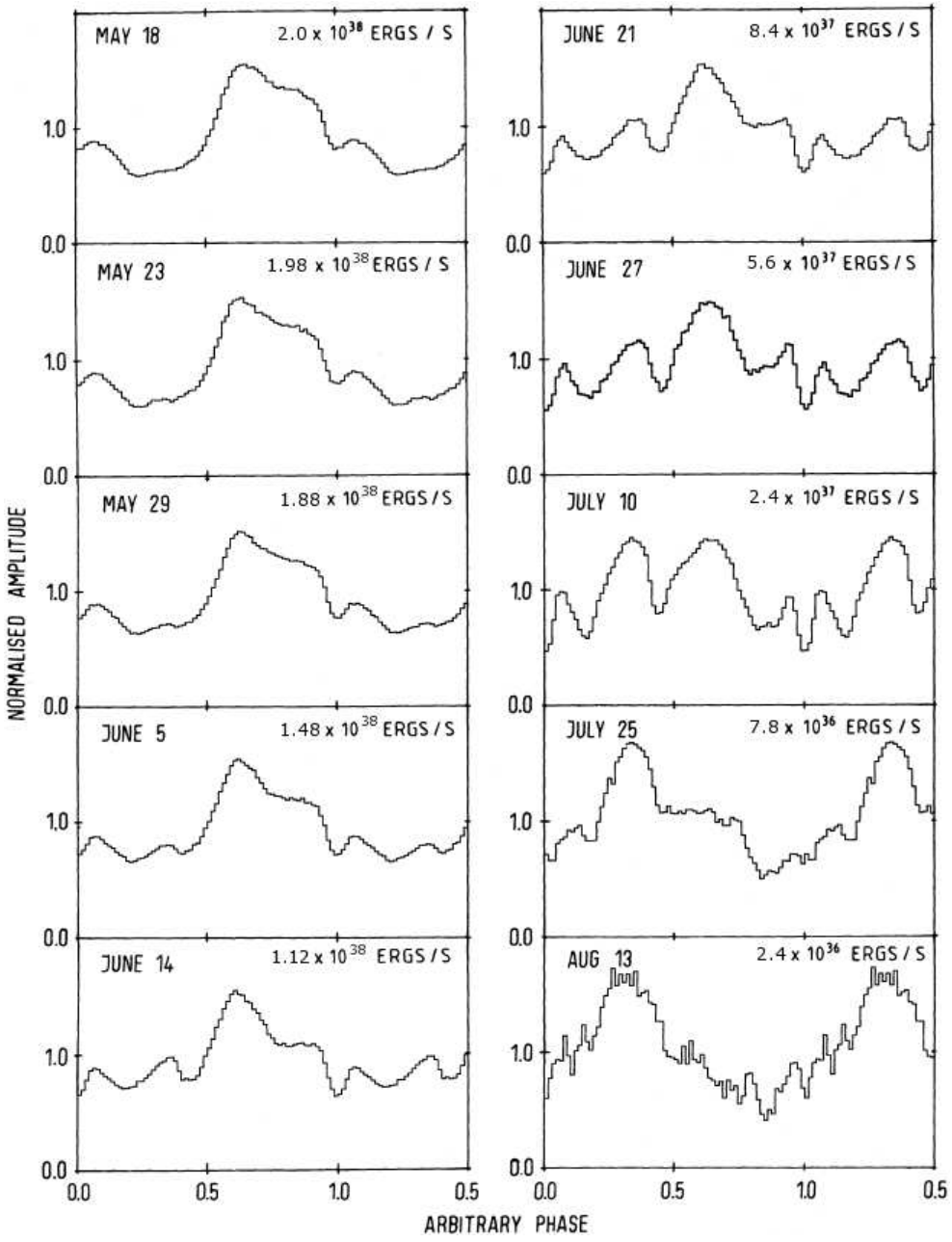

Figure 6.5 1–10 keV *EXOSAT* pulse profiles of EXO 2030+375 showing the evolution of the shape during the 1985 giant outburst. The picture is taken from Parmar et al. (1989b). The indicated 1–20 keV luminosities are corrected assuming the updated distance of 7.1 kpc (Wilson et al. 2002) with respect to those, provided by Parmar et al. (1989b) who used 5 kpc.

periastron passage and form a transient accretion disk which provides a reasonable explanation of normal outbursts.

A possible explanation of the orbital phasing of the normal outbursts (see Section 6.2.2)

is a density perturbation (global one-armed oscillation) in the Be disk. Evidence of these density perturbations is seen in the H_α line profiles for several Be/X-ray binaries (see e.g. Negueruela et al. 2001; Okazaki & Negueruela 2001). If the pulsar interacts with a region of the disk affected by the perturbation, more material would be available for accretion. Slow propagation of the perturbation through the disk possibly causes a shift in outburst phase. Also the fact that the Be disk is not necessarily lies in the orbital plane (as it is assumed in Okazaki & Negueruela 2001) may lead to an additional shift of the outburst's phase with respect to the periastron.

Since many flux and pulse period measurements are available for EXO 2030+375 (Section 6.2.1), one can study the correlation between the flux and spin-up rate predicted by the simple accretion theory (Pringle & Rees 1972). Such a correlation is expected if an accretion disk forms around the pulsar. In the giant outburst observed with *EXOSAT*, such a correlation was clearly seen (Parmar et al. 1989b; Reynolds et al. 1996). During normal outbursts the correlation (albeit not so clear) was also reported by Wilson et al. (2002), based on *BATSE* observations. The measured correlation is inconsistent with the power law index of 6/7 predicted by the simple accretion theory. In order to discriminate between more complicated accretion models, additional measurements of the pulse period at various luminosity levels are needed.

As mentioned in Section 6.2.3, optical/IR observations provide information about the density of the Be disk. From the observations it follows that the Be disk was fairly stable and roughly constant in density from near the end of the initial giant outburst until MJD 49,000 (1993 January). The pulsar was spinning up for most of this period indicating disk accretion. Then the density of the Be disk began to decline. Since the Be disk was becoming less dense, the reservoir of material available to the pulsar near periastron passage was slowly reduced. The X-ray flux observed by *BATSE* responded to the lower density Be disk and dropped dramatically. After MJD 49400 (1994 February) the pulsar begun to spin down. In 2002–2003 the infrared data indicated that the Be disk intensity had again increased (Wilson et al. 2002). This was also accompanied by the brightening of normal outbursts. This increase probably led to the 2006 giant outburst caused by a dramatic expansion of the Be disk. The optical/IR observations are, therefore, in agreement with the described model.

The strong luminosity dependence of the pulse profile of the source observed during the 1985 outburst (the almost 180° switch in phase of the main pulse, see Section 6.2.4) is suggestive of a major change in the beaming direction in the pulsar's surface. Parmar et al. (1989b) suggested that the basic beaming mechanism switches from a fan to a pencil configuration as the luminosity decreases. They noted, however, that their simple model does not provide formally acceptable fits and is only used to illustrate the overall trends. Another possibility to explain the changes in the pulse profile with the luminosity is that the pulsar's magnetic field is more complex than a simple dipole and that a different magnetic pole becomes active as the luminosity changes. More sophisticated modeling of the pulse profiles taking into account their energy dependence is necessary to reveal the geometry and physics of the radiation at the neutron star's surface.

In Section 6.2.5 we mentioned that the X-ray spectral continuum of EXO 2030+375 is similar to those of other accreting pulsars (see also Section 2.4.3). Since the beginning of *RXTE* and *INTEGRAL* operation, broad band spectra (including the high-energy part, $\gtrsim$20 keV) are available for the source. Some unusual features in the spectrum are found (e.g. a black body component with the unusually high temperature $kT \sim 8$ keV, see also the next Chapter). At the moment there is no generally accepted model for the broad band spectrum of EXO 2030+375. There is also no clear interpretation of the luminosity dependence of the continuum parameters found by (Reynolds et al.

1993). The question of the cyclotron line in the spectrum of the source is not clear. So, the open questions related to EXO 2030+375 addressed in this work can be summarized as follows:

1. Study of the $L_X - \dot{P}_{pulse}$ relation. Which accretion mechanism is at work?
2. Origin of the pulse profiles and their dependence on the energy and luminosity. Pencil or fan beam configuration?
3. Origin of the broad band X-ray spectrum of the source.
4. Possible cyclotron feature in the X-ray spectrum of the source.

Chapter 7

INTEGRAL and *Swift* observations of EXO 2030+375

In June–September 2006 EXO 2030+375 entered into a giant (type II) outburst (Corbet & Levine 2006; Krimm et al. 2006; McCollough et al. 2006). This is the second giant outburst since the discovery of the source. The X-ray luminosity at the maximum of the outburst reached a value of $L_{1-20\ \mathrm{keV}} \sim 1.2 \times 10^{38}\,\mathrm{erg\,s^{-1}}$ (Wilson & Finger 2006). Based on the *INTEGRAL* and *Swift* data, we investigated the pulse period and the spin-up rate of the source (Section 7.3.1) and constructed X-ray pulse profiles for different energy ranges and time intervals (Section 7.3.2). To characterize the broad-band spectral behavior we performed the spectral analysis of pulse-phase averaged spectra of the source (Section 7.4).

7.1 *Swift* satellite: mission overview

Swift is a first-of-its-kind multi-wavelength observatory dedicated to the study of gamma-ray bursts (GRBs).[1] The mission was launched into a low-Earth orbit on November 20, 2004. The hardware was developed by an international team from the United States, the United Kingdom, and Italy, with additional scientific involvement of France, Japan, Germany, Denmark, Spain, and South Africa. A comprehensive review can be found in Gehrels et al. (2004). The overall view of *Swift* is given at Fig 7.1. The main mission objectives for *Swift* are the following:

- Determine the origin of GRBs.
- Classify GRBs and search for new types.
- Use GRBs to study the early universe.
- Perform a hard X-ray survey of the sky **(10–30 times more sensitive than the HEAO A-4 survey).**

[1] Gamma-ray bursts are presumably the most powerful explosions in the Universe since the Big Bang. They are observed as brief (milliseconds to a few hundred seconds), but intense, flashes of gamma radiation, sometimes followed by longer and softer afterglows.

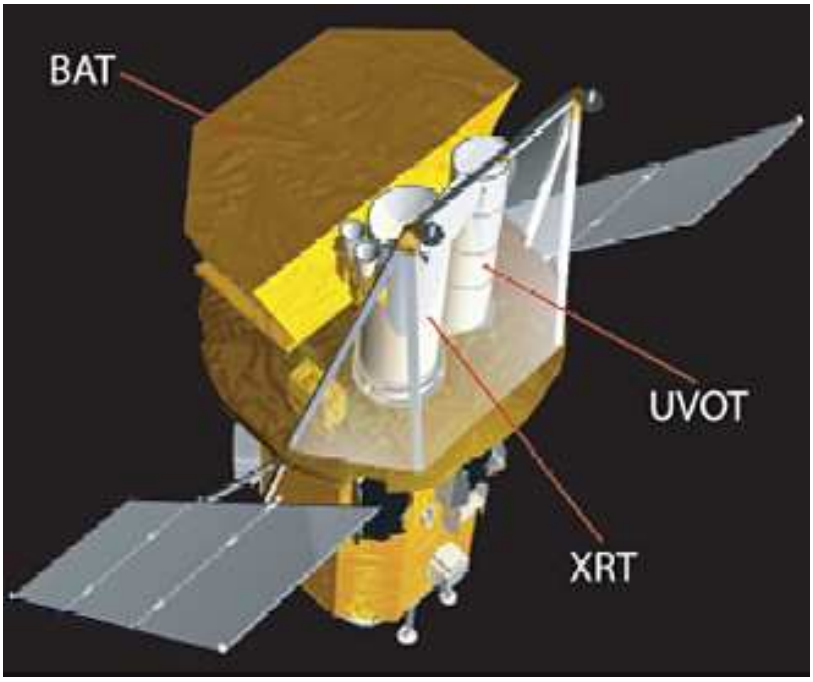

Figure 7.1 *Swift* satellite. *BAT* — Burst Alert Telescope (15–150 keV); *XRT* — X-ray Telescope (0.3–10 keV); *UVOT* — UV/Optical Telescope (170–650 nm).

The payload of *Swift* is comprised of three instruments: the *Burst Alert Telescope (BAT)* with large field-of-view (2 steradians) and 15–150 keV energy range; the *X-ray Telescope (XRT)*, providing high resolution images and spectra in the 0.3–10 keV energy range; and the *UV/Optical Telescope (UVOT)* that takes images and spectra in the optical band 170–650 nm.

Although the main focus of *Swift* are GRBs, the mission is also used to study other sources of X and gamma-rays, such as compact X-ray binaries. Observations of such sources can be triggered by some unusual event or behavior (for example, bright flares or outbursts). In this case the source can be observed as a *Target of Opportunity* (TOO).

Below we provide a brief description of the *BAT* and *XRT* instruments which were used for the observations of EXO 2030+375 analyzed in this work.

7.1.1 *BAT*

The Burst Alert Telescope (BAT) is a highly sensitive, large Field of View (FOV) instrument designed to provide critical GRB triggers and 4-arcmin positions. It is a coded aperture imaging instrument with a 1.4 steradian field-of-view (half coded). The energy range is 15–150 keV for imaging with a non-coded response up to 500 keV (see Barthelmy et al. 2005, for a review). The *BAT* has a two-dimensional coded aperture mask and a large area solid state detector array. Its coded aperture field-of-view always includes the *XRT* and *UVOT* fields-of-view. Table 7.1 summarizes the main instrument characteristics. The data from *BAT* can produce a sensitive hard X-ray

Table 7.1 *BAT* instrument parameters.

Property	Description
Aperture	Coded mask
Detecting Area	5200 cm^2
Detector	CdZnTe
Detector Operation	Photon counting
Field of View	1.4 sr (partially--coded)
Detection Elements	256 modules of 128 elements
Detector Size	4 x 4 x 2 mm
Telescope PSF	17 arcmin
Energy Range	15–150 keV
Sensitivity	**2 mCrab in 16 hours**

Table 7.2 *XRT* instrument parameters.

Property	Description
Focal Length	3.5 m
Effective Area	110 cm^2 at 1.5 keV
Telescope PSF	18 arcsec (HPD) at 1.5 keV
Detector	EEV CCD-22, 600 x 600 pixels
Detector Operation	Imaging, Timing, and Photon-counting
Detection Element	40 x 40 micron pixels
Pixel Scale	2.36 arcsec/pixel
Energy Range	0.2–10 keV
Sensitivity	2×10^{-14}erg cm^{-2} s^{-1} in 10^4 seconds

all-sky survey and X-ray transients monitor over the course of *Swift*'s two year mission.[2]

The *BAT* runs in two modes: (1) burst mode, which produces burst positions, and (2) survey mode, which produces hard X-ray survey data. In the survey mode the instrument collects count-rate data in 5-minute time bins for 80 energy intervals. When a burst occurs it switches into a photon-by-photon mode with a ring-buffer to save pre-burst information.

7.1.2 *XRT*

Swift's *XRT* is designed to measure the fluxes, spectra, and light curves of X-ray sources over a wide dynamic range covering more than 7 orders of magnitude in flux. The instrument parameters are summarized in Table 7.2. For a more detailed review see Burrows et al. (2005).

The instrument is designed as a grazing incidence Wolter 1 telescope with a 110 cm^2 effective area. A set of X-ray mirrors focuses X-rays onto a CCD which consists of an image area with 600 x 602 pixels (40 x 40 microns) and a storage region of 600 x 602 pixels (39 x 12 microns). The FWHM energy resolution of the CCDs decreases from ~190 eV at 10 keV to ~50 eV at 0.1 keV.

The *XRT* supports three readout modes to enable it to cover the dynamic range and rapid variability of X-ray sources (expected in case of GRB afterglows), and autonomously determines which readout mode to use. The *Imaging Mode* produces an integrated image of the sources in the field-of-view and does not permit spectroscopy. The *Timing Mode* sacrifices position information to achieve high time resolution and bright source spectroscopy through rapid CCD readouts. The *Photon-counting* Mode uses sub-array windows to permit full spectral and spatial information to be obtained for source fluxes ranging from the *XRT* sensitivity limit of 2×10^{-14} to 9×10^{-10}erg cm^{-2} s^{-1}.

[2]The data of the *BAT* Hard X-ray Transient Monitor are available at http://heasarc.gsfc.nasa.gov/docs/swift/results/transients/

Table 7.3 Summary of observations.

Obs.	Instrument	Obs.time (ks)	Mean MJD	Mean ASM flux (mCrab)
OBS1	ISGRI+JEM-X	62	53942.9	500
OBS2	ISGRI+JEM-X	140	53967.6	500
OBS2	XRT + BAT	6.3	53967.3	500
OBS3	XRT + BAT	6.4	54002.5	160

7.2 Observations and data reduction

7.2.1 Summary of observations

EXO 2030+375 was observed by *INTEGRAL* (see Section 5.1) on 27 July and 19–21 August 2006 and by *Swift* (see Section 7.1) on 19–20 August and 23–25 September 2006. For our analysis we used the data obtained with the instruments *IBIS/ISGRI* (20–300 keV, see Section 5.1.1) and *JEM-X* (3–30 keV, see Section 5.1.3) onboard *INTEGRAL* as well as *XRT* (0.2–10 keV, see Section 7.1.2) and *BAT* (15–150 keV, see Section 7.1.1) of *Swift.*

Table 7.3 contains the summary of the observations analyzed in this work. A part of the *ASM* light curve of the source including three normal outbursts and the 2006 giant outburst is shown in Figure 7.2. The observations analyzed in this work are marked by solid lines and consist of three sets of pointings. The first set was done by *INTEGRAL*. The second set contains simultaneous observations by *INTEGRAL* and *Swift.* The last set of observations was performed by *Swift.* These three sets will be referred to as OBS1, OBS2, and OBS3 throughout this Chapter. OBS1 and OBS2 observations were made when the source was at approximately the same luminosity level, before and after the maximum of the outburst. These observations cover a broad energy range from 0.2 to 200 keV. Data form OBS2 allowed to derive cross-calibration coefficients between the *INTEGRAL* and *Swift* instruments which were then used to compare the source X-ray luminosity in all three observations. OBS3 was made during the decay of the outburst when the luminosity of the source dropped by a factor of ~3. This observation contains only the low-energy part of the spectrum ($\lesssim$10 keV) since the *BAT* data ($\gtrsim$15 keV) have poor statistics.

7.2.2 *IBIS/ISGRI* and *JEM-X* data processing

For processing of the data taken with the *INTEGRAL* instruments *ISGRI* and *JEM-X* the Off-line Science Analysis (OSA, version 5.1) developed by the *Integral Science Data Center* was used (Courvoisier et al. 2003). The data reduction procedures in case of EXO 2030+375 are mostly the same as those used to analyze the Her X-1 *INTEGRAL* data (see Sections 5.2.2 and 5.2.4). Here we only point out two differences with respect to the Her X-1 data analysis.

1. Apart from EXO 2030+375, two other bright X-ray sources fell into the field of view of the *INTEGRAL* instruments during the observations: Cyg X-1 with the X-ray flux comparable to that of EXO 2030+375, and Cyg X-3 that was ~10 times fainter. All three sources were included in the extraction catalogs of *ISGRI* and *JEM-X* in order to account for their reciprocal flux contaminations.

2. In the case of EXO 2030+375 we did not perform the additional gain correction of the

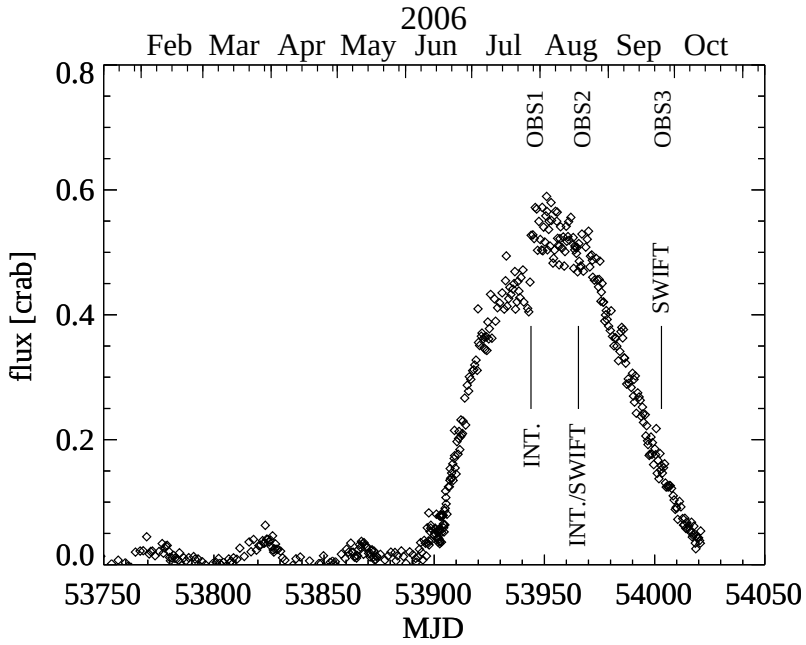

Figure 7.2 The *ASM* light curve of EXO 2030+375. The times of *INTEGRAL* (INT.) and *Swift* observations analyzed in this work are marked by solid lines.

photon energies which was applied in the Her X-1 data analysis. Since the precise measuring of the energy of spectral features is not the main goal of the present analysis (in contrast to Her X-1), additional systematic uncertainty of 1.5–2 keV in the position of lines/"bumps"/cutoff related to this does not affect our results significantly.

7.2.3 *BAT* data processing

Reduction of the *BAT* data was done with the standard *HEADAS* package (version 6.0.4) which contains all necessary routines and calibration data. The raw *BAT* data of EXO 2030+375 taken from the *Swift* archive[3] are accumulated in *survey mode* (see Section 7.1.1) and consist of so-called survey detector plane histograms (DPHs) – three-dimensional data cubes with 80 x 286 x 173 elements. The first dimension corresponds to the number of energy channels (80 for *BAT* surveys). The second and third dimensions indicate the geometric location of the detector in the *BAT* array plane. Each DPH contains data accumulated over ~300 sec. Therefore, no timing analysis is available with time resolution better than ~300 sec. The reconstruction technique involves cross-correlation (or matched filtering) of the detected counts with the mask aperture pattern for all possible locations on the sky (see Section 5.2.2). For light curve and spectral analysis of previously known sources, it is possible to bypass most of the reconstruction steps. We used *BAT* sky images to check the presence and significance of the source.

EXO 2030+375 was observed with *BAT* in OBS2 and OBS3 (see Table 7.3). It was found, however, that statistics of the data taken in OBS3 (during the decay of the outburst) is too low to obtain useful spectra. So, we used only the data from OBS2. The source spectra in the

[3]The archive is available at http://heasarc.gsfc.nasa.gov/cgi-bin/W3Browse/swift.pl

Table 7.4 Pulse period development. The uncertainties in parentheses (68%) refer to the last digit(s).

Obs.	MJD	P [s]	$-dP/dt$ [10^{-8} s/s]	Flux (3–10 keV) [10^{-9} erg cm^{-2} s^{-1}]
OBS1	53942.7714	41.57958(2)	2.93(12)	9.61(6)
OBS2	53967.4260	41.51706(5)	3.29(19)	10.41(4)
OBS3	54002.3877	41.45954(4)	0.67(10)	3.25(3)

range of 15–80 keV were produced with the *HEADAS* tool `batbinevt` from the DPHs using the known position of EXO 2030+375 in the sky. The corresponding detector response matrices were generated with `batdrmgen` also provided by *HEADAS*. Since the pulse period of EXO 2030+375 (~42 sec) is smaller than the typical accumulation time of DPHs (~300 sec), timing analysis of the *BAT* data is not possible.

7.2.4 *XRT* data processing

Reduction of the *XRT* data was also done with the standard *HEADAS* package. The observations of EXO 2030+375 were performed in *windowed timing mode*. This mode is obtained by compressing 10 rows in the serial register of the CCD into a single row, and then reading out only the central 200 columns. It covers the central 8 arcmin of the field of view and one-dimensional imaging is preserved. For our observations (OBS2 and OBS3) the *Swift* archive already contained processed events files which can be directly used to extract higher level products such as images, light curves and spectra.

X-ray spectra and light curves of the source were extracted from the events files using `XSELECT` provided by *HEADAS* package. For the spectral analysis the latest (version 8) response matrix (RMF) and the corresponding ancilliary response function (ARF) provided by the *XRT* team were used. The energy range for the spectra was chosen to be 3–10 keV as advised by the *XRT* team.

7.3 Timing analysis

For the timing analysis we translated all times to the solar system barycenter and corrected for orbital motion in the binary (the orbital ephemeris of Wilson et al. 2005 were used). For determining the pulse period and constructing pulse profiles of EXO 2030+375 the light curves with the time resolution of 0.3 sec extracted with `XSELECT` from the event files were used.

7.3.1 Pulse period behavior

The pulse periods and associated derivatives were determined for each of the three observation periods individually. The results are shown in Table 7.4. These values were found by employing initial epoch-folding and a subsequent phase connection analysis similar to that described in Section 4.2.1 using well defined pulse profiles from a sufficiently large number of pulses. Variation in pulse shape inside each observation is marginal and does not affect our method.

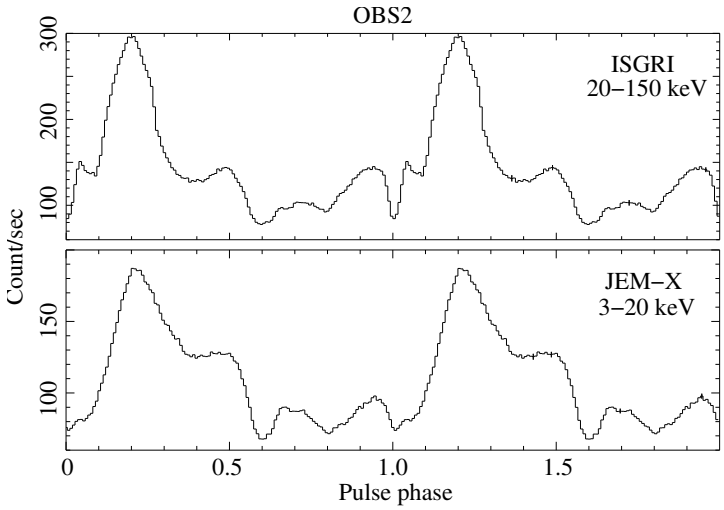

Figure 7.3 X-ray pulse profiles obtained with *ISGRI* (*top panel*) and *JEM-X* (*bottom panel*) during OBS2 (MJD∼ 53966), near the maximum of the outburst. Phase 0.0 was arbitrarily chosen to be defined by the dip-like feature before the main peak.

Figure 6.2 displays our points together with the historical pulse period development as presented by Wilson et al. (2002, 2005). The three data sets are consistent with a global solution (valid between MJD 53943 and MJD 54003) with the following parameters: P = 41.47268(6) s, $\dot{P} = -1.627(5)\times10^{-8}$ s/s and $\ddot{P} = 4.058(25)\times10^{-15}$ s^{-1} for the reference MJD 53992.25 (TDB). The uncertainties in parentheses (68%) refer to the last digit(s). The characteristic spin-up time scale, $-P/\dot{P}$, is ∼40 years, somewhat longer than during the first giant outburst. We also note that the $\dot{P}$ appears to be linearly correlated with the X-ray luminosity (see last two columns in Table 7.4). The slope from a linear fit is 36 ± 2 (s s^{-1})/(erg cm^{-2}s^{-1}), although it is based on only three data points (**see Figures 8.4** and 8.5 Section 8 for detailed discussion).

7.3.2 Pulse profiles

Using the determined values of P and $\dot{P}$ (Table 7.4) we constructed pulse profiles for each observation. Pulse profiles from OBS1 and OBS2 are found to be very similar. This can be expected considering that the luminosity of the source during these observations was approximately the same. The results are shown in Figures. 7.3 and 7.4. We do not show pulse profiles from OBS1 since they are similar to OBS2. Figure 7.4 shows the 0.2–10 keV pulse profiles obtained with *XRT*. One can see that the pulse profile obtained in OBS3, during the decay of the outburst, appears significantly different from that obtained in OBS2 when the luminosity was higher.

The 3–20 keV pulse profile from OBS2 and the 0.2–10 keV pulse profile from OBS3 are similar to the corresponding *EXOSAT* profiles from the 1985 giant outburst obtained when the source was at similar luminosity levels (see Fig. 6.5).

7.4 Spectral analysis

For OBS1 pulse averaged X-ray spectra of *ISGRI* and *JEM-X* were analyzed. For OBS2 spectra from *ISGRI, JEM-X, XRT* and *BAT* were fitted simultaneously. In order to account for small scale uncertainties in the response matrices of the respective instruments systematic uncer-

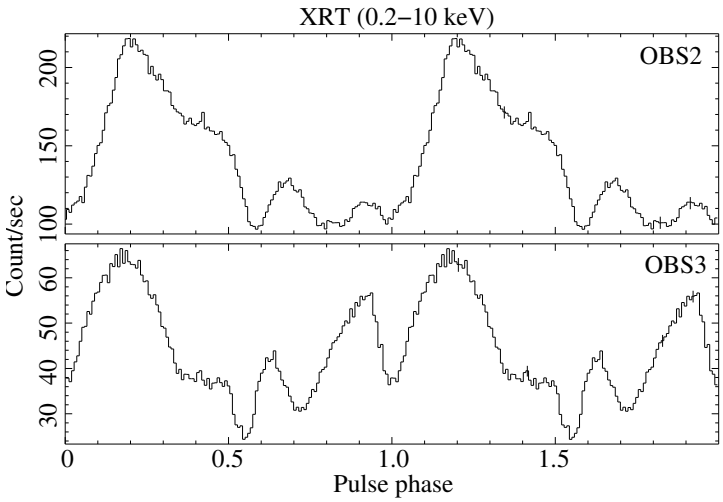

Figure 7.4 X-ray pulse profile obtained with *XRT* during OBS2 (*top panel*) and during OBS3 (*bottom panel)*.

tainties were added at a level of 1% for *ISGRI* and 3% for *JEM-X* and *XRT*. For *BAT* we used energy-dependent systematic errors provided by the *BAT* team. We note that there are additional global systematic uncertainties with the instruments on *INTEGRAL* (e.g. the canonical spectrum of the Crab is not reproduced). The stated uncertainties (e. g. in Tables 3 and 4) are therefore to be taken as lower limits. In the 15–80 keV range these errors are at a level of ∼4%.

To fit the broad band spectral continuum of the source we used an absorbed power law with an exponential cutoff (XSPEC `highecut` model, see Eq. 5.4). An iron emission line at ∼6.5 keV was observed during OBS2 (which has the largest total number of counts) and modeled by a Gaussian emission line. *JEM-X* data revealed an additional feature in 10–20 keV range, which could be explained by a Gaussian emission model at ∼13–15 keV (a "bump"). Alternatively, following the suggestion of a cyclotron line at ∼10 keV by Wilson & Finger (2006), we equally well fitted the spectra adding two Gaussian absorption lines at ∼10 and ∼20 keV to the broad band continuum. As in the case of Her X-1, to account for large systematic uncertainties in the absolute flux measured by the instruments we introduced in our models a free multiplicative factor for each instrument: $F_{\rm ISGRI}$, $F_{\rm XRT}$, and $F_{\rm BAT}$ (for *JEM-X* the factor was fixed to 1.0). The best fit spectral parameters for OBS1 and OBS2 are listed in Table 7.5 (for the model with a "bump") and Table 7.6 (for the model with two absorption lines). The broad band spectrum of OBS2 fitted with `highecut` is shown in Figure 7.5a. Figures 7.5b, 7.5c and 7.5d show the residuals after fitting the spectrum by the `highecut` model without additional features between 10 and 20 keV, with a "bump" around 15 keV, and, alternatively, with two Gaussian absorption lines.

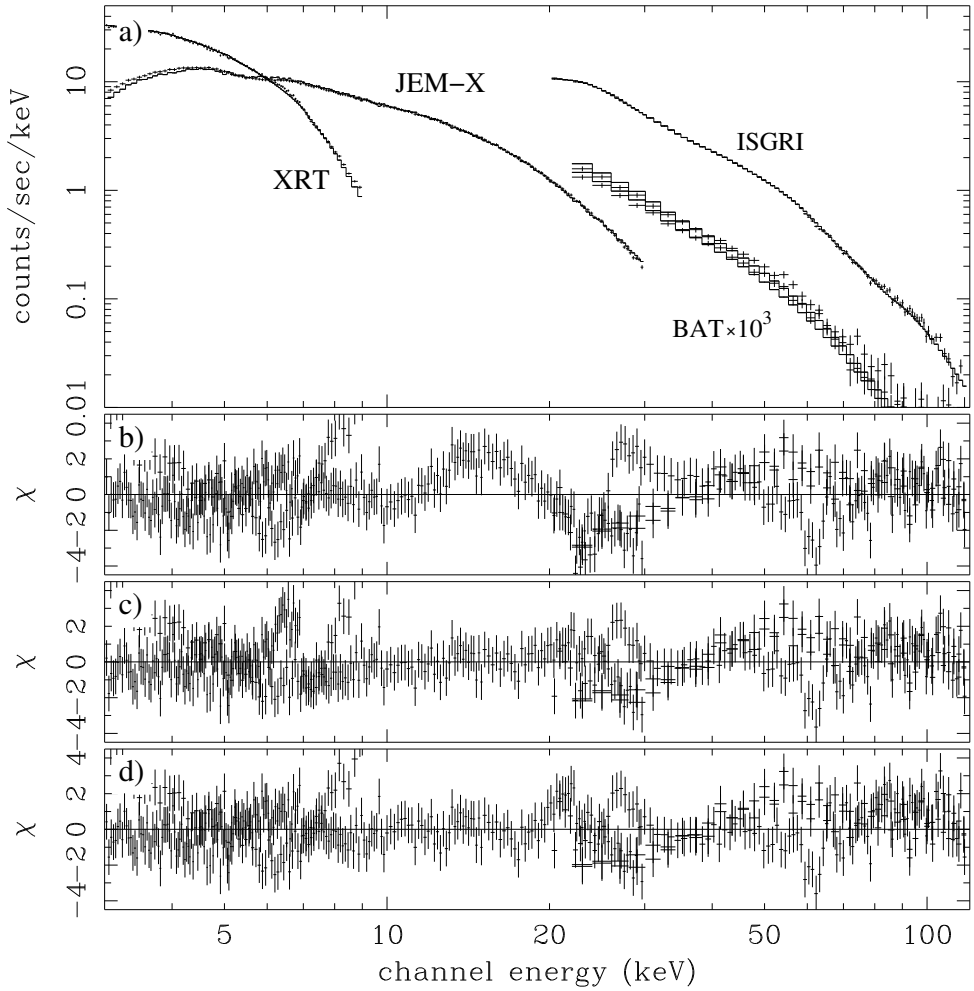

Figure 7.5 The broad band spectrum of EXO 2030+375 from simultaneous fits of *INTEGRAL* and *Swift* data of OBS2 with `highecut` (a) and residual plots after fitting it without additional features (b), adding a "bump" around 15 keV (c), or alternatively including two absorption lines at ~10 and ~20 keV (d).

Table 7.5 Best fit spectral parameters of EXO 2030+375 using the model with a "bump" around 15 keV (see text). 1σ(68%)-uncertainties for one parameter of interest are shown.

Time of observation (MJD) / Instruments	53943(OBS1) ISGRI, JEM-X	53967(OBS2) ISGRI, JEM-X XRT,BAT
Γ	1.93 ± 0.01	$1.93^{+0.01}_{-0.02}$
$E_{\rm cutoff}$ [keV]	$25.9^{+0.2}_{-0.3}$	$26.4^{+0.2}_{-0.5}$
$E_{\rm fold}$ [keV]	26.1 ± 0.2	26.9 ± 0.2
$E_{\rm Fe}$ [keV]	—	6.6 ± 0.1
$\sigma_{\rm Fe}$ [keV]	—	1.2 ± 0.1
$E_{\rm bump}$ [keV]	15.3 ± 0.2	$13.4^{+0.4}_{-0.5}$
$\sigma_{\rm bump}$ [keV]	2.7 ± 0.2	$4.1^{+0.3}_{-0.5}$
$N_{\rm H}$ [10^{22}cm^{-2}]	3.1 ± 0.2	3.4 ± 0.1
$F_{\rm JEM\text{-}X}$	1.0 (fixed)	1.0 (fixed)
$F_{\rm ISGRI}$	1.20 ± 0.01	1.20 ± 0.01
$F_{\rm XRT}$	—	0.926 ± 0.004
$F_{\rm BAT}$	—	0.91 ± 0.01
$\chi^2_{\rm red}$/d.o.f.	1.1/259	1.3/937

Table 7.6 Best fit spectral parameters of EXO 2030+375 using the model with two absorption lines at ~10 and ~20 keV (see text). 1σ(68%)-uncertainties for one parameter of interest are shown.

Time of observation (MJD) / Instruments	53943(OBS1) ISGRI, JEM-X	53967(OBS2) ISGRI, JEM-X XRT,BAT
Γ	1.79 ± 0.01	1.78 ± 0.01
$E_{\rm cutoff}$ [keV]	19.8 ± 0.4	19.5 ± 0.3
$E_{\rm fold}$ [keV]	24.2 ± 0.2	$24.7^{+0.1}_{-0.2}$
$E_{\rm Fe}$ [keV]	—	6.51 ± 0.03
$\sigma_{\rm Fe}$ [keV]	—	$0.32^{+0.04}_{-0.03}$
$E_{\rm 1st\ line}$ [keV]	$10.0^{+0.2}_{-0.3}$	$10.6^{+0.1}_{-0.2}$
$\sigma_{\rm 1st\ line}$ [keV]	$1.6^{+0.4}_{-0.3}$	0.7 ± 0.2
$E_{\rm 2nd\ line}$ [keV]	20.7 ± 0.3	20.6 ± 0.3
$\sigma_{\rm 2nd\ line}$ [keV]	1.3 ± 0.3	$2.0^{+0.3}_{-0.2}$
$N_{\rm H}$ [10^{22}cm^{-2}]	2.2 ± 0.2	3.1 ± 0.1
$\chi^2_{\rm red}$/d.o.f.	1.1/256	1.3/934
$F_{\rm JEM\text{-}X}$	1.0 (fixed)	1.0 (fixed)
$F_{\rm ISGRI}$	1.25 ± 0.01	1.20 ± 0.01
$F_{\rm XRT}$	—	0.926 ± 0.004
$F_{\rm BAT}$	—	0.90 ± 0.01

Chapter 8

Discussion

8.1 Her X-1

8.1.1 Secular change of the orbital period

The precise timing analysis of the *RXTE* observations in combination with the historical data (Section 4.2) allowed us to explore the secular change of the orbital period in Her X-1/HZ Her originally reported by Deeter et al. (1981). As a result, we improved the value of $\dot{P}_{\rm orb}$ which is found to be $-4.74(9) \times 10^{-11}$ s/s. This is slightly smaller in absolute value than $\dot{P}_{\rm orb}$ determined by Deeter et al. (1981): -6.16×10^{-11} s/s.

In order to connect the found value of the secular variation of the orbital period with the physical parameters of the system we will consider a very simplified model, in which the two stars comprising the binary are treated as point masses and only orbital angular momentum is considered. We will neglect the angular momentum of the accretion disk and accretion stream as well as their dynamic action on the stars. Although it is known that this assumption can strongly affect the final result (see e.g. D'Souza et al. 2006), a proper calculation of these effects would require an explicit numerical modeling of the mass transfer which is beyond the scope of this work. In our simple model in case of a circular orbit the total angular momentum of the system J is given by expression:

$$J = \omega_{\rm orb} r_{\rm ns}^2 M_{\rm ns} + \omega_{\rm orb} r_{\rm opt}^2 M_{\rm opt}, \tag{8.1}$$

where $M_{\rm ns}$ and $r_{\rm ns}$ are the mass of the neutron star and the radius of its orbit, respectively; $M_{\rm opt}$ and $r_{\rm opt}$ are the mass and the radius of the orbit of the optical companion, respectively; $\omega_{\rm orb} = 2\pi/P_{\rm orb}$ is the orbital angular frequency of the system. Using Kepler's third law, $\omega_{\rm orb}^2 (r_{\rm ns} + r_{\rm opt})^3 = G(M_{\rm ns} + M_{\rm opt})$, and taking into account that $M_{\rm ns} r_{\rm opt} = M_{\rm opt} r_{\rm ns}$ (from the definition of the center of mass) we arrive at

$$J = \frac{M_{\rm ns} M_{\rm opt} G^{2/3}}{(M_{\rm ns} + M_{\rm opt})^{1/3} \omega_{\rm orb}^{1/3}}. \tag{8.2}$$

Here G is the gravitational constant. Taking the natural logarithm of both sides and differentiating them with respect to time we obtain the expression for the change of the angular momentum of the system:

$$\frac{\dot{J}}{J} = \frac{\dot{M}_{\rm ns}}{M_{\rm ns}} + \frac{\dot{M}_{\rm opt}}{M_{\rm opt}} - \frac{\dot{M}_{\rm ns} + \dot{M}_{\rm opt}}{3(M_{\rm ns} + M_{\rm opt})} + \frac{\dot{P}_{\rm orb}}{3P_{\rm orb}}. \tag{8.3}$$

In case of the conservative mass transfer $\dot{J} = 0$ and $\dot{M}_{\rm ns} = -\dot{M}_{\rm opt}$ (all matter lost by the optical companion is accreted by the neutron star). Equation 8.3 transforms to

$$\frac{\dot{M}_{\rm ns}}{M_{\rm ns}} - \frac{\dot{M}_{\rm ns}}{M_{\rm opt}} + \frac{\dot{P}_{\rm orb}}{3P_{\rm orb}} = 0. \tag{8.4}$$

In this idealized case, using $M_{\rm ns} = 1.4M_{\odot}$, $M_{\rm opt} = 2.2M_{\odot}$, and the found value of $\dot{P}_{\rm orb} = -4.74 \times 10^{-11}$ s/s, we obtain a mass accretion rate of the neutron star $\dot{M}_{\rm ns} \sim 6 \times 10^{17}$ g s^{-1}. This value is smaller than that found by Deeter et al. (1981) but still roughly three times higher than the accretion rate necessary to provide the observed X-ray luminosity $L_{\rm X} \sim 2 \times 10^{37}$ erg s^{-1} assuming that the radiative efficiency of accretion is ∼10%). To explain this Deeter et al. (1981) suggested that the mass transfer is not conservative ($\dot{M}_{\rm ns} \neq -\dot{M}_{\rm opt}$) and matter may leave the system in the form of magnetically channeled wind from the X-ray heated surface of the companion star (Ruderman et al. 1989) carrying away angular momentum. Thus, only part of the matter provided by the normal companion is accreted by the neutron star providing the observed level of X-ray luminosity. We argue, however, than the model used for conservative mass transfer is very approximate and may provide only very rough estimate of $\dot{M}_{\rm ns}$. The obtained discrepancy, therefore, cannot rule out the conservative scenario.

As an alternative to the solution with continuous decrease of the orbital period Deeter et al. (1981) proposed a solution assuming a constant $P_{\rm orb}$ with a sudden jump around 1983 (the dashed lines in Figure 4.4). It was motivated by the unusually long Anomalous Low State (ALS) of the source that took place in 1983–1984. Deeter et al. (1981) suggested that if the change in the orbital period is confined to the ALS then both phenomena can be explained by a sudden temporary increase in the rate of mass transfer from the normal companion to the neutron star. Following this suggestion, Stelzer et al. (1997) performed a fit of the timing data of Her X-1 available at their time using both models. They found that the model with a sudden jump around 1983 provides a better χ^2 than the model assuming continuous decrease of $P_{\rm orb}$, and hence cannot be rejected. However, taking into account the latest *RXTE* data analyzed in this work, the possibility of a sudden jump in $P_{\rm orb}$ can be ruled out (see Section 4.2.3). Thus, we can claim that the decrease of the orbital period of Her X-1/HZ Her originally discovered by Deeter et al. (1981) is due to a constant negative $\dot{P}_{\rm orb}$ and is not confined to any short time interval (like a jump around 1983). We also note that from our disk–stream coupling model (see the next Section) we expect a decrease of the mass transfer to the neutron star during ALSs rather than an increase. This is confirmed by a spin-down observed during most of ALSs (see Fig. 4.9). We argue, therefore, that the most probable explanation of the secular decrease in the orbital period of Her X-1 is a continuous mass transfer from the normal companion to the neutron star in a conservative or non-conservative scenario.

The found $\dot{P}_{\rm orb}$ along with the values of $T^{\rm ref}_{\frac{\pi}{2}}$ and $P^{\rm ref}_{\rm orb}$ determined in Section 4.2.3 (see Table 4.4) comprise a new orbital ephemeris of Her X-1 that can be used to calculate the orbital period, $P_{\rm orb}$, and the time $T_{\frac{\pi}{2}}$, where the mean longitude is 90°, for any particular observation. This allows to perform a precise correction of the photon arrival times for the orbital motion in the binary for a subsequent timing analysis. In Section 5.3 the new ephemeris was used in the timing analysis of the *INTEGRAL* observations of Her X-1. We repeat the new ephemeris below.

$T^{\rm ref}_{\frac{\pi}{2}}$ [MJD(TDB)]	46359.871938(6)
$P^{\rm ref}_{\rm orb}$ [days]	1.700167591(2)
$\dot{P}_{\rm orb}$ [d/d]	$-4.74(9)\times10^{-11}$

8.1.2 The disk–stream coupling model

In Section 4.4.2 we described the numerical model which we used to reproduce the observed anomalous dip behavior. As mentioned before, this model was elaborated by Shakura et al. (1999) and further developed by Klochkov et al. (2006). The detailed numerical calculations are provided in Appendix C. It should be noted that our model is highly idealized. Although detailed numerical calculations of precessing twisted accretion disks including viscous forces have been presented by several authors (e.g. Bardeen & Petterson 1975; Petterson 1977), only simplified models have been used to account for the wobbling motion of the accretion disk (see e.g. Levine & Jernigan 1982, where only tidal wobbling is considered). Thus, it is hardly now possible to check our model, where both tidal forces and dynamical actions of the accretion stream are included, by numerical simulations. However, even this simplified model explains most properties of the averaged X-ray light curve of Her X-1: the duration of the main-on and short-on states, the appearance and behavior of pre-eclipse dips and of anomalous dips and post-eclipse recoveries (see Fig. 4.18).

In our calculations we ignored viscous torques exerted on the outer regions of the disk. Taking them into account complicates the model and can only be done introducing new assumptions about the shape of the twisted and tilted accretion disk in Her X-1. We expect that the effects of the viscosity will be the following: The viscosity always tends to reduce the tilt of the disk. It counterbalances the dynamical action of the stream tending to restore the tilt, so at any given time there is an equilibrium tilt angle. Weakening the stream (for example, by decreasing the mass transfer) would ultimately result in a smaller tilt of the disk, which we believe is the physical reason for the appearance of ALSs.

To account for the observed behavior of the anomalous dips and post-eclipse recoveries, we have to assume a change of the tilt of the outer parts of the disk with precessional phase. In the short-on state the tilt is three times smaller than in the main-on state. As mentioned in Section 4.4, this change can be due to variation of the accretion stream intensity with 35 d phase. Such a variation is expected in the model assuming free precessing of the neutron star. X-ray illumination of the optical companion's atmosphere caused by the precessing neutron star will periodically change with precessional phase. We mention here that the author is currently working on the modeling of the optical light curves of HZ Her (the work is in its final stage and the results will be published elsewhere). This analysis shows additional evidence of a change of the disk tilt with 35 d phase in a similar way as suggested in the described model.

Below we demonstrate that the disk-stream coupling model presented here is able to explain the observed correlation between the 35 d period and the spin period of the neutron star found in Section 4.3.4. As one can see in Figure 4.9, the $(O-C)$ (which is used to explore the 35 d period of the disk precession) and the neutron star spin period $P_{\rm spin}$ are anti-correlated. If we assume that the mass transfer rate $\dot{M}$ increases due to some reason this would cause an increase of the accretion stream intensity. As the stream, according to our model, tends to slow down the disk precession (see Section 4.4.2 and Shakura et al. 1999), the increase of its intensity (i.e. the mass transfer rate through the stream) will result in a slower precession of the disk. The $(O-C)$, therefore, will go up

in the middle panel of Figure 4.9. On the other hand, an increase of the mass accretion rate will spin up the neutron star. The spin period shown in the upper part of Figure 4.9 hence will go down. The observed anti-correlation of $(O-C)$ and $P_{\rm spin}$, therefore, confirms the described physical picture.

8.1.3 Correlation of X-ray luminosity with spin-up rate

In Section 4.3.4 we found evidence for a positive correlation between the spin-up rate of the source ($-\dot{P}_{\rm spin}$) determined from the *BATSE CGRO* data and the X-ray flux $L_{\rm X}$ derived from the maximum main-on flux measured with the *ASM RXTE*. Such a correlation is predicted by basic accretion theory (Pringle & Rees 1972) which assumes that the angular momentum of the infalling matter is transferred to the neutron star at the magnetospheric boundary (see also Section 8.2.1). This simple model does not take into account spin-down torques. In Her X-1, however, episodes of spin-down on top of the mean spin-up trend are clearly observed (see the top panel of Figure 4.9). A more realistic accretion torque model, therefore, has to be used. To fit our values of $L_{\rm X}$ and $\dot{P}_{\rm spin}$ found in Section 4.3.4 we used the model developed by Ghosh & Lamb (1979) which takes into account spin-down torques. According to this model the spin-up rate of the neutron star depends on the X-ray luminosity in a following way:

$$\dot{P}_{\rm spin} = -5\times10^{-5}\mu_{30}^{2/7} n(\omega_s) S_1 (P_{\rm spin} L_{37}^{3/7})^2 \,{\rm s\,yr^{-1}}, \tag{8.5}$$

where μ_{30} is the magnetic moment of the neutron star in units of 10^{30} G cm^3, L_{37} is the luminosity of the source in units of 10^{37} erg s^{-1}, S_1 is a structure parameter depending on the mass, equation of state, and dynamical response of the neutron star, ω_s is the so-called fastness parameter defined as the ratio of the stellar angular velocity and the Keplerian angular velocity at the magnetospheric boundary, and $n(\omega_s)$ is the dimensionless torque introduced by Ghosh & Lamb (1979). As ω_s increases, $n(\omega_s)$ decreases, eventually reaching zero at a critical fastness where the spin-up and spin-down torques exactly balance each other. We have computed ω_s using the approximation given by Eq. 16 in Ghosh & Lamb (1979), and $n(\omega_s)$ using that given by Eq. 10 in Ghosh & Lamb (1979). We used the value of $S_1 = 0.87$ determined from Eq. 17 of Ghosh & Lamb (1979) for a neutron star with a mass of $1.4M_\odot$, radius of 10^6 km, and a moment of inertia of 10^{45} g cm^2. Fitting our values of $\dot{P}_{\rm spin}$ and $L_{\rm X}$ (calculated from the maximum main-on flux) determined in Section 4.3.4 by the formula (8.5) we obtain for Her X-1 a value for the magnetic moment (the only fit parameter of the model) $\mu \sim 0.6\times10^{30}$ G cm^3. This corresponds to the magnetic field strength $B \sim 1.2\times10^{12}$ G which is a factor of $\sim$2.5 lower than the value derived from the cyclotron line energy (see Section 3.2.4). However, taking into account uncertainties in the model parameters (e.g. radiative effectiveness of accretion and the complicated magnetic field structure at the site of the line formation) the difference by only a factor of 2.5 of the B-field strength obtained using completely independent methods can be considered as a good agreement. We argue, therefore, that the correlation between the spin-up rate of the neutron star and its X-ray luminosity in Her X-1 found in this work is consistent with the magnetic field $B \sim 10^{12}$ G found from the energy of the cyclotron line.

8.1.4 Correlation of the cyclotron line energy and the X-ray luminosity

Shifts of cyclotron line energies $E_{\rm cycl}$ have been found to occur with changing X-ray luminosity in a number of high luminosity transient sources: V 0332+53 (Tsygankov et al. 2006; Mowlavi et al. 2006), 4U 0115+63 (Nakajima et al. 2006; Tsygankov et al. 2007b), Cep X-4 (Mihara

et al. 1998). These correlations are negative: $E_{\rm cycl}$ is reduced when $L_{\rm X}$ increases. Mihara et al. (1998) have interpreted this as due to a change in height of the shock (and emission) region above the surface of the neutron star with changing mass accretion rate, $\dot{M}$. As shown by Burnard et al. (1991), the height of the polar accretion structure is tied strongly to $\dot{M}$. If the accretion is in the local super-Eddington regime (when the radiation pressure becomes important and the radiative shock forms) one expects that an increase in accretion rate leads to an increase in the height of the scattering region above the neutron star surface, and therfore to a decrease in magnetic field strength and hence $E_{\rm cycl}$. In Her X-1, however, we report a positive correlation of $E_{\rm cycl}$ with $L_{\rm X}$ (see Section 4.3.5, Staubert et al. 2007b). We have found that the centroid energy of the CRSF changes by ∼5% in energy for a factor of two in luminosity. We suggest that in this source the X-ray luminosity at the magnetic poles of the neutron star is smaller than the local Eddington luminosity, i.e. the accretion is in the sub-Eddington regime. The physical picture of accretion in this case was discussed by Nelson et al. (1993). They assumed that in the low-luminosity X-ray pulsars one can neglect the possibility for the formation of a collisionless shock and the accreting protons lose their kinetic energy in an electron-proton atmosphere due to Coulomb drag and collective plasma effects. An increase of $\dot{M}$ in this case will effectively push down the electron-proton atmosphere and hence the emission region closer to the neutron star surface where the magnetic field strength is higher. This will lead to a positive correlation between $L_{\rm X}$ (which is proportional to $\dot{M}$) and $E_{\rm cycl}$ (which is proportional to the B-field strength). The detailed calculation performed by Staubert et al. (2007b) shows that for a change of a factor of two in $L_{\rm X}$ the expected fractional change in the cyclotron line energy is $\Delta E_{\rm cycl}/E_{\rm cycl} \simeq 0.03$, which is very close to the observed value of 5%.

As one can see, the decisive parameter which determines the sign of the correlation between $E_{\rm cycl}$ and $L_{\rm X}$ in an accreting pulsar is the local Eddington rate at the neutron star. Its value depends on the area upon which accretion proceeds, so it is expected to vary from pulsar to pulsar. In transient pulsars, such as 4U 0115+63, we may already have evidence for a transition from local super- to sub-Eddington accretion (Tsygankov et al. 2007b; Nakajima et al. 2006; Terada et al. 2006) at the decline of the outburst when the luminosity drops below $\sim 5 \times 10^{37}$ erg s^{-1}. The sharp jump in the observed cyclotron line energy in 4U 0115+63 reported by Tsygankov et al. (2007b) could be a sign of an abrupt change in the structure of the accretion column during such a transition.

It is conceivable that long-term variations in the accretion rate exist also in the persistent X-ray pulsar Her X-1. If so, we also speculate that the abrupt jump in the cyclotron line energy in Her X-1 noticed in the early 1990s (see Fig. 3.5) might be associated with a transition of this pulsar from super-Eddington to sub-Eddington accretion.

8.1.5 Pulse profiles

In Section 5.3.2 we constructed 1.24s X-ray pulse profiles of Her X-1 using the data obtained with the *INTEGRAL* instruments. The shape of the profile was found both energy- and time-dependent.

At higher energies the main peak becomes narrower and the pulsed fraction increases (Figs. 5.5 and 5.6). Such a dependence of the profile on energy is typical for accreting pulsars (see e.g. Tsygankov et al. 2007a). It can be understood in a simple purely geometrical picture: if the rotation axis of the neutron star is inclined with respect to the axis of its magnetic field, it is expected that the upper part of the accretion column emitting softer photons is seen during a larger part of the neutron star spin period while the emission region of harder photons, “footstep” of the accretion

column, is screened by the neutron star surface during most part of the spin period. Additionally, the emission diagram of harder photons is believed to be narrower than that of softer photons (see Basko & Sunyaev 1976, see also discussion in Section 8.1.8).

The difference of the pulse profiles in the left and right columns of Figure 5.5 (corresponding to the beginning and the end of the main-on state, respectively) shows the evolution of the profiles with 35 d phase. As mentioned in Section 3.2.3, two models have been proposed to explain these variations. Scott et al. (2000) suggested that the change of the profile from the beginning to the end of the main-on state is due to a "resolved occultation" of the emitting regions on the neutron star by the precessing accretion disk. According to this model, the disk progressively occults the neutron star towards the end of the main-on. In the model of free precession of the neutron star the observed behavior of the profile is explained assuming that the emission region on the star surface has a complex shape (due to the presence of higher multipole components of the neutron star's magnetic field). Changing the viewing conditions of the emitting region with the phase of the free precession causes the observed variation of the pulse profile (see Section 3.3 Ketsaris et al. 2000; Wilms et al. 2003). In pulse profiles obtained with *INTEGRAL* and presented in this work one can see that the count rate at the maximum of the main peak is higher at the end of the main-on than that during the beginning of the main-on (Fig. 5.5). In case of a progressive occultation one would only expect a decrease in the intensity of any feature in the profile towards the end of the main-on. In the model of free precession, however, viewing conditions of different parts of the emission region may change with the precessional phase of the star in such a way that the intensity of particular features of the profile (e.g of the main peak) will increase towards the end of the main-on. We argue, therefore, that the *INTEGRAL* observations analyzed in this work lend some support to the model of a freely precessing neutron star as an explanation of the time variation of the pulse profile in Her X-1.

8.1.6 Short-time scale variations of the pulse period

In Section 5.3.3 we determined the time derivative of the intrinsic (not affected by the orbital motion in the binary) pulse period of the neutron star in Her X-1 during the *INTEGRAL* observation. The pulsar was found to spin-up with the rate $-\dot{P}_{\rm spin} = (5.8 \pm 1.5) \times 10^{-13}$s/s. This value is more than five times larger than the mean spin-up trend of Her X-1 ($\sim 1.1 \times 10^{-13}$ s/s) and consistent with the variations of $P_{\rm spin}$ between subsequent 35 d cycles seen in *BATSE* data (Fig. 4.12). Along with the maximum *ASM* count rate measured during the corresponding main-on state, the *INTEGRAL* measurement of $\dot{P}_{\rm spin}$ turn out to be in line with the found correlation between the spin-up rate in the maximum main-on flux (see Sections 8.1.3 and 4.3.4). Figure 8.1 shows $\dot{P}_{\rm spin}$ versus the maximum main-on flux (the same as in Fig. 4.13) where we added the *INTEGRAL* data point (marked with thick error bars). We stress that in the *INTEGRAL* observation the pulse period derivative was measured using the data within one main-on state while for other data points it was determined using the pulse period values measured in adjacent main-ons. We conclude, therefore, that the short-term variation of the pulse period in Her X-1 are mainly related to the variations in the mass accretion rate (which the X-ray luminosity is proportional to).

8.1.7 Absorption during X-ray dips

In Section 5.4.2 we have shown that the X-ray spectrum of Her X-1 obtained during X-ray dips can be modeled using a so-called partial covering model which assumes that the observed

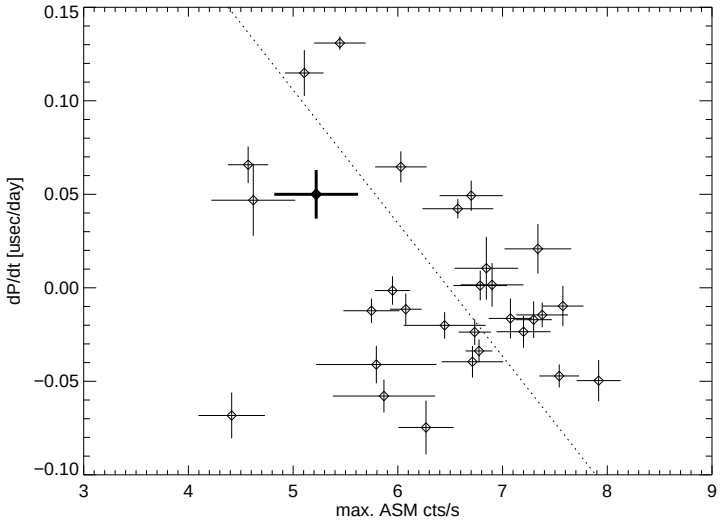

Figure 8.1 The negative correlation between $\dot{P}_{\rm spin}$ and the maximum main-on flux. The plot is the same as in Figure 4.13 except that the *INTEGRAL* observation is added (marked by thick error bars).

spectrum is a combination of direct and absorbed radiation. Such a combination has already been observed in Her X-1 during X-ray turn-ons (Davison & Fabian 1977; Becker et al. 1977; Parmar et al. 1980; Kuster et al. 2005).

According to our model (Section 3.3), most of the X-ray dips are produced by the occultation of the X-ray source by the cold matter in the accretion stream that moves out of the system orbital plane. If the stream is not continuous but consists of "blobs" of material then the source will be screened during some time intervals within a dip. Between these intervals the source will be opened or seen through less dense material. This picture seems to be confirmed by the complicated behavior of the light curve inside the dips (Fig. 5.10). In our analysis, in order to construct an X-ray spectrum of acceptable quality we have to accumulate the flux during complete dips. The spectrum in this case will contain a superposition of the absorbed and non-absorbed flux. The fact that our partial covering model fits the spectrum from the dips better than the simple absorption model reflects the described effect.

8.1.8 Pulse-phase variability of the X-ray spectrum

It was shown in Section 5.4.3 that the spectral parameters of Her X-1 are highly pulse-phase dependent. The spectral changing with pulse phase is a common feature in X-ray pulsars (see e.g. Kreykenbohm et al. 2004, and references therein) which is usually attributed to the change of the viewing angle of the accretion region on the neutron star surface. Below we show that the pulse-phase variability observed in Her X-1 is basically consistent with this interpretation.

As one can see in Figure 5.13, the power law photon index Γ symmetrically decreases during the main peak. It ranges from ∼1.0 in the off-pulse to ∼0.5 close to the maximum of the main peak. This effect reflects the sharpening of the peak with energy which is observed in energy-resolved pulse profiles constructed in Section 8.1.5 (Fig. 5.5). The spectral hardening in the main peak can be explained by the dependence of the optical depth on the angle between the line-of-sight and the magnetic field lines (Pravdo et al. 1977). The closer the viewing direction is to the

magnetic axis, the deeper we look into the emission region where harder photons originate. Since it is generally accepted that the main peak corresponds to the radiation from one of the two magnetic poles, the viewing direction is closest to the magnetic axis during the main peak which causes the observed effect.

The exponential folding energy $E_{\rm fold}$ reaches its maximum around the main peak. In comptonized X-ray spectra (which are normally observed from accreting pulsars) this parameter is believed to be proportional to the plasma temperature (see e.g. Rybicki & Lightman 1979). As already mentioned, during the main peak we see the emission from higher optical depth. This means that the observed radiation originates closer to the footstep of the accretion column where the plasma temperature is higher.

The cyclotron line centroid energy $E_{\rm cycl}$ also increases towards the main peak of the profile with a relative amplitude of ∼25% (Fig. 5.14). As argued from Γ and $E_{\rm fold}$, during the main peak we see X-rays that originate closer to the neutron star surface, i.e. where the magnetic field strength is higher. The increase in $E_{\rm cycl}$ during the main peak is, therefore, qualitatively consistent with this picture. If one assumes that the radiation comes from a compact accretion column located at the magnetic pole of the neutron star with a pure dipole field then the change in the height of the observed emission region necessary to produce a ∼25% variation of the magnetic field strength is ∼1.1 km (for a neutron star radius of 10 km). However, as it was shown by Staubert et al. (2007a), the height of the emission and line forming region in case of Her X-1 is most probably much smaller, $\sim 10^4$ cm. Thus, a changing height of the emitting region above the neutron star cannot explain the observed variability of the cyclotron line energy with pulse phase in this source.

Another possibility for the line energy variability is to assume a complicated structure of the magnetic field at the site of X-ray emission. As shown by Shakura et al. (1991) and Panchenko & Postnov (1994), the complex shape of the observed pulse profiles in Her X-1 suggests that such a complicated field structure including higher multipole components is indeed present in the source. In this case, at different rotational phases of the neutron star we will observe emission coming from the regions corresponding to different sub-structures of the non-dipole magnetic field with very different field strengths. Furthermore, the numerical modeling of Her X-1 pulse profiles observed with *EXOSAT* performed by Panchenko & Postnov (1994) suggests that the magnetic field stength at the ring-like structure on the neutron star's surface corresponding to the quadrupole component of the field (which was introduced in the model) is indeed by ∼27% lower than that at the magnetic pole. Thus, a complicated magnetic field structure on the surface of the neutron star can cause the observed 25%-variation of $E_{\rm cycl}$ with pulse phase.

8.2 EXO 2030+375

8.2.1 X-ray luminosity – $\dot{P}_{\rm spin}$ relation: probing the accretion theory

As mentioned in Section 6.3, if an accretion disk is present in an accreting pulsar system, one expects a correlation between the rate of change of the pulse period and the observed X-ray flux. This correlation can be used to compare different accretion torque models and to determine physical parameters of the system such as luminosity and magnetic dipole moment of the neutron star (see e.g. Rappaport & Joss 1977; Henrichs 1983; Joss & Rappaport 1984). Figure 8.2 (Joss & Rappaport 1984) shows the empirical relation between the fractional rate of change of the pulse period, $\dot{P}/P$, and the parameter $PL_{\rm X}^{6/7}$ for several X-ray pulsars. The solid line shows the relation predicted by the

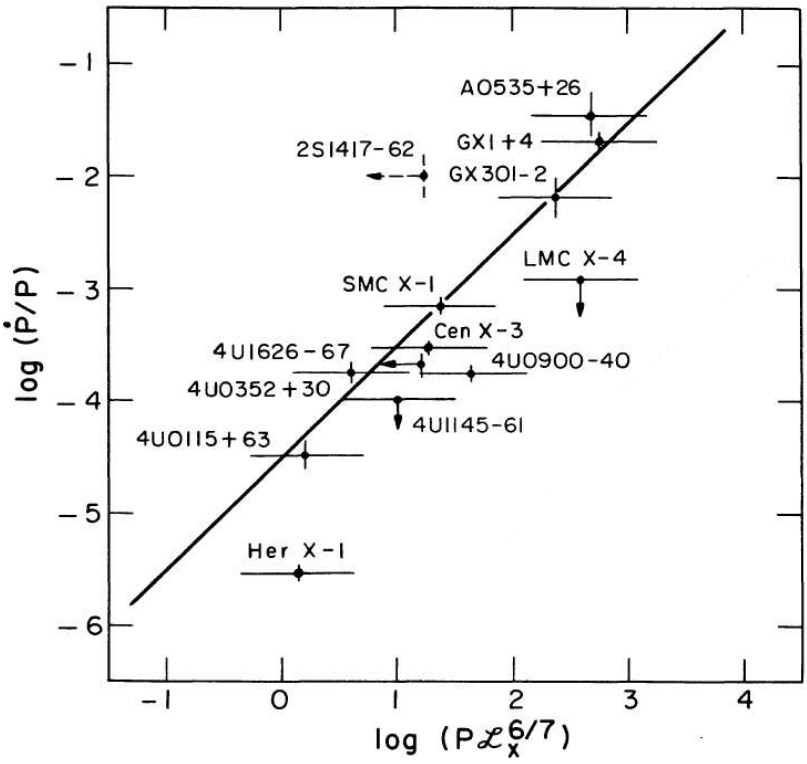

Figure 8.2 The empirical relation between the fractional rate of change of the pulse period, $\dot{P}/P$, and the parameter $PL_{\rm X}^{6/7}$ for several X-ray pulsars. The units of $\dot{P}/P$, P, and $L_{\rm X}$ are yr^{-1}, s, and 10^{37} erg s^{-1}, respectively. The solid line is the relation expected from the simple accretion theory, $-\dot{P} \propto \dot{M}^{6/7}$ (Pringle & Rees 1972). The figure is adopted from Joss & Rappaport (1984).

simple accretion theory (Pringle & Rees 1972) for some "standard" set of neutron star parameters (mass, radius, dipole magnetic moment). Variation of these parameters between different systems causes some scattering of the data points in the plot.

The giant outburst of EXO 2030+375 in 1985 allowed for the first time to study the dependence of the spin-up rate on the X-ray flux in a single source, i.e. for the same neutron star parameters (Parmar et al. 1989b; Reynolds et al. 1993). In this work we compare the luminosity – $\dot{P}_{\rm spin}$ relation observed by *EXOSAT* in 1985 with that measured with *INTEGRAL* in 2006 (see Section 7.3, Table 7.4). Figure 8.4 shows the spin-up rate as a function of the 1–20 keV flux for both outbursts. It is clearly seen that during the 2006 outburst (squares in the plot) the dependence is steeper than during the 1985 outburst. This might indicate a difference in the configuration of the accretion disk and/or the neutron star's magnetosphere in the two outbursts. This would result e.g. in a different radiation pattern on the surface of the neutron star leading to a change of the *beaming factor* which is used to convert the observed X-ray flux into luminosity.

We fit the data from the two outbursts separately using two accretion torque models: (1) the "simple" model with $-\dot{P} \propto \dot{M}^{6/7}$ developed by Pringle & Rees (1972) and (2) the model described by Ghosh & Lamb (1979) which takes into account spin-down torques due to interaction of the accretion disk with the neutron star's magnetosphere beyond the Alfvén radius. As mentioned

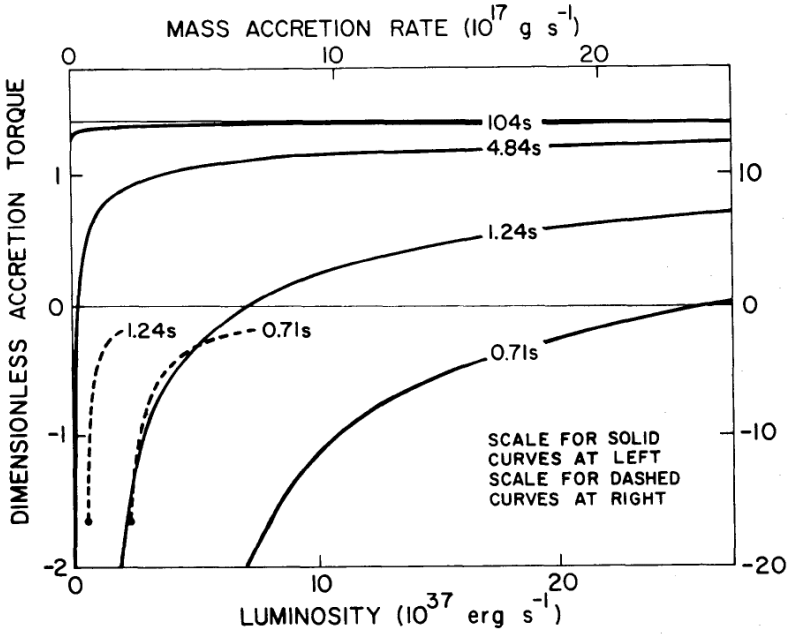

Figure 8.3 The dimensionless accretion torque n on neutron stars of selected periods as a function of the mass accretion rate $\dot{M}$, in units of 10^{17} g s^{-1}, or the luminosity $L_{\rm X}$, in units of 10^{37} erg s^{-1}. Each star is assumed to have a magnetic moment $\mu = 10^{30}$ G cm^3 and a mass $M = 1.3 M_\odot$. The period of each star is written on the corresponding curve. The figure is adapted from Ghosh & Lamb (1979).

in Section 8.1.3, the torque in the first model is calculated assuming that the angular momentum of the infalling matter is transferred to the neutron star at the magnetospheric boundary determined by the Alfvén radius:

$$R_{\rm A} = \left(\frac{\mu^2}{2\dot{M}\sqrt{2GM}} \right)^{2/7}, \tag{8.6}$$

where M is the mass of the neutron star, μ is its dipole magnetic moment, and $\dot{M}$ is the accretion rate. The equation determining the change of the angular momentum of the neutron star in this case has the form

$$\frac{d(I\omega)}{dt} = \dot{M}\sqrt{GMR_{\rm A}}, \tag{8.7}$$

where I is the moment of inertia of the neutron star, ω is the angular frequency. This leads to the following dependence of the spin-up rate of the neutron star on its X-ray luminosity:

$$\dot{P}_{\rm spin} \simeq -1.7 \times 10^{-5} \mu_{30}^{2/7} P_{\rm spin}^2 L_{37}^{6/7} \, {\rm s\,yr^{-1}}. \tag{8.8}$$

The model of Ghosh & Lamb (1979) is described in Section 8.1.3 (Eq. 8.5) where it was used to fit our data of Her X-1. The difference between Equations 8.8 and 8.5 is the presence of the dimensionless accretion torque n in the model of Ghosh & Lamb (1979) (see Section 8.1.3) taking into account the interaction of the accretion disk with the neutron star's magnetic field beyond the corotational radius which tends to slow down the neutron star. The dependence of this torque on the mass accretion rate $\dot{M}$ or luminosity L is shown in Figure 8.3 (according to the approximation given

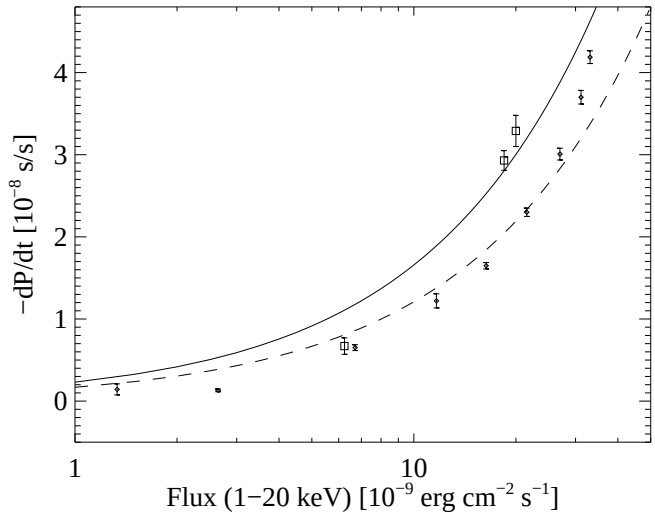

Figure 8.4 Spin-up rate of the neutron star in EXO 2030+375 as a function of 1–20 keV flux measured during the 1985 outburst (small diamonds, Parmar et al. 1989b) and during the 2006 outburst (squares, Klochkov et al. 2006). The solid and dashed lines show fits by the "simple" accretion model $-\dot{P} \propto \dot{M}^{6/7}$ of the data from the 2006 outburst and from the 1985 outburst respectively.

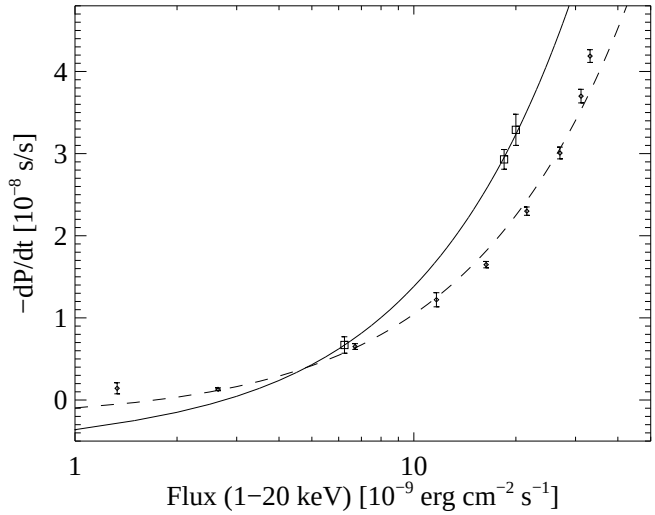

Figure 8.5 The same as in Fig. 8.4 but using the fit by the model described in Ghosh & Lamb (1979)

by Eqs. 10 and 16 in Ghosh & Lamb 1979). One can see that for low $\dot{M}$ the torque can be negative which means that the neutron star will spin down. The introduction of this dimensionless torque leads to a steeper dependence of the spin-up rate on the luminosity with respect to that predicted by the "simple" accretion theory.

We fit the values of $\dot{P}$ and $L_{\rm X}$ (derived from the X-ray flux) in the two giant outbursts by formulae (8.8) ("simple" model) and (8.5) (model of Ghosh & Lamb 1979). As before, we used the value of $S_1 = 0.87$ determined from Eq. 17 of Ghosh & Lamb (1979) for a neutron star with a mass of $1.4M_\odot$, radius of 10^6 km, and a moment of inertia of 10^{45} g cm^2. $n(\omega_s)$ was computed using the numerical approximation given by Eqs. 10 and 16 in Ghosh & Lamb (1979). The solid and dashed curves in Figure 8.4 show the fit by the "simple" accretion model of the data from the 2006 outburst and from the 1985 outburst respectively. Here we use a linear plot instead of logarithmic because the model of Ghosh & Lamb (1979) predicts negative spin-up rates for low fluxes. The free parameter

of the fit is the magnetic dipole moment μ. Both data sets clearly deviate from the model showing a steeper dependence of $(-\dot{P})$ on the X-ray flux. Figure 8.5 shows the fit of the two data sets with the model of Ghosh & Lamb (1979) which shows better agreement with the data (again, the only fitting parameter is μ). For the 2006 outburst the data are in a good agreement with the theoretical curve, but it can be due to poor coverage of the outburst (only three measurements are available). For the 1985 outburst the data at higher fluxes seem to show steeper dependence with respect to the model prediction. Generally, taking into account spin-down torque (the model of Ghosh & Lamb 1979) leads to a better agreement with the data with respect to the "simple" accretion theory of Pringle & Rees (1972) in both giant outbursts.

Considering the uncertainties in the model parameters, both models provide a rough estimate of the neutron star's magnetic dipole moment in the range of $\sim (3-20)\times10^{30}$ G cm^3, which translates into the magnetic field strength of a few times 10^{12} to 10^{13} G. This would be consistent with a fundamental cyclotron line energy in the range $E_{\rm cyc} \sim 10-100$ keV ($E_{cyc} = 11.6\cdot(B/10^{12}\,{\rm G})\times[1+z]^{-1}$ keV, where z is the gravitational redshift which was assumed to be 1.2 in our calculations).

8.2.2 Pulse profiles

As it was shown by Parmar et al. (1989a), the general shape of X-ray pulse profiles of EXO 2030+375 is qualitatively consistent with the simple geometric model where axially symmetric fan and pencil-beams are emitted from two magnetic poles on a rotating neutron star. However, the increasing amount of observational data, including the high energy data obtained with *INTEGRAL* (this work), requires more detailed modeling of the profiles which should take into account a number of geometrical physical effects, such as e.g. gravitational bending and the non-dipole shape of the neutron star's magnetic filed.

As mentioned in Section 7.3.2, the low-energy (< 20 keV) X-ray pulse profiles observed with *INTEGRAL* during the 2006 giant outburst are consistent with the *EXOSAT* pulse profiles observed during the 1985 giant outburst at the corresponding luminosity levels (see Figs. 7.3, 7.4 and 6.5). We repeat here that we corrected the X-ray luminosity of the source measured by *EXOSAT* according to the updated distance to the source (∼7 kpc, Wilson et al. 2002). The *XRT* pulse profile obtained at the maximum of the 2006 outburst when the luminosity was $\sim 1.2\times10^{38}$ erg s^{-1} looks similar to the profiles observed with *EXOSAT* during the 1985 outburst at a luminosity level of $(1.12-1.48)\times10^{38}$ erg s^{-1}. The profiles observed during the decay of the 2006 outburst when the luminosity of the source dropped by a factor of ∼3 look similar to the *EXOSAT* profiles taken at a luminosity level of $(2.4-5.6)\times10^{37}$ erg s^{-1}. This confirms that the pulse profile of EXO 2030+375 is mostly determined by the X-ray luminosity of the source rather than by geometric effects resulting from e.g. a precessing neutron star (like in case of Her X-1). However, a contribution of such geometric effects cannot be completely ruled out on the basis of our observations. The high-energy (> 20 keV) pulse profile is remarkably different with respect to the low-energy one. The main peak at higher energies is more prominent and the pulse fraction is higher. This energy-dependence is similar to that of Her X-1 as discussed in Section 8.1.5.

8.2.3 Broad band X-ray spectrum

In our observations for the first time the broad band X-ray spectrum of the source (including energies above ~25 keV) during a type II outburst is analyzed. The general shape of the continuum is typical for accreting pulsars: a power law modified by photo-absorption at lower energies and by an exponential cut-off at higher energies. Several conclusions and comments can be made concerning the open questions posed by previous X-ray observations of EXO 2030+375. It is seen that the exponential roll-off of the spectrum starting at 25 keV continues at higher energies and, therefore, cannot be interpreted as a cyclotron absorption feature as suggested by Parmar et al. (1989a) on the basis of *EXOSAT* spectra ($\lesssim$ 25 keV). Using our observations we cannot confirm the presence of a cyclotron line at ~36 keV reported by Reig & Coe (1999). The interpretation of the feature around 10 keV as a cyclotron line provided by Wilson & Finger (2006) is also doubtful: inclusion of the broad emission component at ~15 keV leads to flattening of residuals around ~10 and ~20 keV (see Fig. 7.5). From the accretion torque models (Section 8.2.1) the magnetic field strength on the surface of the neutron star can be as high as 10^{13} G. This would place the fundamental cyclotron line at ~100 keV where the statistics of our spectra is rather poor. The observed broad emission feature at ~15 keV (a "bump") may correspond to the broad component observed by Camero Arranz et al. (2005) during a normal outburst of EXO 2030+375. Camero Arranz et al. (2005) modeled the feature by a disk black body radiation with the unusually high temperature, $kT \sim 8$ keV. The origin of the "bump" is not clear. A preliminary pulse phase resolved analysis shows that the spectrum is highly variable with pulse phase. This means that any interpretation of the phase averaged spectrum should be made with caution. Moreover, residual features around 25 keV may hint at calibration uncertainties.

Chapter 9

Summary and conclusions

In this work we analyzed the multi-instrument X-ray observations of two accreting pulsars, Her X-1 and EXO 2030+375. The analysis includes the data from the *RXTE, INTEGRAL,* and *Swift* satellites. The results were used to check and to improve the existing theoretical models of the two binary systems. Below we list the main results of our work.

Her X-1:

- Using the *RXTE* observations of the source along with the historical timing data, we constructed a new orbital ephemeris of the system. The value of secular decrease of the orbital period has been improved (with respect to that found by Deeter et al. 1991). The possibility of a sudden jump of the orbital period during the long Anomalous Low State in 1983–1984 instead of a continuous changing has been ruled out.

- Using the data from *RXTE ASM* and *CGRO BATSE* we studied the long-term behavior of the 35 d period, 1.24s pulsation period, and X-ray luminosity as well as their correlation with each other. A positive correlation between the spin-up rate of the source and its intrinsic X-ray luminosity was found. The dependence between the two values is consistent with the magnetic field strength of $B \sim 10^{12}$ G, in agreement with the value found from the position of the cyclotron line in the X-ray spectrum of the source. An anti-correlation between the 1.24s period and 35 d period was found on long as well as on short time scales and interpreted in terms of the accretion disk–stream coupling model.

- A positive correlation of the cyclotron line energy with the X-ray luminosity of the source is found. It is argued that such a correlation is expected in the case of local sub-Eddington accretion when an increase of the mass accretion rate $\dot{M}$ leads to a decrease of the height of the emission region.

- Averaged 35 d X-ray light curves were constructed using the data from *RXTE ASM*. The anomalous dips and post-eclipse recoveries present in the averaged light curve are successfully reproduced using a numerical model of disk–stream interaction (coupling). The data require a variation of the accretion disk tilt with 35 d phase.

- A strong spin-up is found during the *INTEGRAL* observations. The value of the spin-up rate and the X-ray luminosity measured during the *INTEGRAL* observations are found to be consistent with the correlation between these two values measured on the basis of the data from *RXTE ASM* and *CGRO BATSE* (see above).

- Spectral changes during X-ray dips are studied. The X-ray spectrum of the dips was modeled by a partial covering model which assumes that the observed spectrum is a combination of direct and absorbed radiation. It is suggested that the obscuring matter (accretion stream) is not continuous but rather consists of blobs of material.

- Energy-resolved X-ray pulse profiles as well as the variation of cyclotron line and continuum parameters with 1.24 s pulse phase were explored. The spectral changes with pulse phase are shown to be qualitatively consistent with those expected from the variable viewing conditions of the complex emitting region with rotational phase of the neutron star.

Conclusion: Most of the observed properties of Her X-1/HZ Her can be explained in terms of a single, although highly idealized, qualitative model which includes a precessing, wobbling accretion disk interacting with the accretion stream, and a freely precessing neutron star. There are, however, observational features of Her X-1 that require further study and modeling.

EXO 2030+375

- For the first time the broad band (3–200 keV) X-ray spectrum of the source during a giant outburst was studied. The presence of a cyclotron feature reported earlier by some authors is not confirmed. A broad "bump" is found around ~15 keV.

- The X-ray pulse profiles are found to be highly luminosity-dependent and consistent with those obtained with *EXOSAT* during the 1985 giant outburst at corresponding luminosity levels.

- The dependence of the spin-up rate on the X-ray luminosity during the 2006 giant outburst is measured and compared with that observed during the 1985 giant outburst. There is an indication of a possible change of the configuration of the neutron star's magnetosphere and/or accretion disk between the two giant outbursts. The dependence is modeled using different accretion torque models.

Bibliography

Anderson, P. W. & Itoh, N. 1975, Nature, 256, 25

Anzer, U. & Börner, G. 1983, A&A, 122, 73

Arnaud, K. A. 1996, in Astronomical Society of the Pacific Conference Series, Vol. 101, Astronomical Data Analysis Software and Systems V, ed. G. H. Jacoby & J. Barnes, 17

Baade, W. & Zwicky, F. 1934, Proceedings of the National Academy of Science, 20, 254

Bahcall, J. N. & Bahcall, N. A. 1972, aPj, 178, L1

Balbus, S. A. & Hawley, J. F. 1991, ApJ, 376, 214

Bałucińska-Church, M. & McCammon, D. 1992, ApJ, 400, 699

Bardeen, J. M. & Petterson, J. A. 1975, ApJL, 195, L65

Barthelmy, S. D., Barbier, L. M., Cummings, J. R., et al. 2005, Space Science Reviews, 120, 143

Basko, M. M. 1980, A&A, 87, 330

Basko, M. M. & Sunyaev, R. A. 1976, MNRAS, 175, 395

Baykal, A., Boynton, P. E., Deeter, J. E., & Scott, D. M. 1993, MNRAS, 265, 347

Becker, R. H., Boldt, E. A., Holt, S. S., et al. 1977, ApJ, 214, 879

Begelman, M. C. & McKee, C. F. 1983, ApJ, 271, 89

Bildsten, L., Chakrabarty, D., Chiu, J., et al. 1997, ApJS, 113, 367

Blondin, J. M. 2000, New Astronomy, 5, 53

Blondin, J. M., Kallman, T. R., Fryxell, B. A., & Taam, R. E. 1990, ApJ, 356, 591

Bochkarev, N. G. & Karitskaia, E. A. 1989, ApSS, 154, 189

Bondi, H. & Hoyle, F. 1944, MNRAS, 104, 273

Boynton, P. E., Canterna, R., Crosa, L., Deeter, J., & Gerend, D. 1973, ApJ, 186, 617

Burnard, D. J., Arons, J., & Klein, R. I. 1991, ApJ, 367, 575

Burrows, D. N., Hill, J. E., Nousek, J. A., et al. 2005, Space Science Reviews, 120, 165

Caballero, I., Kretschmar, P., Santangelo, A., et al. 2007, A&A, 465, L21

Camero Arranz, A., Wilson, C. A., Connell, P., et al. 2005, ApJ, 441, 261

Caroli, E., Stephen, J. B., di Cocco, G., Natalucci, L., & Spizzichino, A. 1987, Space Science Reviews, 45, 349

Chandrasekhar, S. 1931, ApJ, 74, 81

Cherepashchuk, A. M., Efremov, Y. N., Kurochkin, N. E., Shakura, N. I., & Sunyaev, R. A. 1972, Informational Bulletin on Variable Stars, 720, 1

Choi, C. S., Nagase, F., Makino, F., Dotani, T., & Min, K. W. 1994, ApJ, 422, 799

Chubb, T. A., Friedman, H., Kreplin, R. W., & Kupperian, J. E. 1957, Nature, 179, 861

Coburn, W., Heindl, W. A., Rothschild, R. E., et al. 2002, ApJ, 580, 394

Coe, M. J. 2000, in ASP Conf. Ser. 214: IAU Colloq. 175: The Be Phenomenon in Early-Type Stars, ed. M. A. Smith, H. F. Henrichs, & J. Fabregat, 656

Coe, M. J., Everall, C., Fabregat, J., et al. 1993, A&AS, 97, 245

Coe, M. J., Payne, B. J., Longmore, A., & Hanson, C. G. 1988, MNRAS, 232, 865

Cooke, B. A. & Page, C. G. 1975, Nature, 256, 712

Corbet, R. H. D. & Levine, A. M. 2006, The Astronomer's Telegram 843

Courvoisier, T. J.-L., Walter, R., Beckmann, V., et al. 2003, A&A, 411, L53

Crampton, D. 1974, ApJ, 187, 345

Crosa, L. & Boynton, P. E. 1980, ApJ, 235, 999

Dal Fiume, D., Orlandini, M., Cusumano, G., et al. 1998, A&A, 329, L41

Daugherty, J. K. & Harding, A. K. 1986, ApJ, 309, 362

Davison, P. J. N. & Fabian, A. C. 1977, MNRAS, 178, 1P

Deeter, J. E., Boynton, P. E., Miyamoto, S., et al. 1991, ApJ, 383, 324

Deeter, J. E., Pravdo, S. H., & Boynton, P. E. 1981, ApJ, 247, 1003

Deeter, J. E., Scott, D. M., Boynton, P. E., et al. 1998, ApJ, 502, 802

D'Souza, M. C. R., Motl, P. M., Tohline, J. E., & Frank, J. 2006, ApJ, 643, 381

Frank, J., King, A., & Raine, D. 1992, Accretion Power in Astrophysics (Accretion Power in Astrophysics, ISBN 0521408636, Cambridge University Press, 1992.)

Gehrels, N., Chincarini, G., Giommi, P., et al. 2004, ApJ, 611, 1005

Gerend, D. & Boynton, P. E. 1976, ApJ, 209, 562

Ghosh, P. & Lamb, F. K. 1979, ApJ, 234, 296

Giacconi, R. & Gursky, H., eds. 1974, X-ray astronomy

Giacconi, R., Gursky, H., Kellogg, E., et al. 1973, ApJ, 184, 227

Giacconi, R., Gursky, H., & Waters, J. R. 1964, Nature, 204, 981

Giacconi, R., Murray, S., Gursky, H., et al. 1972, ApJ, 178, 281

Gorecki, A., Levine, A., Bautz, M., et al. 1982, ApJ, 256, 234

Gruber, D. E., Heindl, W. A., Rothschild, R. E., et al. 2001, ApJ, 562, 499

Hanuschik, R. W. 1996, A&A, 308, 170

Harris, D. E., Forman, W., Gioia, I. M., et al., eds. 1993, The Einstein Observatory catalog of IPC X ray sources. Volume 1E: Documentation, Vol. 1

Heindl, W. A., Rothschild, R. E., Coburn, W., et al. 2004, in American Institute of Physics Conference Series, Vol. 714, X-ray Timing 2003: Rossi and Beyond, ed. P. Kaaret, F. K. Lamb, & J. H. Swank, 323–330

Heiselberg, H. & Pandharipande, V. 2000, Annual Review of Nuclear and Particle Science, 50, 481

Henrichs, H. F. 1983, in Accretion-Driven Stellar X-ray Sources, ed. W. H. G. Lewin & E. P. J. van den Heuvel, 393–429

Howarth, I. D. & Wilson, B. 1983, MNRAS, 202, 347

Illarionov, A. F. & Sunyaev, R. A. 1975, A&A, 39, 185

Jahoda, K., Swank, J. H., Giles, A. B., et al. 1996, in Presented at the Society of Photo-Optical Instrumentation Engineers (SPIE) Conference, Vol. 2808, Proc. SPIE Vol. 2808, p. 59-70, EUV, X-Ray, and Gamma-Ray Instrumentation for Astronomy VII, Oswald H. Siegmund; Mark A. Gummin; Eds., ed. O. H. Siegmund & M. A. Gummin, 59–70

Janot-Pacheco, E., Motch, C., & Pakull, M. W. 1988, A&A, 202, 81

Jones, C. & Forman, W. 1976, ApJ, 209, L131

Jones, D. I. & Andersson, N. 2001, MNRAS, 324, 811

Joss, P. C. & Rappaport, S. A. 1984, ARA&A, 22, 537

Kahabka, P. 1987, NASA STI/Recon Technical Report N, 88, 19405

Kahabka, P. 1989, in ESA SP-296: Two Topics in X-Ray Astronomy, Volume 1: X Ray Binaries. Volume 2: AGN and the X Ray Background, ed. J. Hunt & B. Battrick, 447–452

Katz, J. I., Anderson, S. F., Grandi, S. A., & Margon, B. 1982, ApJ, 260, 780

Kellogg, E. M. 1975, ApJ, 197, 689

Ketsaris, N. A., Kuster, M., Postnov, K. A., et al. 2000, ArXiv Astrophysics e-prints

Klochkov, D., Horns, D., Santangelo, A., et al. 2007, A&A, 464, L45

Klochkov, D. K., Shakura, N. I., Postnov, K. A., et al. 2006, Astronomy Letters, 32, 804

Kreykenbohm, I., Wilms, J., Coburn, W., et al. 2004, A&A, 427, 975

Krimm, H., Barthelmy, S., Gehrels, N., et al. 2006, The Astronomer's Telegram 861

Kunz, M. 1996, PhD thesis, University of Tübingen, Germany

Kuster, M., Wilms, J., Staubert, R., et al. 2005, A&A, 443, 753

Lamb, F. K., Pethick, C. J., & Pines, D. 1973, ApJ, 184, 271

Landau, L. D. 1932, Phys. Z. Sowjetunion, 1, 285

Langer, S. H. & Rappaport, S. 1982, ApJ, 257, 733

Leahy, D. A. 1997, MNRAS, 287, 622

Leahy, D. A., Elsner, R. F., & Weisskopf, M. C. 1983, ApJ, 272, 256

Leahy, D. A., Yoshida, A., & Matsuoka, M. 1994, ApJ, 434, 341

Lee, U., Osaki, Y., & Saio, H. 1991, MNRAS, 250, 432

Levine, A. M., Bradt, H., Cui, W., et al. 1996, ApJ, 469, L33

Levine, A. M. & Jernigan, J. G. 1982, ApJ, 262, 294

Lewin, W. H. G. & van der Klis, M. 2006, Compact stellar X-ray sources (Compact stellar X-ray sources)

Lewin, W. H. G., van Paradijs, J., & van den Heuvel, E. P. J. 1995, X-ray binaries (Cambridge Astrophysics Series, Cambridge, MA: Cambridge University Press, —c1995, edited by Lewin, Walter H.G.; Van Paradijs, Jan; Van den Heuvel, Edward P.J.)

Liller, W. 1972, IAU Circ., 2415, 1

Lipunov, V. M. 1992, Astrophysics of neutron stars (Berlin ; New York : Springer-Verlag, c1992.), 5713

Lund, N., Budtz-Jørgensen, C., Westergaard, N. J., et al. 2003, A&A, 411, L231

McCollough, M. L., Turler, M., Willis, D., & Shaw, S. E. 2006, The Astronomer's Telegram 868

McCray, R. A., Shull, J. M., Boynton, P. E., et al. 1982, ApJ, 262, 301

Meszaros, P. 1992, High-energy radiation from magnetized neutron stars (Theoretical Astrophysics, Chicago: University of Chicago Press, —c1992)

Meszaros, P., Nagel, W., & Ventura, J. 1980, ApJ, 238, 1066

Mihara, T., Makishima, K., & Nagase, F. 1998, Advances in Space Research, 22, 987

Mineo, T., Ferrigno, C., Foschini, L., et al. 2006, A&A, 450, 617

Miroshnichenko, A. S., Fabregat, J., Bjorkman, K. S., et al. 2001, A&A, 377, 485

Motch, C. & Janot-Pacheco, E. 1987, A&A, 182, L55

Mowlavi, N., Kreykenbohm, I., Shaw, S. E., et al. 2006, A&A, 451, 187

Nagase, F. 1989, PASJ, 41, 1

Nakajima, M., Mihara, T., Makishima, K., & Niko, H. 2006, ApJ, 646, 1125

Negueruela, I., Okazaki, A. T., Fabregat, J., et al. 2001, A&A, 369, 117

Nelson, R. W., Salpeter, E. E., & Wasserman, I. 1993, ApJ, 418, 874

Ögelman, H. 1987, A&A, 172, 79

Ögelman, H., Kahabka, P., Pietsch, W., Trümper, J., & Voges, W. 1985, Space Science Reviews, 40, 347

Okazaki, A. T. 2001, PASJ, 53, 119

Okazaki, A. T. & Negueruela, I. 2001, A&A, 377, 161

Oosterbroek, T., Parmar, A. N., Dal Fiume, D., et al. 2000, A&A, 353, 575

Panchenko, I. E. & Postnov, K. A. 1994, A&A, 286, 497

Parmar, A. N., Oosterbroek, T., dal Fiume, D., et al. 1999, A&A, 350, L5

Parmar, A. N., Pietsch, W., McKechnie, S., et al. 1985, Nature, 313, 119

Parmar, A. N., Sanford, P. W., & Fabian, A. C. 1980, MNRAS, 192, 311

Parmar, A. N., White, N. E., & Stella, L. 1989a, ApJ, 338, 373

Parmar, A. N., White, N. E., Stella, L., Izzo, C., & Ferri, P. 1989b, ApJ, 338, 359

Pethick, C. J., Akmal, A., Pandharipande, V. R., & Ravenhall, D. G. 2000, Nuclear Physics B Proceedings Supplements, 80, C1114

Petterson, J. A. 1977, ApJ, 218, 783

Porter, J. M. 1999, A&A, 348, 512

Pravdo, S. H., Boldt, E. A., Holt, S. S., & Serlemitsos, P. J. 1977, ApJ, 216, L23

Pringle, J. E. 1981, Ann. Rev. Astron. Astrophys., 19, 137

Pringle, J. E. & Rees, M. J. 1972, A&A, 21, 1

Prokhorov, M. E., Shakura, N. I., & Postnov, K. A. 1990, Thirty-five-day cycle of HER X-1: Synthesised optical light curves in the model of freely processing neutron star, Tech. rep.

Quirrenbach, A., Bjorkman, K. S., Bjorkman, J. E., et al. 1997, ApJ, 479, 477

Rappaport, S. & Joss, P. C. 1977, Nature, 266, 683

Reig, P. & Coe, M. J. 1998, MNRAS, 294, 118

Reig, P. & Coe, M. J. 1999, MNRAS, 302, 700

Reig, P., Coe, M. J., Stevens, J. B., et al. 1997, in ESA SP-382: The Transparent Universe, ed. C. Winkler, T. J.-L. Courvoisier, & P. Durouchoux, 175

Reig, P., Stevens, J. B., Coe, M. J., & Fabregat, J. 1998, MNRAS, 301, 42

Revnivtsev, M., Fabrika, S., Abolmasov, P., et al. 2006, A&A, 447, 545

Reynolds, A. P. & Parmar, A. N. 1995, A&A, 297, 747

Reynolds, A. P., Parmar, A. N., Stollberg, M. T., et al. 1996, A&A, 312, 872

Reynolds, A. P., Parmar, A. N., & White, N. E. 1993, ApJ, 414, 302

Reynolds, A. P., Quaintrell, H., Still, M. D., et al. 1997, MNRAS, 288, 43

Ricketts, M. J. 1982, in Accreting Neutron Stars, ed. W. Brinkmann & J. Trümper, 100–105

Rothschild, R. E., Blanco, P. R., Gruber, D. E., et al. 1998, ApJ, 496, 538

Ruderman, M. 2001, ArXiv Astrophysics e-prints

Ruderman, M., Shaham, J., Tavani, M., & Eichler, D. 1989, ApJ, 343, 292

Rybicki, G. B. & Lightman, A. P. 1979, Radiative processes in astrophysics (New York, Wiley-Interscience, 1979. 393 p.)

Schandl, S. 1996, A&A, 307, 95

Schandl, S. & Meyer, F. 1994, A&A, 289, 149

Scott, D. M. & Leahy, D. A. 1999, ApJ, 510, 974

Scott, D. M., Leahy, D. A., & Wilson, R. B. 2000, ApJ, 539, 392

Sedrakian, A., Wasserman, I., & Cordes, J. M. 1999, ApJ, 524, 341

Shaham, J. 1977, ApJ, 214, 251

Shakura, N. I., Ketsaris, N. A., Prokhorov, M. E., & Postnov, K. A. 1998a, MNRAS, 300, 992

Shakura, N. I., Postnov, K. A., & Prokhorov, M. E. 1991, Soviet Astronomy Letters, 17, 339

Shakura, N. I., Postnov, K. A., & Prokhorov, M. E. 1998b, A&A, 331, L37

Shakura, N. I., Prokhorov, M. E., Postnov, K. A., & Ketsaris, N. A. 1999, A&A, 348, 917

Shakura, N. I. & Syunyaev, R. A. 1973, A&A, 24, 337

Sheffer, E. K., Kopaeva, I. F., Averintsev, M. B., et al. 1992, Soviet Astronomy, 36, 41

Skinner, G. K. & Ponman, T. J. 1994, MNRAS, 267, 518

Slettebak, A. 1988, PASP, 100, 770

Soong, Y., Gruber, D. E., Peterson, L. E., & Rothschild, R. E. 1990a, ApJ, 348, 641

Soong, Y., Gruber, D. E., Peterson, L. E., & Rothschild, R. E. 1990b, ApJ, 348, 634

Stairs, I. H. 2004, Science, 304, 547

Staubert, R., Bezler, M., & Kendziorra, E. 1983, A&A, 117, 215

Staubert, R., Schandl, S., Klochkov, D., et al. 2007a, A&A, [in preparation]

Staubert, R., Schandl, S., Klochkov, D., et al. 2006, in American Institute of Physics Conference Series, Vol. 840, The Transient Milky Way: A Perspective for MIRAX, ed. J. Braga, F. D'Amico, & R. E. Rothschild, 65–70

Staubert, R., Shakura, N. I., Postnov, K., et al. 2007b, A&A, 465, L25

Stelzer, B., Staubert, R., Wilms, J., et al. 1997, in American Institute of Physics Conference Series, Vol. 410, Proceedings of the Fourth Compton Symposium, ed. C. D. Dermer, M. S. Strickman, & J. D. Kurfess, 753

Still, M. & Boyd, P. 2004, ApJL, 606, L135

Still, M., O'Brien, K., Horne, K., et al. 2001, ApJ, 553, 776

Sunyaev, R. A., Gilfanov, M. R., Churazov, E. M., et al. 1988, Soviet Astronomy Letters, 14, 416

Tanaka, Y. 1986, in Lecture Notes in Physics, Berlin Springer Verlag, Vol. 255, IAU Colloq. 89: Radiation Hydrodynamics in Stars and Compact Objects, ed. D. Mihalas & K.-H. A. Winkler, 198

Tananbaum, H., Gursky, H., Kellogg, E. M., et al. 1972, ApJ, 174, L143

Terada, Y., Mihara, T., Nakajima, M., et al. 2006, ApJ, 648, L139

Trümper, J., Kahabka, P., Oegelman, H., Pietsch, W., & Voges, W. 1986, ApJ, 300, L63

Trümper, J., Pietsch, W., Reppin, C., et al. 1978, ApJ, 219, L105

Tsygankov, S. S., Lutovinov, A. A., Churazov, E. M., & Sunyaev, R. A. 2006, MNRAS, 371, 19

Tsygankov, S. S., Lutovinov, A. A., Churazov, E. M., & Sunyaev, R. A. 2007a, ArXiv e-prints, 704

Tsygankov, S. S., Lutovinov, A. A., Churazov, E. M., & Sunyaev, R. A. 2007b, Astronomy Letters, 33, 368

Ubertini, P., Lebrun, F., Di Cocco, G., et al. 2003, A&A, 411, L131

Ushimaru, N., Tawara, Y., Koyama, K., et al. 1989, PASJ, 41, 441

van den Heuvel, E. P. J. 1983, in Accretion-Driven Stellar X-ray Sources, ed. W. H. G. Lewin & E. P. J. van den Heuvel, 303–341

van Kerkwijk, M. H., Charles, P. A., Geballe, T. R., et al. 1992, Nature, 355, 703

Vedrenne, G., Roques, J.-P., Schönfelder, V., et al. 2003, A&A, 411, L63

Voges, W. 1985, NASA STI/Recon Technical Report N, 85, 34112

Voges, W., Pietsch, W., Reppin, C., et al. 1982, ApJ, 263, 803

Vrtilek, S. D. & Halpern, J. P. 1985, ApJ, 296, 606

Vrtilek, S. D., Mihara, T., Primini, F. A., et al. 1994, ApJ, 436, L9

Wang, Y.-M. 1987, A&A, 183, 257

White, N. E. & Holt, S. S. 1982, ApJ, 257, 318

White, N. E., Swank, J. H., & Holt, S. S. 1983, ApJ, 270, 711

White, N. E. & Zhang, W. 1997, ApJ, 490, L87

Wilms, J., Ketsaris, N. A., Postnov, K. A., et al. 2003, Izvestiya Akademii Nauk, Ser. Fizicheskaya, 67, 310

Wilson, C. A., Fabregat, J., & Coburn, W. 2005, ApJ, 620, L99

Wilson, C. A. & Finger, M. H. 2006, The Astronomer's Telegram 877

Wilson, C. A., Finger, M. H., Coe, M. J., Laycock, S., & Fabregat, J. 2002, ApJ, 570, 287

Wilson, R. B., Finger, M. H., Pendleton, G. N., Briggs, M., & Bildsten, L. 1994, in American Institute of Physics Conference Series, Vol. 308, The Evolution of X-ray Binariese, ed. S. Holt & C. S. Day, 475

Ziolkowski, J. 2002, Memorie della Societa Astronomica Italiana, 73, 1038

Appendix A

Turn-On times and maximum main-on fluxes

Below we provide parameters of individual 35 d cycles determined on the basis of the ASM RXTE data (Sectiom 4.3).

Cycle No.	Turn-on MJD	lower error days	upper error days	(O-C) orbital periods	maximum main-on flux ASM cts/s	error ASM cts/s
253	50146.22	0.32	0.34	0.8	6.7	0.2
254	50181.27	0.01	0.05	0.9	6.0	0.3
255	50216.46	0.32	0.07	1.1	6.7	0.2
256	50251.71	0.29	0.64	1.3	6.5	0.3
257	50285.49	0.63	0.56	0.7	6.4	0.4
258	50321.03	0.36	0.73	1.1	6.7	0.1
259	50355.63	1.09	0.45	0.9	5.7	0.3
260	50390.68	0.49	0.51	1.1	6.7	0.3
261	50425.41	0.08	0.05	1.0	7.5	0.2
262	50460.59	0.20	0.21	1.2	7.9	0.2
263	50496.44	0.21	0.06	1.8	7.3	0.2
264	50530.87	0.15	0.84	1.5	6.9	0.3
265	50565.73	0.22	0.07	1.5	7.5	0.2
266	50601.16	2.06	0.88	1.9	7.2	0.2
267	50636.66	0.55	0.25	2.2	6.8	0.3
268	50670.89	0.10	3.21	1.9	5.8	0.5
269	50705.18	0.24	0.49	1.5	7.3	0.3
270	50738.87	0.37	1.43	0.9	4.5	0.2
271	50773.32	0.29	0.71	0.6	4.6	0.4
272	50808.36	1.64	1.29	0.7	4.4	0.3
273	50842.36	0.38	0.41	0.2	6.2	0.3
274	50877.59	0.51	0.21	0.4	7.2	0.2

Cycle No.	Turn-on MJD	lower error days	upper error days	(O-C) orbital periods	maximum main-on flux ASM cts/s	error ASM cts/s
275	50912.64	0.02	0.44	0.6	6.0	0.1
276	50947.11	0.46	2.28	0.3	5.9	0.2
277	50981.83	0.00	0.26	0.3	7.0	0.2
278	51016.29	0.13	1.49	0.0	5.1	0.2
279	51050.84	0.43	0.16	-0.1	5.7	0.6
280	51085.78	0.01	0.05	-0.1	6.7	0.1
281	51120.33	0.36	0.71	-0.3	6.7	0.3
282	51154.65	2.78	0.15	-0.6	6.0	0.2
283	51188.79	0.31	0.83	-1.0	5.4	0.2
284	51223.64	0.09	0.91	-1.0	1.8	0.3
301	51826.35	0.32	0.21	5.0	4.2	0.6
302	51860.31	0.55	0.11	4.5	5.2	0.3
303	51894.86	0.79	1.07	4.3	6.2	0.6
304	51929.41	0.18	0.75	4.1	6.0	0.3
305	51963.28	0.21	0.85	3.5	6.2	0.2
306	51996.70	0.37	2.05	2.7	5.3	0.2
307	52033.00	0.19	0.47	3.5	7.1	0.4
308	52068.05	0.84	0.16	3.6	6.8	0.2
309	52102.64	0.05	0.95	3.5	7.5	0.3
310	52138.98	0.37	0.03	4.4	8.3	0.2
311	52175.05	0.99	0.01	5.1	6.0	0.2
312	52208.88	0.19	0.21	4.5	7.5	0.2
314	52279.18	0.44	1.01	4.8	7.3	0.5
315	52314.45	0.41	0.12	5.1	7.2	0.2
316	52349.15	0.12	0.01	5.0	7.5	0.1
317	52384.29	0.06	0.67	5.1	5.2	0.2
318	52419.40	0.85	0.07	5.3	7.2	0.4
319	52454.23	0.68	0.25	5.3	6.9	0.3
320	52489.84	0.34	0.06	5.7	7.1	0.3
321	52525.11	0.18	0.34	6.0	6.1	0.3
322	52559.64	0.40	0.45	5.8	7.1	0.4
323	52595.00	0.24	0.61	6.1	7.5	0.4
324	52630.18	0.38	0.35	6.3	7.3	0.2
325	52666.23	1.37	0.47	7.0	5.1	0.4
326	52701.90	1.82	0.08	7.5	5.7	0.3
327	52735.83	0.48	0.37	6.9	6.9	0.3
328	52770.96	0.72	0.75	7.1	7.7	0.6
329	52806.38	0.40	0.12	7.4	7.1	0.3
330	52842.17	0.15	0.63	8.0	6.5	0.2

Cycle No.	Turn-on MJD	lower error days	upper error days	(O-C) orbital periods	maximum main-on flux ASM cts/s	error ASM cts/s
331	52876.71	0.25	0.74	7.8	4.5	0.2
340	53193.40	0.09	0.64	9.6	4.6	0.4
341	53226.99	0.29	1.16	8.8	5.5	0.2
342	53262.86	0.05	0.02	9.4	4.8	0.3
343	53297.03	0.09	0.11	9.0	4.1	0.4
344	53330.28	0.30	5.81	8.1	0.0	0.0
345	53365.13	0.11	1.72	8.1	5.1	0.3
346	53400.05	0.20	0.46	8.1	6.0	0.4
347	53434.76	0.62	0.07	8.0	6.2	0.4
348	53470.50	0.12	0.19	8.5	6.7	0.4
349	53504.62	0.39	0.19	8.1	7.6	0.4
350	53539.27	0.50	2.25	8.0	7.7	0.6
351	53575.71	0.12	0.60	8.9	4.9	0.3
352	53609.87	0.19	0.14	8.5	5.8	0.3
353	53644.65	0.30	1.07	8.5	4.8	0.2
355	53714.58	0.20	0.53	8.6	5.2	0.5
356	53749.31	0.00	0.13	8.5	5.6	0.3
357	53784.16	0.15	0.90	8.5	4.4	0.4
358	53818.72	0.37	0.95	8.4	4.7	0.3
359	53852.98	0.82	0.10	8.0	6.9	0.4
360	53887.04	0.29	0.73	7.5	5.1	0.4
361	53922.69	0.06	0.01	8.0	6.4	0.3
362	53958.50	0.42	0.16	8.6	7.3	0.3
363	53994.05	0.55	0.24	9.0	7.4	0.3
364	54029.50	0.45	0.01	9.3	6.2	0.7
365	54063.41	0.57	1.00	8.8	5.6	0.3
366	54099.59	0.09	3.14	9.6	4.9	0.3
367	54133.65	0.36	0.58	9.1	3.4	0.3
368	54167.62	0.01	1.35	8.6	5.1	0.5
369	54202.62	0.52	0.58	8.7	6.0	0.4

Appendix B

Spin period

Below we provide the pulse period of Her X-1 measured by different satellites (see also Staubert et al. 2007a, and references therein). We used these data in Section 4.3.

time MJD	P-1.237 s μsec	error μsec	satellite
41259.369	820.644	0.051	Uhuru
41295.072	820.104	0.044	Uhuru
41312.075	819.521	0.340	Uhuru
41329.076	820.577	0.007	Uhuru
41364.779	820.592	0.010	Uhuru
41400.483	820.005	0.008	Uhuru
41434.486	818.866	0.030	Uhuru
41470.190	817.019	0.021	Uhuru
41504.193	815.472	0.011	Uhuru
41539.897	815.046	0.009	Uhuru
41573.900	815.121	0.013	Uhuru
41607.903	818.111	0.017	Uhuru
41643.607	817.817	0.045	Uhuru
41675.910	816.601	0.024	Uhuru
41711.613	815.339	0.018	Uhuru
41745.0	814.2	0.2	Uhuru
42482.5	796.	8.	Ariel
42623.15	808.25	0.080	SAS
42653.506	806.541	0.006	OSO
42901.83	803.	3.	Ballon-HEXE
43176.7	813.	5.	Ariel
43356.93	799.1	0.4	SAS
43389.679	796.600	0.004	OSO
43390.49	796.3	0.7	Ballon-HEXE
43564.722	793.725	0.004	HEAO
43738.213	794.019	0.007	HEAO

time MJD	P-1.237 s μsec	error μsec	satellite
43774.0	794.14	0.45	HEAO
43949.034	791.325	0.006	Einstein
44368.45	790.	4.	Ballon-HEXE
44370.45	792.	1.	Ballon-HEXE
44507.44	791.	2.	GBall
44767.05	792.	3.	Ariel
45135.5	793.9	0.1	Hakucho
45478.	794.22	0.01	Tenma
45761.	797.3	0.3	Astron
45778.56	792.00	0.05	EXOSAT
45798.	792.3	0.2	Astron
45864.	791.1	0.3	EXOSAT
45938.	791.5	0.17	Astron
46145.	785.	1.	EXOSAT
46180.	787.	2.	EXOSAT
46218.	781.1	0.2	EXOSAT
46988.95	768.0	1.4	HEXE
47021.70	773.1	0.2	HEXE
47303.02	773.0	14.0	HEXE
47367.68	766.5	1.4	HEXE
47404.2	765.884	0.002	Ginga
47441.87	765.0	0.3	HEXE
47646.0	757.973	0.007	Ginga
47663.7	757.758	0.013	Ginga
47682.4	759.653	0.003	Ginga
48014.7	751.400	0.260	Ginga
48100.5	750.046	0.004	Ginga
48120.3	749.	1.	ROSAT
48478.9	744.060	0.090	Ginga
48516.5	742.86	0.05	OSSE
48653.	745.5	0.7	OSSE
48895.80	746.212	0.003	BATSE
50008.00	736.57668	0.52537818	BATSE
50047.00	737.01001	0.37324405	BATSE
50080.00	740.35285	0.38823252	BATSE
50114.50	739.50999	0.39539538	BATSE
50149.00	738.55664	0.60371996	BATSE
50183.00	738.17668	0.45860901	BATSE
50217.50	736.41501	0.61583280	BATSE
50256.00	738.27800	0.45985215	BATSE
50289.00	739.47572	0.30115424	BATSE

time MJD	P-1.237 s μsec	error μsec	satellite
50290.66	739.511	0.019	RXTE
50325.00	737.46429	0.42046621	BATSE
50360.00	737.93667	0.66236947	BATSE
50393.50	736.93001	0.37674593	BATSE
50429.00	734.91999	0.33541323	BATSE
50464.00	733.47430	0.30563750	BATSE
50498.00	731.46667	1.4640127	BATSE
50536.00	732.05001	0.47450559	BATSE
50569.00	733.13890	0.38243535	BATSE
50601.50	731.50000	1.0816654	BATSE
50637.00	732.41333	0.71050060	BATSE
50674.50	732.09998	0.92195445	BATSE
50708.50	729.31625	0.32230857	BATSE
50741.00	732.88400	0.56961390	BATSE

Appendix C

Numerical model of disk wobbling in Her X-1

Below we describe our quantitative model for reproducing the observed behavior of anomalous dips and post-eclipse recoveries in Her X-1 (Sections 4.4 4.4.2). We argue that in order to explain the observations, the tilt of the outer regions of the disk should regularly change over the 35 d cycle. The physical reason for this can be a decrease of the mass transfer rate $\dot{M}$ supplied by the optical component as is expected in our model of a freely precessing neutron star as the underlying clock mechanism for the 35 d cycle in Her X-1 (Shakura et al. 1999).

To quantify this behavior, we calculated the net wobbling of the disk produced by tidal forces and the accretion stream. In contrast to Schandl & Meyer (1994), we ignored the viscous torques on the twisted accretion disk (see discussion in Section 4.4.1).

To account for the tidal torques, we approximated the outer disk as a solid ring of radius $r_{\rm d}$ In the quadrupole approximation, the ring precesses around the orbital angular momentum with the frequency

$$\omega_t \sim \frac{3}{4}\frac{r_{\rm d}^{3/2}\cos\theta}{\sqrt{q+q^2}}\omega_{\rm b}\,, \tag{C.1}$$

where $q \equiv M_{\rm x}/M_{\rm o} \simeq 0.64$ is the binary mass ratio and $\omega_{\rm b} = 2\pi/P_{\rm b}$ is the orbital binary frequency.

We denote the precession angle of the disk by ϕ (counting along the orbital rotation) and the tilt angle of the disk by θ. The tidal wobbling of the disk on top of its slow precessional motion in the leading order in $\omega_{\rm t}/(2\omega_{\rm b}+\omega_{\rm t}) \ll 1$ can be described as (Levine & Jernigan 1982)

$$\frac{d\phi}{dt} \simeq -\omega_{\rm t}\left[1+\frac{2\omega_{\rm b}}{2\omega_{\rm b}+\omega_{\rm t}}\cos 2(\phi_{\rm b}-\phi_{\rm pre})\right], \tag{C.2}$$

$$\frac{d\theta}{dt} \simeq \omega_{\rm t}\sin\theta\frac{2\omega_b}{2\omega_{\rm b}+\omega_{\rm t}}\sin 2(\phi_{\rm b}-\phi_{\rm pre})\,. \tag{C.3}$$

where $\phi_{\rm b}$ is the orbital phase and $\phi_{\rm pre}$ is the precessional phase.

Let us now discuss the dynamical action of the stream in more detail. The angular momentum of the outer parts of the disk $\mathbf{K}_{\rm d}$ are changed by the stream according to the equation

$$\frac{d\mathbf{K}_{\rm d}}{dt} = \dot{M}[\mathbf{r}\times\mathbf{v}]\,, \tag{C.4}$$

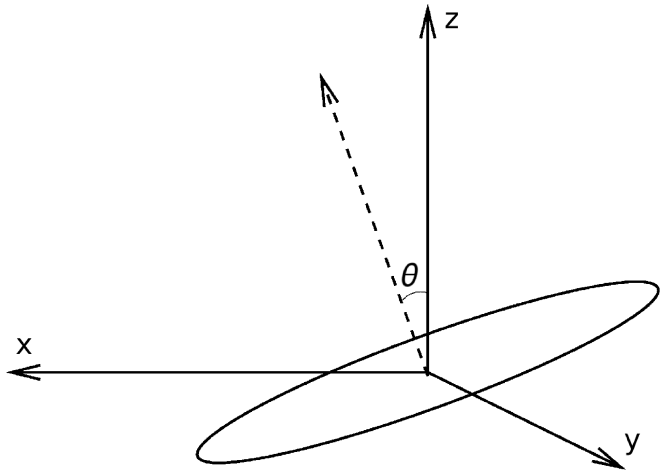

Figure C.1 The reference frame connected to the disk. The origin of the frame is at the center of the neutron star. The vector of the angular momentum **K** of the disk always lies in the $z - x$ plane.

where **r** and **v** are the distance from center of the disk to the impact point of the stream and the gas velocity at the impact point, respectively. They depend on the binary phase. In our model $\dot{M}$ is also a function of the orbital phase because the matter supply through the inner Lagrangian point depends on its position relative to the shadow produced by the tilted and twisted disk in the atmosphere of the optical star.

We will use the right-hand Cartesian reference frame rigidly connected to the accretion disk and consider it as non-rotating (this assumption is justified by the relatively slow precessional motion of the disk). The origin of the frame is at the center of the neutron star, the z-axis is normal to the orbital plane and the x-axis lies in the orbital plane and is directed such that the disks angular momentum vector always lies in the $z - x$ plane (see Fig. C.1):

$$\mathbf{K}_{\rm d} = (K_{\rm d}\sin\theta, 0, K_{\rm d}\cos\theta)\,. \tag{C.5}$$

Then the change of the disk momentum $d\mathbf{K}_{\rm d} = (d\mathbf{K}_{\rm x}, d\mathbf{K}_{\rm y}, d\mathbf{K}_{\rm z})$ can be written through the change in its components as

$$\begin{aligned} dK_{\rm d} &= dK_{\rm x}\sin\theta + dK_{\rm z}\cos\theta\,,\\ K_{\rm d}\theta &= dK_{\rm z}\cos\theta - dK_{\rm z}\sin\theta\,,\\ K_{\rm d}\sin\theta d\phi &= dK_{\rm y}\,. \end{aligned} \tag{C.6}$$

The time evolution of the disk angular momentum components (Eq.(C.4)) in this frame now can be written in the form:

$$\begin{aligned} \frac{dK_{\rm x}}{dt} &= \dot{M}v_{\rm rel}a(yv_{\rm z} - zv_{\rm y})\,,\\ \frac{dK_{\rm y}}{dt} &= \dot{M}v_{\rm rel}a(zv_{\rm x} - xv_{\rm z})\,,\\ \frac{dK_{\rm z}}{dt} &= \dot{M}v_{\rm rel}a(xv_{\rm y} - yv_{\rm x})\,, \end{aligned} \tag{C.7}$$

where x, y, z are dimensionless coordinates of the stream impact point (in units of binary separation a) and v_x, v_y, v_z are the components of the velocity of the stream at the impact point (in units of relative velocity of binary components v_{rel}). For computing ballistic trajectories of the gas stream from the Lagrangian point we used the primed right-hand reference frame x', y', z' rigidly rotating with the binary system. The origin of the frame is at the center of the neutron star, the z'-axis is normal to the orbital plane and the x'-axis is pointed to the center of the normal component. The transition from that frame to the one of the precessing disk is made by usual coordinate transformation:

$$\begin{aligned} x &= x' \cos\Phi - y' \sin\Phi\,, \\ y &= x' \sin\Phi + y' \cos\Phi\,, \\ z &= z'\,, \end{aligned} \tag{C.8}$$

and for velocities:

$$\begin{aligned} v_x &= v'_x \cos\Phi - v'_y \sin\Phi - \sqrt{(x')^2 + (y')^2}\sin\Phi\,, \\ v_y &= v'_x \sin\Phi + v'_y \cos\Phi + \sqrt{(x')^2 + (y')^2}\cos\Phi\,, \\ v_z &= v'_z\,, \end{aligned} \tag{C.9}$$

where Φ is the angle between the coordinate axes x and x'.

It is convenient to rewrite all equations in a dimensionless form. The angular momentum of the disk can be written as

$$|\mathbf{K}_d| = \gamma M_d \omega_k r_{eff}^2\,, \tag{C.10}$$

where r_d is the effective disk radius (see Section 3), M_d is the mass of the disk and $\omega_k = \sqrt{GM_x/r_{eff}^3}$ is the Keplerian frequency at the effective radius and γ is a numerical coefficient accounting for the surface density distribution $\Sigma(r)$; for example, in the standard Shakura-Sunyaev accretion disk (Shakura & Syunyaev 1973) $\Sigma \propto r^{-3/4}$ and $\gamma = 5/7$.

Now, from equations (C.6) and (C.7)) and making use of the Kepler's 3rd law, we arrive at the following equations for the change of angles ϕ and θ with the synodic angle $\tau = t\omega_s$ ($\omega_s = \omega_{pre} + \omega_b$):

$$\begin{aligned} \sin\theta \frac{d\phi}{d\tau} &= \frac{\dot{M}}{\gamma M_d \omega_s}\sqrt{\frac{M_x + M_o}{M_x}}\sqrt{\frac{a}{r_d}}[zv_x - xv_z]\,, \\ \frac{d\theta}{d\tau} &= \frac{\dot{M}}{\gamma M_d \omega_s}\sqrt{\frac{M_x + M_o}{M_x}}\sqrt{\frac{a}{r_d}}[\cos\theta(yv_z - zv_y) - \\ &\quad - \sin\theta(xv_y - yv_x)]\,. \end{aligned} \tag{C.11}$$

Using these equations, we calculated the change in angles ϕ and θ ($\Delta\phi$ and $\Delta\theta$) step by step and sum them up to find their behavior over one precessional cycle. The initial components of the velocities v'_x, v'_y, v'_z were chosen as a function of the synodic phase Φ in the way described in detail by Shakura et al. (1999).

The free parameters are the mass of the accretion disk M_d, the maximal disk tilt θ_0 and its change, the disk semi-thickness h/r_d at the outer boundary and the binary inclination angle i. We fixed the angle $i = 88.^\circ 6$ and the disks semi-thickness $h/r_d = 0.04$ (corresponding to a disk opening

angle of about 5°). The disks tilt was allowed to change with precessional phase according to the Eq. (4.12).

The angle $\theta_0 = 20°$ and numerical coefficients ($a = 0.6$, $b = 0.4$ and $\Delta = 15°$) in Eq. (4.12) were chosen to reproduce the observations. Now we can calculate the angle ϵ between the line of sight and the outer parts of the disk making use of Eq. (4.11).

In contrast to the case with constant tilt θ considered earlier by Shakura et al. (1999), the change of ϵ with precessional phase is determined also by the change of the tilt $\theta(\phi_{\rm pre})$ [Eq. (4.12)]. The effect of the phase delay Δ is illustrated by Fig. 4.17: the larger Δ is, the more asymmetric is the changing of ϵ The results are shown in Fig. 4.18.

Acknowledgements

A lot of people have contributed to this work. I want to thank them all for their help, advises, and discussions. First of all, I would like to thank Prof. Dr. Rüdiger Staubert for wise supervision of my research, encouraging and comprehensive discussions as well as finding the sources of funding for my PhD position and inviting me to Tübingen.

Prof. Dr. Andrea Santangelo coordinated activity of our X-ray and Gamma-ray astronomy group. I thank him for providing (together with Rüdiger Staubert) the excellent environment and friendly atmosphere inside the group as well as for useful discussions and his help with preparing the text of the thesis.

I also want to thank my colleagues in the X-ray and Gamma-ray astronomy group with whom I constantly exchanged with ideas, opinions, questions etc.: Sonja Fritz, Isabel Caballero, Dieter Horns, Jürgen Barnstedt, Nikolai von Krusenstiern, Lioubov Rodina, Victor Doroshenko, and Rozaliya Doroshenko.

I am grateful to Nikolai Shakura and Konstantin Postnov with whom I started my first scientific research as a diploma student of Moscow University and who continued to help me during my work on the thesis. I also thank them for their hospitality during our visits to Moscow after I have moved to Tübingen.

This thesis would also not be possible without discussions with Jörn Wilms, Ingo Kreykenbohm, Peter Kretschmar, Valeriy Suleymanov, Artem Tuntsov, Daniil Smirnov, and Elena Glushkova.

Finally, I would like to thank my wife Erzhena for her endless patience with me while I rejected vacations, journeys, holiday etc. and her understanding that the amount of time required by scientific research can never be restricted by any “Arbeitsvertrag”.

Lebenslauf

20.02.1982	geboren in Nizhnekamsk (resp. Tatarstan, Russland)
1989–1999	Schule Volgodonsk (Russland)
ab Sep. 1999	Studium der Physik und Astronomie (Diplom), Fakultät für Physik der M. V. Lomonosov Universität Moskau (Russland)
2003–2004	Belegarbeit am Sternberg Astronomischen Institut der M. V. Lomonosov Universität Moskau unter Anleitung von Prof. Dr. N. I. Shakura über das Thema “Modeling of Optical Light Curves of Close Binary Systems containing an Accretion Disk of a Complicated Geometry by the Example of Her X-1 / HZ Her”
2004–2005	Diplomarbeit am Sternberg Astronomischen Institut der M. V. Lomonosov Universität Moskau unter Anleitung von Prof. Dr. N. I. Shakura über das Thema “Analysis of the X-ray and Optical Light Curves of the Close Binary System Her X-1 / HZ Her”
Jan 2005	Diplom in Astronomie
Feb. 2005 – – Okt. 2007	Promotion am Astronomischen Institut der Eberhard-Karl-Universität Tübingen unter Anleitung von Prof. Dr. R. Staubert über das Thema “X-ray observations of the accreting pulsars Her X-1 and EXO 2030+375”

Berufliche Tätigkeit

seit Feb. 2005	Wissenschaftlicher Mitarbeiter am Astronomischen Institut der Eberhard-Karl-Universität Tübingen